



Università degli Studi di Ferrara

DOTTORATO DI RICERCA IN  
FISICA  
CICLO XXVII

COORDINATORE Prof. Guidi Vincenzo

STUDY OF COHERENT INTERACTIONS  
BETWEEN CHARGED PARTICLE BEAMS AND  
CRYSTALS  
FOR BEAM STEERING AND INTENSE  
ELECTROMAGNETIC RADIATION GENERATION

Settore Scientifico Disciplinare FIS/01

**Dottorando**  
Dott. Bandiera Laura

**Tutore**  
Prof. Guidi Vincenzo

Anni 2012-2014



# Contents

<b>Introduction</b>	<b>iii</b>
<b>List of publications</b>	<b>ix</b>
<b>1 Coherent interactions of charged particle beams with crystalline media</b>	<b>1</b>
1.1 Channeling and related phenomena in straight crystals . . . . .	3
1.1.1 Directional effects . . . . .	3
1.1.2 Planar motion of charged particles in a straight crystal . . . . .	4
1.1.3 Axial Channeling . . . . .	17
1.1.4 Energy Loss . . . . .	19
1.2 Coherent interactions in bent crystals . . . . .	20
1.2.1 Planar Channeling in a bent crystal . . . . .	20
1.2.2 Dynamics of over-barrier particles in bent crystals . . . . .	22
1.2.3 Multiple Volume Reflection in One Crystal . . . . .	26
<b>2 Electromagnetic radiation emitted by ultrarelativistic electrons and positrons in straight and bent crystals</b>	<b>31</b>
2.1 General features of emission of radiation by high-energy particles in straight crystals . . . . .	32
2.2 General features of emission of radiation by high-energy particles in bent crystals . . . . .	41
2.2.1 Radiation accompanying single and multiple volume reflection . . . . .	41
<b>3 A method for calculation of emitted radiation in straight and bent crystals based on the Baier Katkov quasiclassical formula</b>	<b>47</b>
3.1 The Baier-Katkov quasiclassical formula . . . . .	47
3.2 Algorithm for the Direct Integration of BK formula . . . . .	49
3.3 RADCHARM++ . . . . .	52

<b>4</b>	<b>Radiation emitted by 120 GeV/c electrons through single and multiple volume reflection in a short bent crystal</b>	<b>55</b>
4.1	Experimental setup . . . . .	56
4.1.1	Part A of the experimental setup: the tracking system . . . . .	56
4.1.2	Part B of the experimental setup: the spectrometer and the electro-magnetic calorimeter . . . . .	59
4.2	Experimental measurements . . . . .	62
4.2.1	Single Volume Reflection . . . . .	62
4.2.2	Multiple Volume Reflection . . . . .	77
4.3	Possible applications . . . . .	82
4.3.1	Intense $\gamma$ -source . . . . .	82
4.3.2	Crystal-assisted collimation in electron/positron colliders . . . . .	83
<b>5</b>	<b>Investigation on coherent interactions of sub-GeV electrons for beam steering and high intense e.m. radiation generation</b>	<b>85</b>
5.1	Experimental Setup at MAMI B . . . . .	86
5.2	Steering of sub-GeV electrons . . . . .	90
5.3	Radiation measurements . . . . .	95
5.4	Summary . . . . .	102
<b>6</b>	<b>Recent studies on coherent interactions of 400 GeV/c protons with innovative crystals</b>	<b>105</b>
6.1	Characterization of a crystalline undulator with 400 GeV/c protons . . . . .	105
6.1.1	Why a crystalline undulator? . . . . .	105
6.1.2	Fabrication and Interferometric Characterization of a periodically bent crystal . . . . .	107
6.1.3	Experiment with high-energy protons . . . . .	109
6.1.4	Monte Carlo simulations . . . . .	112
6.1.5	Summarizing . . . . .	115
6.2	Mirroring of 400 GeV/c protons by a ultra-thin straight crystal . . . . .	115
6.2.1	A crystal <i>mirror</i> . . . . .	115
6.2.2	<i>Crystal mirror</i> fabrication and characterization at the Sensor and Semiconductor Lab of Ferrara University . . . . .	117
6.2.3	Experiment at CERN SPS . . . . .	120
6.2.4	Summarizing . . . . .	125





# Introduction

When a charged particle crosses a crystalline medium with a small angle with respect to a crystallographic direction (or plane), it suffers a series of correlated collisions (*coherent interactions*) with the neighboring atoms in the same row (plane) [1]. Moreover, if the particle trajectory is aligned with respect to crystal planes/axes, it may be trapped inside the planar/axial potential well, i.e., the *channeling* of the particle occurs.

Since its discovery by computer simulations in 1963 [2], channeling and coherent interactions in general have been exploited for different purposes. At non relativistic energies, channeling is an important tool for material analysis by ion channeling [3], while in the high-energy range, coherent interactions have been investigated for years for high-intense e.m. radiation generation by  $e^\pm$  [4]. Hard x- and  $\gamma$ -radiations are usually generated by ultra-relativistic electrons passing through strong magnetic fields of undulators and wigglers, which allow reaching photon energies of hundreds-keV at modern synchrotrons and of tens-MeV in the polarized  $\gamma$ -ray sources for positron production in future linear colliders [5]. Harder gamma-quanta are typically produced through electron and positron bremsstrahlung in matter [6], for which mostly soft photons are emitted. With the aim of increasing the intensity of photo-production, coherent effects in crystals, such as coherent bremsstrahlung (CB) and channeling radiation (CR) can be exploited. In particular, CB facilities for generation of high-intense and monochromatic radiation are already available worldwide [7]. CB is originated by interference effects in the bremsstrahlung of electrons/positrons crossing the periodic structure of a crystal [8–10], while CR is generated by the oscillatory motion of channeled particles inside the planar/axial potential well [11].

Another scientific field in which the coherent interactions in crystals have generated particular interest is the Accelerator Physics, where such phenomena can be exploited for beam manipulation through the usage of bent crystals [12], for either beam collimation or extraction [13]. For instance, a crystal-assisted collimation for high-energy hadron machines has been proposed. Such collimation scheme consists in the usage of a short bent crystal as primary collimator to deflect channeled particles of the beam halo. Within this

context, the reduction of nuclear interaction rate for channeled protons and Pb ions has been proved to lower beam losses in the CERN-SPS synchrotron in the framework of the UA9 experiment [14, 15]. This possibility has also been demonstrated for another coherent effect, which is typical of bent crystals, i.e., the volume reflection (VR), which consists in the deflection of over-barrier particles in a bent crystal [16]. On the strength of these results, bent crystals have been proposed for collimation and extraction at the LHC [17, 18].

Indeed, the usage of bent crystals also offers new opportunities for intense production of e.m. radiation by high-energy electrons and positrons. In particular, the radiation accompanying VR is promising for relevant applications. The main advantage of the radiation accompanying VR is the large and adjustable angular acceptance, which can be exploited for a  $\gamma$ -source with the usage of a relatively poor emittance electron beam. Moreover, the combination of the deflecting power of VR with the high-intense radiation generation could be investigated for a crystal-based collimation in future electron/positron colliders, such as ILC [19]. Up to now, only few experiments on radiation accompanying VR have been performed [20–22], while more experimental data are needed to test the feasibility of the proposed applications.

The work presented in thesis has been devoted to the study of coherent interactions for innovative schemes of either intense e.m. radiation production or beam steering. A particular attention has been given to the combination of these two possibilities.

The first Chapter is dedicated to an overview of coherent interactions between charged particle beams and crystals. Meanwhile, the second Chapter describes the phenomenology of the e.m. processes in crystals at high energies. The first part represents an overview of radiation emission in straight crystals, while the second part is dedicated to the radiation processes in bent crystals.

In the third Chapter, a method for computation of the emitted radiation by  $e^\pm$  in crystals, based on the direct integration of the Baier-Katkov formula, is described. This method has been used to predict and describe the experimental results on e.m. radiation production.

In the fourth Chapter, an experimental study conducted by the INFN-COHERENT group and performed at the extracted beamline H4 of SPS with 120 GeV/c electrons is presented. Two coherent effects were investigated, i.e., the single and multiple volume reflections. Indeed, despite many advantages, the radiation accompanying VR is limited by the relatively weak strength of the field of crystal planes, which may limit the possibility of high-intense  $\gamma$ -production. In order to increase the intensity of coherent radiation in bent crystals, one can take advantage of the effect of multiple volume reflection in one crystal (MVROC).

The fifth Chapter is dedicated to the investigation of the possibility to steer sub-GeV electron beams with the usage of ultra-thin bent crystals. An experiment was carried out at the MAInzer MIcrotron (MAMI) of the University of Mainz (Germany) by the INFN-ICERAD experiment in collaboration with the MAMI group. Thanks to a new developed technique available at the Sensor and Semiconductur Laboratory of the Ferrara University, a bent crystal with the characteristics suited for deflecting a sub-GeV negative beam was fabricated. This experiment opens up the way for the investigation and exploitation of coherent interactions in bent crystals in the Sub-GeV/GeV energy range accessible by many electron accelerators worldwide and which is interesting for X- or  $\gamma$ -ray sources. With the aim of understating how the emission of e.m. radiation changes with energy, the radiation accompanying coherent interactions with the ultra-thin bent crystal was also measured.

The last Chapter goes beyond the study of beam manipulation and emitted radiation by high energy electrons in bent crystals, describing some interesting results achieved with the usage of 400 GeV/c protons, available at the external line H8 of SPS, interacting with two innovative crystals, i.e., a **periodically bent crystal** and a **crystal mirror**. The first part of the chapter is dedicated to the characterization of a periodically bent crystal via channeling of 400 GeV/c protons, conducted by the INFN-ICERAD experiment. A periodically bent crystal can be used in particular conditions as an innovative and compact source of intense X- and  $\gamma$ -radiation, i.e., a crystalline undulator ([23] and references therein). The second part of the Chapter is devoted to the study of the steering of ultra-high energy protons with the usage of an ultra-thin (some tens of microns) straight crystal, i.e., a crystal mirror [24]. This experimental work has been done in the framework of the UA9 experiment, which is devoted to the investigation of possible crystal-assisted collimation in high-energy hadron accelerators/colliders. Concerning this possibility, unlike the traditional scheme relying on mm-long curved crystals, particle mirroring enables beam steering of high-energy hadrons via interactions with a  $\mu\text{m}$ -thick straight crystal, thereby decreasing the unwanted nuclear interactions.



# List of publications

The work presented in this thesis is based on the following articles (two of them are still unpublished) and conference proceedings:

- A1:** V. Guidi, L. Bandiera, V. Tikhomirov, Phys. Rev. A **86** (2012) 042903, *Radiation generated by single and multiple volume reflection of ultrarelativistic electrons and positrons in bent crystals*
- A2:** L. Bandiera *et al*, Nucl. Instr. Meth. B **309** (2013) 135, *On the radiation accompanying volume reflection*
- A3:** L. Bandiera *et al*, Phys. Rev. Lett. **111** (2013) 255502, *Broad and Intense Radiation Accompanying Multiple Volume Reflection of Ultrarelativistic Electrons in a Bent Crystal*
- A4:** L. Bandiera *et al*, Journal of Physics: Conference Series **517** (2014) 012043, *Single and Multiple Volume Reflections of Ultra-Relativistic Electrons in a Bent Crystal as Tools for Intense Production of Electromagnetic Radiation*
- A5:** A. Mazzolari *et al*, Phys. Rev. Lett. **112** (2014) 135503, *Steering of a sub-GeV electron beam through planar channeling enhanced by rechanneling*
- A6:** W. Scandale *et al*, Phys. Lett. B **734** (2014) 1-6, *Mirroring of 400 GeV/c protons by an ultra-thin straight crystal*
- A7:** E. Bagli *et al*, Eur. Phys. J. C **74** (2014) 1-7, *Experimental evidence of planar channeling in a periodically bent crystal*
- A8:** L. Bandiera, E. Bagli, V. Guidi, V. Tikhomirov, submitted, *RADCHARM++: a C++ Routine to Compute the Electromagnetic Radiation Generated by Relativistic Charged Particles in Crystals and Complex Structures*
- A9:** L. Bandiera *et al*, submitted, *Investigation on the electromagnetic radiation emitted by sub-GeV electrons in a bent crystal*

Articles and proceeding not included in this thesis published during the PhD:

- N1:** E. Bagli *et al*, JINST **7** (2012) P04002, *A topologically connected multistrip crystal for efficient steering of high-energy beam*
- N2:** W. Scandale *et al*, Phys. Lett. B **719** (2013) 70, *Measurement of the dechanneling length for high-energy negative pions*
- N3:** E. Bagli *et al*, Phys. Rev. Lett. **110** (2013) 175502, *Coherent Effects of High-Energy Particles in a Graded  $Si_{1-x}Ge_x$  Crystal*
- N4:** D. De Salvador *et al*, J. App. Phys. **114** (2013) 154902, *Highly bent (110) Ge crystals for efficient steering of ultrarelativistic beams*
- N5:** E. Bagli *et al*, Eur. Phys. J. C **74** (2014) 2740, *Steering efficiency of a ultrarelativistic proton beam in a thin bent crystal*
- N6:** W. Scandale *et al*, Phys. Lett. B **726** (2013) 182, *Optimization of the crystal assisted collimation of the SPS beam*
- N7:** W. Scandale *et al*, Phys. Lett. B **733** (2014) 366, *Observation of focusing of 400 GeV/c proton beam with the help of bent crystals*
- N8:** W. Scandale *et al*, Nucl. Instr. Meth. B **338** (2014) 108, *Deflection of high energy protons by multiple volume reflections in a modified multi-strip silicon deflector*
- N9:** U. Wienands *et al*, accepted to be published in Phys. Rev. Lett. *Observation of Deflection of a Beam of Multi-GeV Electrons by a thin crystal*





# Chapter 1

## Coherent interactions of charged particle beams with crystalline media

In 1912 Stark [25] had the first idea that the atomic ordered structure of a crystal may be important for the process of interaction of charged particles with matter. Nevertheless, this old idea of the **directional effects**<sup>1</sup> for a charged particle moving in a crystal was dormant until the early 1950s, when interference effects in the bremsstrahlung of electrons/positrons crossing the periodic structure of a crystal appeared for the first time in the works of Ferretti [8], Ter-Mikaelian [9], Dyson and Uberall [10]. Such effect took the name *coherent bremsstrahlung* (CB), to be distinguished from the ordinary bremsstrahlung in an amorphous medium described by the Bethe and Heitler formulation (BH) [6]. CB was experimentally proven true by Diambrini-Palazzi et al. at Frascati in 1960 [26]. In 1963 the channeling effect was discovered in computer simulations [27] and experiments [28], which observed too much long ranges of ions in crystal.

The theoretical explanation of the channeling effect has been given by Lindhard [1] in 1964. Lindhard introduced the concept of coherent scattering of charged particles by the atoms of a crystal when the trajectory of the particle is nearly aligned with a crystal axis (or plane) due to correlations between successive collisions of a particle with the atoms in the same row/plane. In such low-angle approximation one can replace the screened Coulomb potentials of separate atoms with an average continuous potential of the crystal atomic string/plane. Channeling consists in the trapping of a charged particle within the planar/axial potential well.

In the 1976 Tsyganov proposed to use slightly bent monocrystals to deflect high-energy particle beams [12]; his idea was that a channeled particle would follow the direction of the

<sup>1</sup>In this thesis, directional effects and coherent interactions are used as synonyms.

bent atomic planes (or axes), thus deviating from its initial direction by an angle equal to the bending angle of the crystal. In 1979 the possibility to steer a charged beam using a bent crystal was demonstrated experimentally with 8.4 GeV proton beam extracted from the synchrotron of the Laboratory of High Energies, JINR [29, 30].

In the following years other effects were discovered studying bent crystals such as *volume capture* and *volume reflection*. The first one consists in the phenomenon of capturing 'quasi-channeled' particles (i.e. unchanneled particles that are moving in a trajectory nearly aligned to the crystal planes) into a channeling mode in the depth of a bent single crystal in the region where the particle trajectories are tangential to the crystallographic planes; it was discovered in 1982 by using a 1 GeV proton beam [31]. The second one consists in the deflection of 'quasi-channeled' particles in a direction *opposite* to the crystal bending and hence opposite to the one of the channeled particles deflection; this effect was found in computer simulations in 1987 by Taratin and Vorobiev [16].

Another interesting effect called *Multiple Volume Reflections in One Crystal* was predicted in 2007 through computer simulation by Tikhomorov [32]. MVROC concerns those particles entering a bent crystal with a small angle with respect to a crystal axis and consists in a set of volume reflections by different planes intersecting the axis.

Bent crystals have opened up new perspectives for manipulation of high-energy particle trajectories such as particle beam extraction and halo scraping. In last years, the effects of volume reflection (VR) [33–35] and multiple volume reflection in one crystal (MVROC) [36–38] were observed and widely studied mainly in connection with the problem of halo cleaning in the Large Hadron Collider (LHC).

In this chapter, a brief description of coherent interactions in straight and bent crystals is presented. With the aim of not becoming too prolix, it was preferred to give most of the attention to those coherent effects that have been investigated in this work of thesis. Nevertheless, other possibilities based on planar, such as multiple volume reflection in a series of crystals [39], or axial effects, e.g., axial channeling [40] and doughnut scattering [37, 41], have been deeply investigated during the years for beam steering or intense e.m. radiation generation.

# 1.1 Channeling and related phenomena in straight crystals

## 1.1.1 Directional effects

In this section the theoretical explanation of the directional effects given by Lindhard in 1964-5 is presented [1]. He demonstrated that when a charged particle has a small incidence angle with respect to a crystallographic axis (plane) the successive collisions of the particle with the lattice atoms are correlated, i.e. *coherent scattering* occurs, and therefore one could consider the interaction of the charged particle with the continuous atomic string (plane) rather than with single atoms.

Any charged particle crossing an amorphous medium, which is characterized by homogeneity, isotropy and randomness, suffers uncorrelated collisions with single atoms. These collisions may be of different nature, depending on the impact parameter. The most common are multiple Coulomb scattering with atomic nuclei and energy loss in collisions with atomic electrons. In a random system the slowing-down process is practically independent of the particle direction and therefore the probability distribution in energy loss and scattering angle depends only on the density of the penetrated medium. This is essentially a gas picture that may be called a *random system*, implying homogeneity, isotropy and random collisions.

A single crystal is a medium in which directional effects in stopping might appear, due to both inhomogeneity, anisotropy and lack of randomness. In fact, a crystal is a regular arrangement of atoms located on a lattice so that, depending on the point of view of the observant, the atoms are arranged in strings or planes. Any anisotropy due to the lattice structure may result in some kind of correlation between collisions.

The directional effects for charged particles crossing a crystal were discovered for several processes requiring a small impact parameter in a particle-atom collision (*e.g.*, nuclear reactions, large-angle scattering and energy loss). We may classify directional effects for charged particles moving through single crystal using two labels: *ungoverned motion* and *governed motion*. By *ungoverned motion* is meant the approximation where the path of the particle may be assumed to be essentially unaffected by the structure of the substance. *Governed motion* means that a path deviates strongly from the one in a random system, because it is determined by the structure of the medium. Governed motion leads to more fundamental changes in physical processes, whereas ungoverned motion just show fluctua-

tions in physical effects due to correlations<sup>2</sup>.

For treatment of possible governed motion the scattering angle of the particle may be assumed to be small, because scattering by large angles would imply that the original direction is completely lost, as well as correlations associated with direction. The scattering of a particle can be ascribed mainly to nuclear collisions, causing the interaction with the charge distribution of an atom as a whole through nearly elastic collision. Moreover, since collision requires that the particle comes close to the atom, strong correlations between collisions occur if the particle moves at a small angle with a row of atoms; if it passes close to one atom in a row, it must also pass close to the neighboring atoms in the same row. At this stage, one may introduce the concept of continuous string of atoms, which is characterized for example by the distance of separation,  $d$ , of atoms placed on a straight line. As a result, the trajectory of a particle obtained after a sequence of collisions with single atoms becomes indistinguishable from the trajectory obtained from *smearing* (averaging) the atomic potentials along the string.

In the next sections, the concepts of continuous potential and of channeling are described following the book [42]. Most attention is given to planar effects, since they are the most investigated within this work of thesis.

## 1.1.2 Planar motion of charged particles in a straight crystal

### Continuous Planar Potential

When the motion of a charged particle is aligned (or nearly aligned) with a string (or plane), a coherent scattering with the atoms of the string (or plane) may occur. In such *low-angle approximation* one can replace the potentials of the single atoms with an averaged **continuous potential**. The atomic string (plane) in the continuum approximation gently steers a particle away or towards the atoms depending on the particle charge's sign.

If a particle is misaligned with respect to the atomic strings while moving at a small angle with respect to a crystallographic plane, the influence of the plane may be treated as a continuous potential, where averaging is made over the two planar coordinates:

$$U_{pl}(x) = Nd_p \int_{-\infty}^{\infty} \int_{-\infty}^{\infty} V(x, y, z) dy dz \quad (1.1)$$

$V(x, y, z)$  being the particle-atom interaction potential,  $N$  the density of atoms and  $d_p$  the

<sup>2</sup>In Lindhard description, interference effects in the process of bremsstrahlung were not considered.

interplanar spacing. Fig. 1.1(a) shows a scheme for a positive particle interacting with a crystal plane composed by individual atoms. If the distance between the particle and the

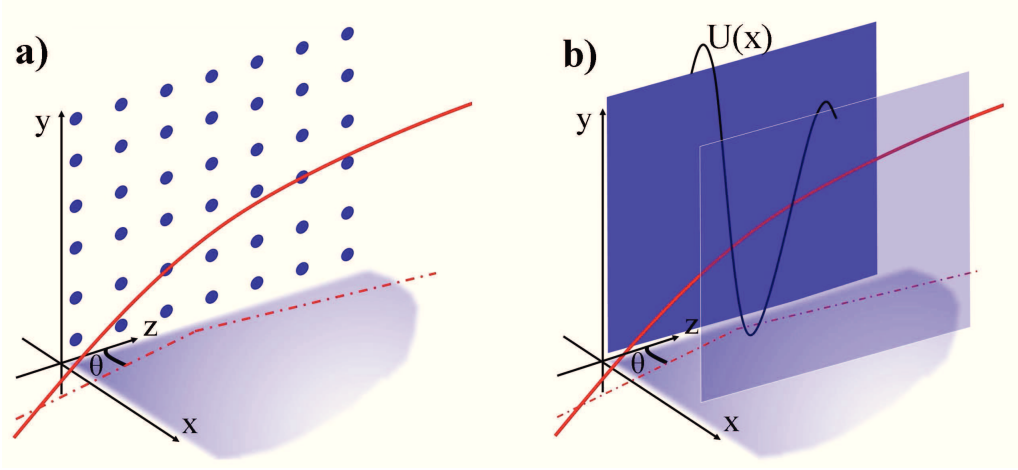


Figure 1.1: a) A positive particle moving in a crystal misaligned with respect to the axis but at a small angle with respect to a crystallographic plane. b) The particle feels an averaged planar continuous potential ( $U(x)$ ), which form a potential well between two neighboring crystal planes [43].

atom,  $r = \sqrt{x^2 + y^2 + z^2}$ , is not too much larger than  $a_{TF}$  (the screening length of the particle-atom interaction), the potential  $V(r)$  is Thomas-Fermi-like, and can be described in terms of:

$$V(r) = \frac{Z_i Z e^2}{r} \Phi\left(\frac{r}{a_{TF}}\right), \quad (1.2)$$

$Z_i e$  being the particle charge and  $Z$  the atomic number of the crystalline medium. Here, the screening distance is  $a_{TF}^3 = 0.8853 a_B (Z^{\frac{2}{3}} + Z_i^{\frac{2}{3}})^{-\frac{1}{2}}$  and the Bohr radius is  $a_B = 0.529 \text{ \AA}$ . The first factor in eq. 1.2 represents the potential of point-like charge, while the screening function  $\Phi\left(\frac{r}{a_{TF}}\right)$  is the Fermi function belonging to an isolated atom that takes into account the charge distribution of the atom. By using the approximation for the screening function  $\Phi$  suggested by Lindhard

$$\Phi\left(\frac{r}{a_{TF}}\right) = 1 - \left(1 + \frac{3a_{TF}^2}{r^2}\right)^{-\frac{1}{2}}, \quad (1.3)$$

<sup>3</sup>In the following it is often implicitly understood that  $Z_i \ll Z$  so that  $a_{TF}$  is put equal to  $0.8853 a_B Z^{-\frac{1}{3}}$ .

the following approximation for the planar continuous potential is obtained:

$$U_{pl}(x) = 2\pi N d_p Z_i Z e^2 (\sqrt{x^2 + 3a_{TF}^2} - x). \quad (1.4)$$

A more accurate approach is given by Doyle and Turner [44], where the potential  $V(r)$  is obtained by fitting the electron scattering factor, determined by a Hartree-Fock calculation, to experimental results. The Doyle-Turner potential has the form

$$V(r) = 16\pi Z_i a_B e^2 \sum_{i=1}^4 \frac{a_i}{(b_i/\pi)^{3/2}} \exp\left[\frac{-r^2}{(b_i/4\pi)^2}\right], \quad (1.5)$$

where  $a_i$  and  $b_i$  are tabulated coefficients [44]. The planar static continuum potential according to Doyle-Turner is:

$$U_{pl}(x) = 2\pi^{1/2} N d_p Z_i a_B e^2 \sum_{i=1}^4 \frac{a_i}{(b_i/4\pi^2)^{1/2}} \exp\left[\frac{-x^2}{(b_i/4\pi^2)^2}\right], \quad (1.6)$$

Another common approximation for the Fermi function  $\Phi$  was given by Molière [45], leading to a different approximation for planar potential:

$$U_{pl}(x) = 2\pi N d_p Z_i Z e^2 a_{TF} \sum_{i=1}^3 \frac{\alpha_i}{\beta_i} \exp\left(-\frac{\beta_i x}{a_{TF}}\right), \quad (1.7)$$

being  $\alpha = (0.1, 0.55, 0.35)$  and  $\beta = (6.0, 1.2, 0.3)$  the Molière's coefficients.

The formulas seen so far are valid in the idealized case of a perfect lattice and may be used as a *first approximation*. Indeed, thermal vibrations of atoms modify the static-lattice potential near the plane at a distance of the order of thermal vibrations root-mean square amplitude,  $u_T$ . If we suppose that individual atoms vibrate independently and that the vibrations are distributed according to Gaussian probability distribution as

$$P(x) = \frac{1}{\sqrt{2\pi u_T^2}} \exp\left(-\frac{x^2}{2u_T^2}\right), \quad (1.8)$$

the modified potential can be obtained by averaging  $U_{pl}(x)$  over this distribution. As an example, for silicon at room temperature,  $u_T$  is about 0.075 Å, which is quite small as compared to the lattice constant  $d = 5.43$  Å. Fig. 1.2 displays the continuous potential under Molière approximation with the contribution of thermal vibrations at different temperatures for the case of Si(110) planes.

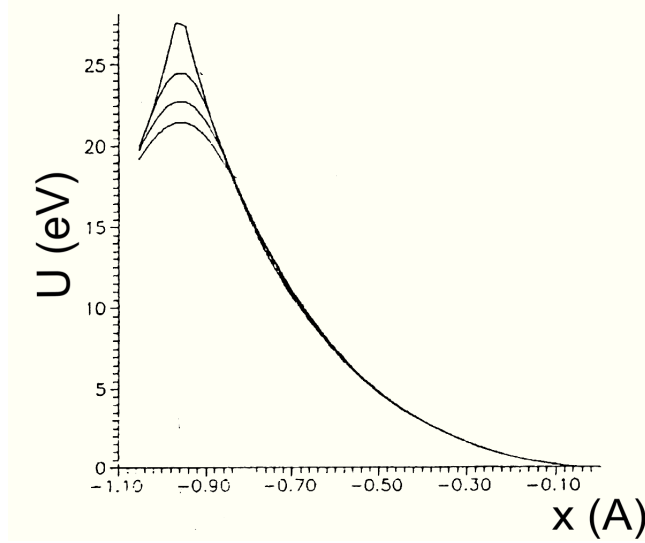


Figure 1.2: The Molière potential of the Si(110) planes at different temperatures, and the potential of the static lattice. Top to bottom at the left edge: static, 77K, 300K, 500K [42].

In the low-angle approximation a charged particle moves in a crystal in a potential that is the sum of the potentials of the single planes, but one can consider that contributions of two nearest atomic planes dominate. The resulting potential for positively charged particles can be approximated as

$$U_{pl}(x) \approx U_{pl}(d_p/2 - x) + U_{pl}(d_p/2 + x) - 2U_{pl}(d_p/2), \quad (1.9)$$

$x$  being the transverse coordinate defined with respect to the midplane between the atomic layers, and  $U(0) = 0$ . As a result, a positive particle moving in a crystal nearly aligned with crystal planes *sees* the crystal as a series of potential wells,  $U(x)$ , formed between neighboring planes (see Fig. 1.1(b)).

Usually, in *channeling experiments* with high-energy charged beams, mostly diamond-lattice crystals (see Fig. 1.3-left), such as C, Si or Ge, are used. In some cases, since higher  $Z$  materials generate a stronger potential, W crystals are used. Si is extensively used in channeling experiments due to the high degree of perfection of crystalline materials and the well-developed technology of growing large Si wafers for microelectronic. Fig. 1.3-right shows the main planes of the cubic lattice, indicated by the Miller indexes. Each plane has a different inter-atomic distance,  $d_p$ . Table 1.1 summarizes the parameters of the strongest planar channels of the crystal of silicon at room temperature. Higher Miller indexes correspond to weaker crystal planes.

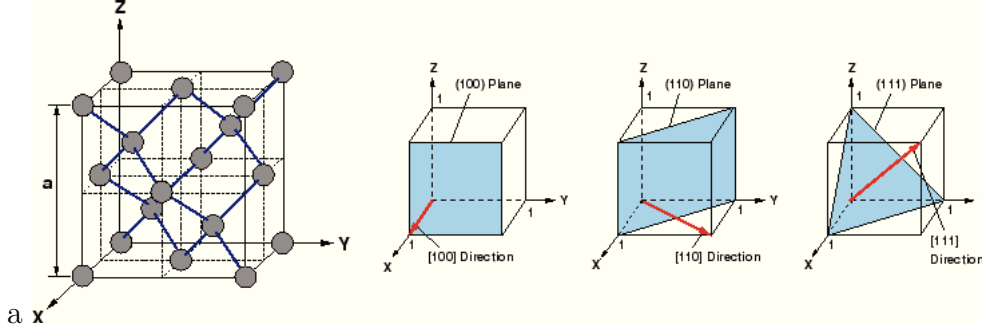


Figure 1.3: Left-The diamond cubic lattice is characterized by a tetragonal covalent bond: two identical fcc lattices, one inside the other and shifted along the bulk diagonal by one quarter of their length. Right-The main planes of the cubic lattice, i.e., (100), (110) and (111).

Plane	$d_p$ [Å]	$a_{TF}$ [Å]	$u_T$ [Å]	$U(x_c)$ [eV]	$U'(x_c)$ [GeV/cm]
Si		0.194	0.075		
(110)	1.92			16	5.7
(111)L	2.35			19	5.6
(111)S	0.78			4.2	3.5

Table 1.1: Parameters of some planar channels of silicon crystal. The potentials  $U$  are given at the distance  $x_c = d_p/2 - 2u_T$  in the Molière approximation [42].

Fig. 1.4 displays some examples of the interplanar potential energy of positively charged particles interacting with the (110) and (111) planes, which are the most commonly used for *channeling experiments*, due to the generation of the largest potentials. The harmonic approximation  $U \sim x^2$ , plotted with a dashed line in Fig. 1.4(a), fits the interplanar Molière potential rather well, and it is often used for analytic estimations. The planar potential-well depth in silicon is  $\sim 20$  eV.

Fig. 1.5 shows the scheme of continuous planar potential for either positive (a) or negative (b) particles in the case of a silicon crystal oriented along the (110) planes. The harmonic approximation does not hold for the planar potential for negatively charged particles, being opposite to that for positive particles and thus more similar to an "inverted parabola" [4].

## Planar Channeling

It has been shown that the transverse motion of a charged particle with a small angle with respect to atomic planes can be well described by the approximation of continuous

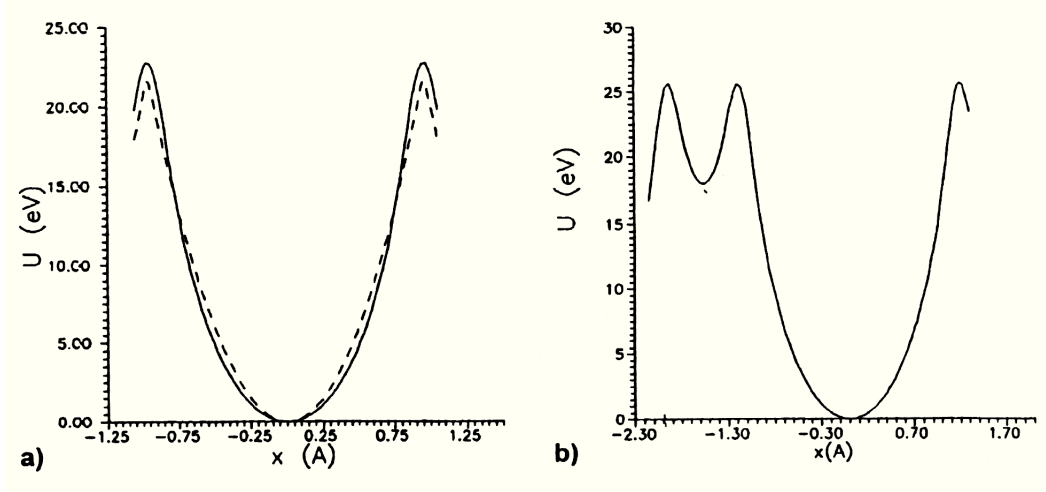


Figure 1.4: The interplanar Molière potential for (a) the Si channels (110) and (b) the Si channels (111) for positively charged particles with  $Z_i=1$  (solid lines). The dashed line represents the harmonic approximation. In the crystal with the (111) orientation the large distance  $d_p^L = 2.35 \text{ \AA}$  between the atomic planes changes periodically into a small one  $d_p^S = 0.78 \text{ \AA}$  [42].

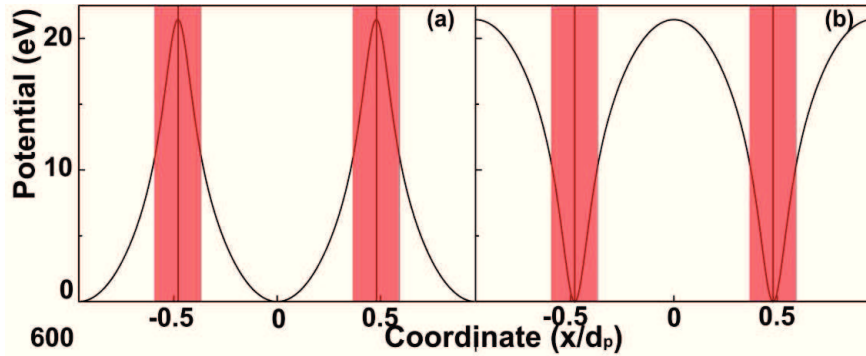


Figure 1.5: Planar potentials experienced by positive (a) and negative (b) particles channeled in the field of (110) silicon planes. Shaded regions highlight the regions of high nuclear density (nuclear corridors), vertical lines inside those regions show the positions of atomic planes [46].

potential. It has been also explained that the electric potential of atomic planes forms potential wells. In this section, we describe the case in which a particle may be *channeled*, when its transverse momentum is not sufficient to exceed the barrier of a neighboring channel. This process is schematically shown in Fig. 1.6. The planar channeling motion results to be very different from the random motion of a particle crossing an amorphous medium or a misaligned crystal [42]. In the latter case, there are two main sources of

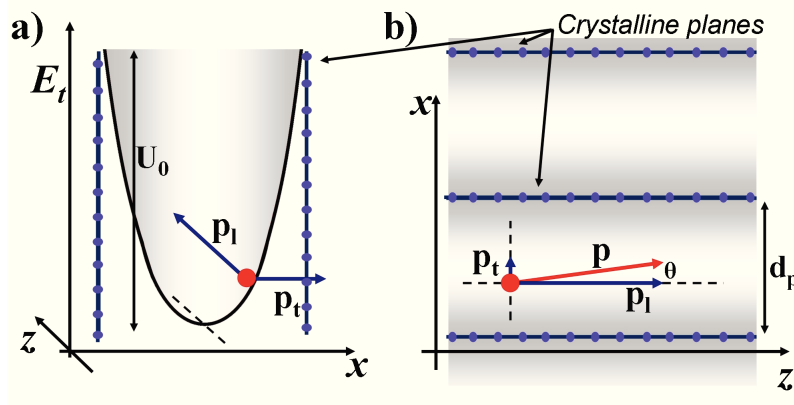


Figure 1.6: a) A positive particle bound in the interplanar continuous potential. b) Top view of the channel. Here are highlighted the components of the transverse ( $p_t$ ) and longitudinal ( $p_l$ ) momentum of the particle with respect to the plane direction.  $\theta = p_t/p_l$  is the small misalignment angle with respect to the crystal plane.

**energy loss** by a charged particle in a medium: electronic stopping and nuclear stopping [1]. Electronic stopping is caused by electronic inelastic collisions in which the particle excites or ejects atomic electrons, with a consequent loss of energy. Since electrons are light particles, the corresponding momentum transferred to the medium is small. On the other hand, nuclear stopping arises from nearly-elastic collisions with nuclei, with transfer of both energy and momentum. We assume here that the nuclei are much more massive than the incident particles so that the small energy transfer to the nucleus is negligible [47]. Ignoring spin effects and screening, these collisions are individually governed by the well-known Rutherford formula where  $\frac{d\sigma}{d\Omega} \propto 1/\sin^4(\theta/2)$ , hence the vast majority of these collisions results in a small angular deflection of the particle (multiple Coulomb scattering), causing a random zigzag path through the medium. The cumulative effect of those small-angle scatterings is, however, a net deflection from the original particle direction. As a consequence, particle deflection can be mainly ascribed to nuclear collisions, in which stronger forces and heavier masses are involved. At relativistic energies, electronic stopping is completely dominating, being nuclear stopping  $\sim 10^3$  times smaller. A quantum perturbation treatment of the excitation of the atomic system may then be applied (Bethe-Bloch treatment) [1].

For light particles, such as electrons and positrons, the radiative losses become dominant in the energy loss spectrum at relativistic velocities [47].

The particle dynamics under channeling is quite different from the amorphous or misaligned case. Moreover, in such a case the particle dynamics depends on the charge's

sign. Indeed, a channeled positive particle moves between two atomic planes formed by atomic nuclei, thus reducing the possibility to experience nearly-elastic scattering with nuclei themselves. Furthermore, since most of the electronic levels are close to the nuclei (core electrons), a channeled positive particle moves in a medium of electrons with reduced density determined by the valence electrons only. In the opposite case of negatively charges, a channeled particle oscillates around atomic planes, in the region of high nuclear and electronic densities, thus increasing the probability of close collisions with nuclei and core electrons as compared to channeled positive particles. Finally, it has been demonstrated that channeling, and coherent interactions in general, increase the probability of a photon to be radiated (the creation of a pair), leading to an increase of energy loss per unit of length. This argument is treated in the next chapter, while in section 1.1.4 a brief description of the phenomena that contribute to the stopping and, hence, to the energy loss of high-energy charged particles in crystals is presented.

In the limit of high particle momenta the motion of channeled particles (or in general in the approximation of continuous potential) may be considered in the framework of classical mechanics, even though the single process of scattering is a quantum event. The classical approximation works better at high-energy for two reasons. First of all, the wavelengths of incident particles are sufficiently small to prevent the formation of interference patterns of waves. Secondly, classical mechanics is applicable thanks to the large number of energetic levels in the planar potential well (in analogy with the quantum harmonic oscillator). The quasiclassical estimate of the number of levels in the one-dimensional potential well at planar channeling yields  $N \sim \frac{d_p}{\lambda_c} \sqrt{\frac{EU_0}{m^2}} \gg 1$ ,  $\lambda_c$  being the Compton wavelength,  $E$  the particle energy,  $U_0$  the potential well depth and  $m$  the particle mass. The second condition is always fulfilled for heavy particles, such as ions and protons, but for light particles (electrons, positrons) the classical approach starts to work in the 10 – 100MeV energy range [4].

In the framework of classical mechanics, one can write the classical law of conservation of the total energy adapted to the case of particle motion in the continuous planar potential (see eq. 1.1). When the transverse component  $p_x$  of the particle momentum  $p$  is much smaller than the longitudinal component  $p_z$  (*i.e.*  $\theta \approx tg\theta = p_x/p_z \ll 1$ ), the total conserved energy  $E$  of the system can be written in the form:

$$E = \sqrt{p_x^2 c^2 + p_z^2 c^2 + m^2 c^4} + U(x) \simeq \frac{p_x^2 c^2}{2E_z} + E_z + U(x) = const, \quad (1.10)$$

being  $E_z = \sqrt{p_z^2 c^2 + m^2 c^4}$  a conserved quantity, since the potential energy  $U(x)$  is in-

dependent of  $z$ . As a consequence, the transverse energy,  $E_T = \frac{p_x^2 c^2}{2E_z} + U(x)$ , must be conserved too. Being  $p_x \simeq p_z \theta$  and assuming  $E_z \approx E$ ,  $p_z \approx p$ , using the known relation  $pc^2 = vE$ , where  $v$  is the particle velocity, we may rewrite  $E_T$  as:

$$E_T = \frac{pv}{2}\theta^2 + U(x) = \text{const.} \quad (1.11)$$

The particle trajectory is obtain by the integration of

$$dz = \frac{dx}{\sqrt{2/pv[E_T - U(x)]}}. \quad (1.12)$$

Rewriting eq. 1.11 by taking into account that  $\theta = dx/dz$  one obtain

$$E_T = \frac{pv}{2}\left(\frac{dx}{dz}\right)^2 + U(x) = \text{const} \quad (1.13)$$

Differentiating with respect to  $z$  and dividing all terms by  $\theta$ , the result for the one-dimensional transverse motion in the potential  $U(x)$  is:

$$pv \frac{d^2x}{dz^2} + \frac{d}{dx}U(x) = 0 \quad (1.14)$$

Eq. 1.14 describes the particle transverse oscillation of the particle motion under the influence of the planar potential  $U(x)$ .

In the case of positively charged particle, in Sec. 1.1.2 it has been shown that the harmonic approximation  $U(x) \simeq U_0 \left(\frac{2x}{d_p}\right)^2$  for the interplanar potential can be used. In this case the solution of eq. 1.14 is a sinusoidal oscillation:

$$x = \frac{d_p}{2} \sqrt{\frac{E_T}{U_0}} \sin\left(\frac{2\pi z}{\lambda} + \phi\right) \quad (1.15)$$

with the oscillation period being  $\lambda = \pi d_p \sqrt{pv/2U_0}$ .

In the case of negatively charged particles, the harmonic approximation for  $U(x)$  never holds, therefore a single period cannot be defined. Nevertheless, the main features of the electron motion at planar channeling can be easily observed by means of the simple model of "inverted parabola potential" [4]:

$$U(x) \simeq U_0 \left[1 - \left(1 - \frac{2|x|}{d_p}\right)^2\right]. \quad (1.16)$$

Within this simplified model the period of each channeled particle depends on its transverse energy inside the potential well,  $E_T$ , being  $\lambda = d_p \sqrt{pv/2U_0} \ln \left| \frac{1+\sqrt{E_T/U_0}}{1-\sqrt{E_T/U_0}} \right|$ .

The particle remains trapped within the channel if its transverse energy is lower than the potential-well depth  $U_0$  (defined at the distance  $d_p/2$  from the center of the potential well):

$$E_T = \frac{pv}{2}\theta^2 + U(x) \leq U_0. \quad (1.17)$$

If a particle moves along the center line of a channel ( $x = 0$ ,  $U(0) = 0$ ), with oscillations around the center of the channel, from eq. 1.17 the limiting angle of capture is obtained:

$$\theta_c = \sqrt{\frac{2U_0}{pv}}, \quad (1.18)$$

$\theta_c$  being the critical angle introduced by Lindhard, for both planar and axial channeling independently of the particle charge's sign.

## Dechanneling

The motion of channeled particles is affected by incoherent scattering with electrons and nuclei, which causes the non-conservation of the transverse energy  $E_T$  due to the contribution of a random scattering angle in a event of scattering. As a result  $E_T$  may become higher than the potential barrier, leading to the kick out of the particle from the channel (*dechanneling* process) [42, 46]. There are two main sources of dechanneling in crystals: the multiple quasi-elastic scattering with nuclei and the multiple inelastic scattering with electrons.

In a random system, the electronic scattering is usually neglected in many physical approximation and the incoherent scattering with nuclei can be well described by a multiple Coulomb scattering<sup>4</sup> (MCS) process. MCS can be roughly represented by a Gaussian for small deflection angles [48], where the value

$$\theta_0 = \theta_{plane}^{rms} = \frac{13.6 MeV}{\beta c p} Z \sqrt{\frac{t}{X_0}} \left[ 1 + 0.038 \ln \left( \frac{t}{X_0} \right) \right] \quad (1.19)$$

is the width of the approximate Gaussian projected angle distribution,  $p$ ,  $\beta c$  and  $Z$  are the momentum, velocity and charge number of the incident particle, and  $t/X_0$  is the true path length in radiation length unit. A more accurate theory was given by Moliere [49], which

<sup>4</sup>We are neglecting the strong interactions that may also contribute to multiple scattering for hadronic projectile.

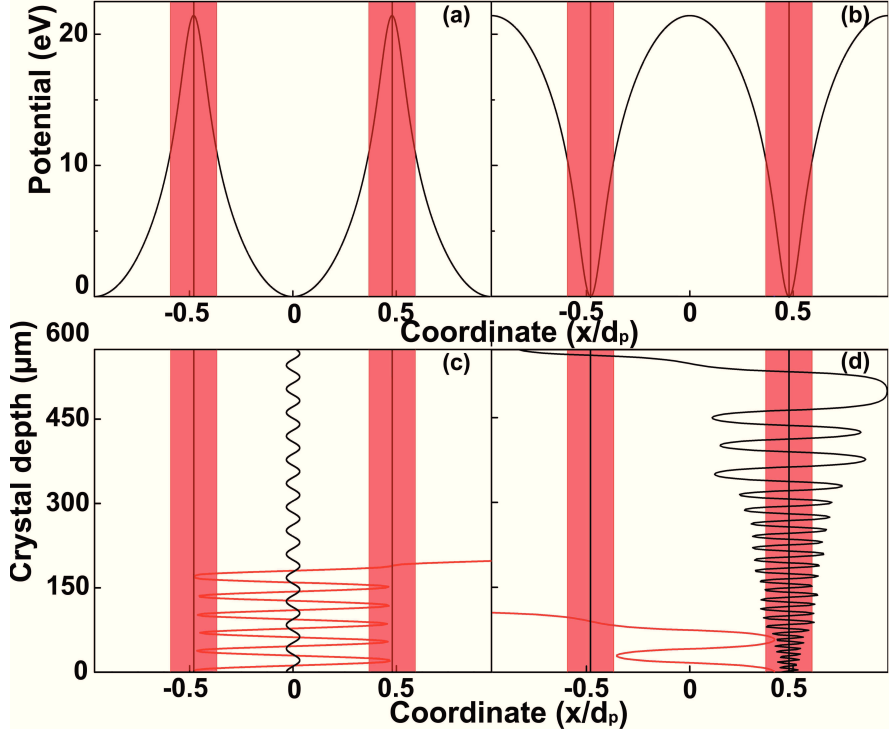


Figure 1.7: (a-b) planar potentials experienced by positive and negative particles channeled in the field (110) silicon planes. Shaded regions highlight the regions of high nuclear density (nuclear corridors), vertical lines inside those regions show the positions of atomic planes. (c) Trajectories of two 150 GeV/c  $\pi^+$ : the trajectory of the particle with larger oscillation amplitude is for a particle whose impact parameter lays inside the region of high nuclear density (i.e. the particle is in unstable channeling state). Such a particle is dechanneled after traversing a short distance in the crystal. The other trajectory refers to a particle impinging far from atomic planes (such particle is in stable channeling states). (d) trajectories of two 150 GeV/c  $\pi^-$ : all negative particles pass through the high-atomic density regions and are subject to nuclear dechanneling [46].

takes into account the large scattering angles ( $>$  a few  $\theta_0$ ) leading to larger tails that a Gaussian distribution does.

In the case of a crystalline material, it is not always possible to disregard the contribution of multiple scattering with electrons. For instance, for planar channeled positive particles, two mechanisms of dechanneling have been identified, i.e., nuclear and electronic dechannelings. Indeed, when the incidence angle of a particle with the channel direction is less than  $\theta_c$  but close to the nuclei (as close as  $\sim a_{TF} \sim u_T$ ), the scattering from the nuclei itself rapidly removes the particle from the channeling mode, i.e., nuclear dechanneling. We can approximate the atomic density as a Gaussian distribution with standard deviation equal to the atomic thermal vibration amplitude,  $u_T$ , (see eq. 1.8), and then assume that

the atomic density region interested by intense multiple scattering extends, for example, over  $2.5 u_T$ , the so-called nuclear corridor (see Fig. 1.7 (a) and (b)). As an example, since the (110) interplanar distance is  $d_p = 1.92 \text{ \AA}$ , about 19.5% of particles ( $5u_T/d_p \approx 0.195$ ) of a perfectly parallel beam are under unstable channeling states. For all these reasons, it can be introduced the critical transverse coordinate for planar channeling

$$x_c = \frac{d_p}{2} - 2.5u_T \quad (1.20)$$

and another common definition of the *critical angle of channeling*

$$\theta_c = \sqrt{\frac{2E_c}{pv}} \quad (1.21)$$

where  $E_c = U(x_c)$  is the critical transverse energy. Within this picture, particles impinging onto the crystal far from the atomic planes and with transverse energy  $E_T \leq E_c$  are found in stable channeling states. In such a case, a channeled particle is affected mainly by multiple scattering with electrons. Because the electronic density is rather uniform in the channel (due to valence electrons, see Fig. 1.8(a)) the process is independent from the transverse position,  $x$ , of the particle but depends only on  $E_T$ . If no interaction with electrons would occur, such particles never dechannel. Indeed, particles slowly increase their transverse energy via interaction with the electrons until they reach the region with high-atomic density and then experience interaction with the nuclei (electronic dechanneling).

With the aim of quantifying the strength of dechanneling, it is better to separate the cases of long and short crystals. In the case of long crystals, one may assume that all the positive particles approaching to the atomic planes as close as  $2.5u_T$  are rapidly dechanneled and, therefore, to study the dechanneling process for the rest of particles in stable channeling states. The particles trapped in the stable channeling states move far from nuclei. The transitions from (or to) the stable states are thereby possible mainly through electronic dechanneling. Since the most frequent collisions of such particle are soft, one can treat the non-conservation of transverse energy  $E_T$  for soft interactions in the framework of the diffusion theory starting from the Fokker-Planck equation [50]. Therefore, in the depth of the crystal the fraction of channeled particles decreases exponentially,  $N_{ch} \approx N_{st} \exp(-z/L_D)$ ,  $z$  being the crystal depth,  $N_{st}$  the total number of particles with  $E_T \leq E_c$  at  $z = 0$  and  $L_D$  the *dechanneling length*, which increases with the particle momentum. After some approximation and using the Lindhard potential for an atomic plane (eq. 1.4) in the case of high-energies ( $\gamma \gg 1$ ), an approximated value for the electronic

dechanneling length for positive particles channeled between atomic planes could be [42]:

$$L_D = \frac{256}{9\pi^2} \frac{pv}{\ln(2m_e c^2 \gamma / I) - 1} \frac{a_{TF} d_p}{Z_i r_e m_e c^2} \quad (1.22)$$

where  $m_e$  and  $r_e$  are the mass and the classical radius of an electron,  $I$  is the mean ionization energy and  $\gamma$  is the Lorentz factor. The diffusion approach remains valid for the electronic dechanneling, since the contribution of single strong collisions that may knock the particle out of the channeling mode at once remains small. This effect starts to become important for electronic dechanneling at energies  $\geq$  GeV.s

On the other hand, if a crystal is short enough to avoid the total loss of particles due to nuclear dechanneling, the numbers of channeled particles at coordinate  $z$ ,  $N_{ch}(z)$ , over the total number of particles,  $N_0$ , can be roughly estimated as in [51], where both the dechanneling processes, which lead to a decay in the number of channeled particles, are approximated by exponential functions as following:

$$N_{ch}(z) \approx N_{un} e^{-z/L_n} + N_{st} e^{-z/L_D} \quad (1.23)$$

where  $N_{un}$  and  $N_{st}$  are the number of particles in unstable and stable channeling states at the crystal entry face ( $z = 0$ ), respectively. For Si (110) at 300 K,  $N_{un} \sim 19.5\% N_0$  and  $N_{st} \sim 80.5\% N_0$ .  $L_n$  and  $L_D$  are the nuclear and electronic dechanneling lengths, respectively. The electronic dechanneling is a slower process than the one due to the strong nuclear collisions. As an example, Fig. 1.7 (c) shows trajectories of two 150 GeV/c  $\pi^+$  channeled in the (110) potential well depth [46]. The trajectory of the particle with larger oscillation amplitude is for a particle whose impact parameter lays inside the region of high nuclear density (i.e. the particle is in an unstable channeling state). Such a particle is dechanneled after traversing a short distance in the crystal. The other trajectory refers to a particle impinging far from atomic planes. Such particle founds in stable channeling state.

The electronic and nuclear dechanneling lengths could be measured in experiments, but it is not easy to distinguish the electronic long component from the nuclear short one, unless of being in special experimental conditions, e.g., through the usage of short bent crystals [51]. As an example, for 400 GeV/c protons interacting with Si (111) planes,  $L_D \sim 220$  mm [52], while  $L_n \sim 1.5$  mm [51].

The calculations seen above are valid in the case of motion of positively charged particles channeled between two crystallographic planes. For negative particles the planar potential is attractive and since the minimum of the potential well is located on the atomic planes, all

the particles with  $E_T < U_0$  at  $z = 0$  are readily directed toward the nuclear corridor, crossing the dense layers of atomic nuclei (see Fig. 1.7(b)-(d)). As a consequence, all negatively charged particles lie in unstable channeling states ( $N_{st} = 0$ ,  $N_{un} = N_0$ ) and the mechanism of dechanneling via interaction with valence electrons negligibly contributes to dechanneling with respect to nuclear dechanneling. The diffusion approach can be used to treat also the dechanneling of negative particles, in particular for electrons [53].

A simple way to estimate the number of channeled particles at depth  $z$  is [46]:

$$N_{ch}(z) \approx N_0 e^{-z/L_{neg}} \quad (1.24)$$

Since the probability of scattering with nuclei increases, it increases also the probability of dechanneling. For this reason, the total dechanneling length for negative particles  $L_{neg}$  is much shorter than the electronic dechanneling length  $L_D$  for positive ones according to the theoretical and the experimental data [2]. Indeed, it has been shown in [46] that  $L_{neg}$  is of the order of the nuclear dechanneling length for positively charged particles  $L_n$ . As an example, Fig. 1.7(d) displays the trajectories of two 150 GeV/c  $\pi^-$  channeled in the field of (110) Si planes. One can notice that all negative particles pass through the high-atomic density region and are subject to nuclear dechanneling, independently on their impact parameters with atomic planes.

To conclude, one should remember that the counterpart of the dechanneling mechanism is the feed-in process, or rechanneling, which may contribute in an important way to the refilling of the number of channeled particles. The reversibility rule [1] assures that for any trajectory of a particle in a crystal a time-reversed trajectory is possible. Therefore, as well as there are particles that leave channeling mode in the depth of a crystal, there are particles entering the channeling mode (*feeding in*). The mechanisms responsible for these two opposite processes are essentially the same, i.e., the incoherent scattering with nuclei and electrons.

### 1.1.3 Axial Channeling

The continuous approximation can be used also in the case of a particle aligned with the atomic strings. In such a case, a charged particle is influenced mostly by a crystal axis, which generates a stronger electric field than for a plane. According to Lindhard, the axial continuous potential averaged along the longitudinal coordinate of the string can be written in the form [42]:

$$U_{ax}(r) = \frac{Z_i Z e^2}{a_i} \ln \left( 1 + \frac{3a_{TF}^2}{r^2} \right) \quad (1.25)$$

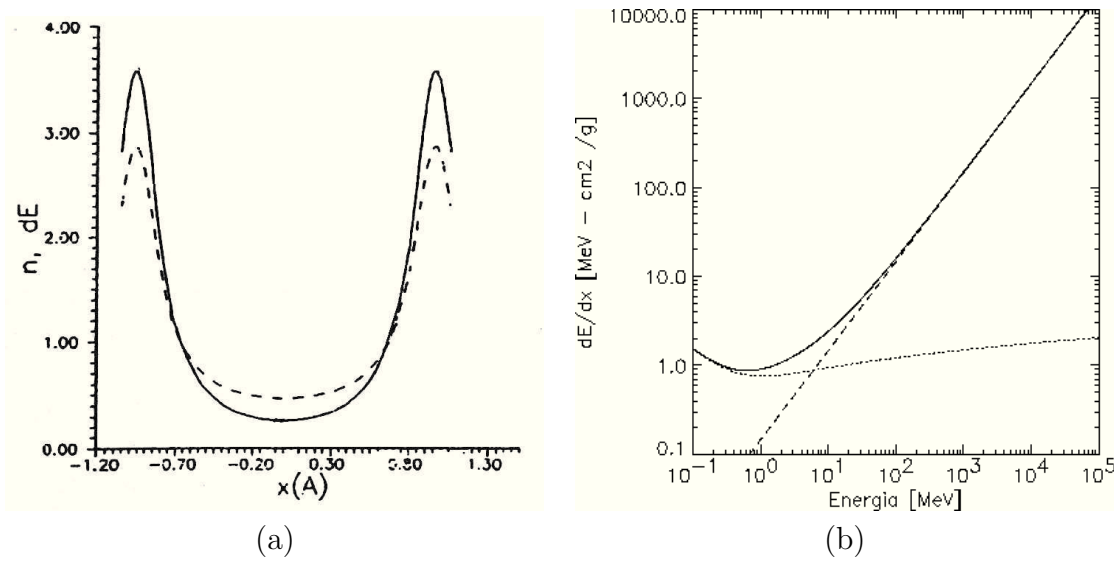


Figure 1.8: (a) The electronic density (*solid line*) and the mean ionization energy loss (*dashed line*) in an aligned crystal, normalized to the amorphous values, in Si(110). (b) Stopping power for electrons in tungsten (solid-line): bremsstrahlung contribution (dashed-line) and Bethe-Bloch one (dot-line). Adapted from [42]

where  $a_i$  is the interatomic spacing in the string and  $r$  is the distance from the particle to the axis (see Fig. 1.9).

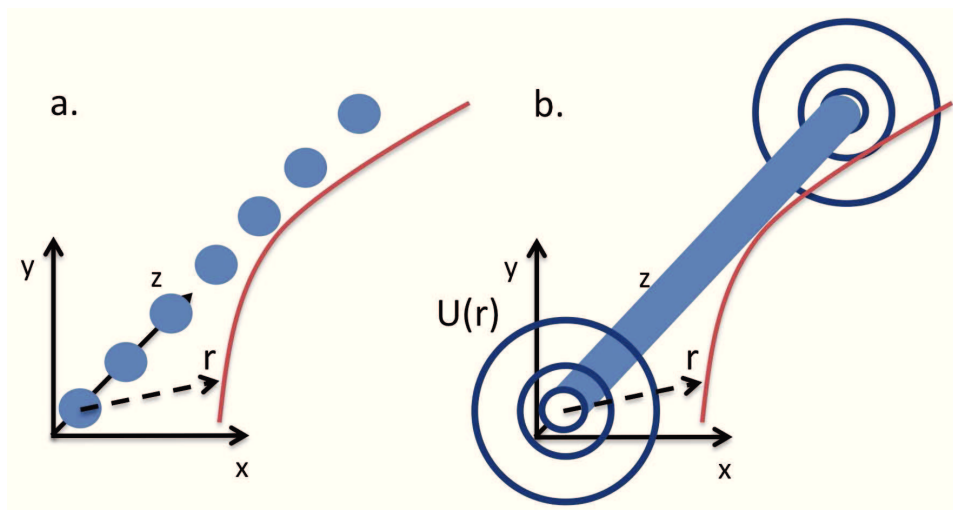


Figure 1.9: a) Trajectory of positive particle moving in a crystal aligned with respect to a crystal axis. b) Continuous potential  $U(r)$  is felt by the particle mainly due to the neighboring axis.

In the case of axial channeling, the particle motion in the field of  $U_{ax}(r)$  is characterized

by two conserved quantities, the angular momentum  $L$  and the transverse energy  $E_T$  in the transverse plane. If a particle impinging onto a crystal axis with a small angle  $\psi$ , with projections  $\psi_r = dr/dz$  directed toward the axis  $z$  and  $\psi_\phi = rd\phi/dz$  perpendicular to it ( $\psi^2 = \psi_r^2 + \psi_\phi^2$ ). The conserved transverse energy can be expressed as

$$E_T = \frac{pv}{2}\psi^2 + U(r) = \frac{pv}{2}\left(\frac{dr}{dz}\right)^2 + \frac{L^2}{2m\gamma r^2} + U(r), \quad (1.26)$$

$m$  being the particle mass. The particle motion in the axial field is then defined by the following equations

$$dz = \frac{dr}{\sqrt{2/pv[E_T - U(r)] - L^2/p^2r^2}}, \quad (1.27)$$

$$d\phi = \frac{L/r^2 dr}{\sqrt{2m\gamma[E_T - U(r)] - L^2/r^2}}. \quad (1.28)$$

### 1.1.4 Energy Loss

Energetic heavy charged particles in an amorphous substance (or a misaligned crystal), lose energy mainly in inelastic collisions with atomic electrons, i.e., through ionization energy losses. The *stopping power*  $dE/dx$ ,  $x$  being the depth penetration, is described by the Bethe-Bloch formula and the energy loss shows the Landau distribution form [47]. The frequent soft collisions, that cause only an excitation, provide a Gaussian-like peak in the energy loss spectrum, while the rare close hard collisions, in which the energy transferred is sufficient to cause ionization and eventually secondary ionization ( $\delta$  - rays), contribute to the long high-energy tail and to the spread of the energy-loss distribution.

When a positively charged beam is aligned with respect to atomic planes it could be divided in two parts: channeled beam (with  $x \leq x_c$ ) and random beam (with  $x > x_c$ ). The channeled beam moves in a region with lower electron density as compared to the amorphous case (see Fig. 1.8 (a)), so the contribution due to hard collisions is suppressed. For this reason both the average loss of energy and its spread are decreased compared to the amorphous case. A quantitative description of the position-dependent energy loss was given by Esbensen and Golovchenko [54]. On the contrary, since negatively charged particles oscillates around planes, the ionization losses for channeled particles are comparable to the one for amorphous medium. In fact, in the case of axial channeling, negatively charged particles oscillate around axes, thus seeing an increased atomic density as compared to amorphous case. The result is an increase of energy loss as compared to random orientation (about the 20% more for GeV negative particles) [55].

Furthermore, because of their small mass, electrons and positrons not only lose energy in collisions with atoms, but also in the emission of electromagnetic radiation arising from scattering in the electric field of a nucleus (**Bremsstrahlung**) [6]. At energies larger than the critical one [56],

$$E_c \approx \frac{610 \text{ MeV}}{Z + 1.24}, \quad (1.29)$$

bremsstrahlung dominates in the energy losses of electrons and positrons as compared to ionization losses (see in Fig. 1.8(b)). In silicon,  $E_c \sim 40$  MeV.

As introduced before, the e.m radiation emitted by  $e^+/e^-$  through coherent interactions is more intense than for common bremsstrahlung in an amorphous medium. Such increase occurs not only for channeling, thereby called *channeling radiation* (CR) [11], but also in the case of particles that move in over-barrier states in the fields of several atomic planes or axes [9]. A qualitative description on the process of e.m. radiation emission in oriented crystals is presented in Chapter 2.

## 1.2 Coherent interactions in bent crystals

### 1.2.1 Planar Channeling in a bent crystal

The possibility to steer charged particle beams with bent crystals was proposed by Tsyganov in 1976 [12]. He supposed that, if a crystal is slightly bent, the channeled particles would follow the direction of the bent atomic planes (or axes), thus deviating from the initial direction by an angle equal to the crystal bend<sup>5</sup>. In case of macroscopic curvatures (from  $cm$  to several  $m$ ), the bending has a negligible effect on the planar (axial) potential in the range of angstroms in the laboratory inertial frame (see Fig. 1.10(a)). On the contrary, from the point of view of the non-inertial reference frame (comoving with a particle channeled with zero transverse momentum along the bent planar channel) a centrifugal fictitious force appears due to the bending of the crystal (see Fig. 1.10(b)). In the lab-frame, a particle enters in the channel aligned with the crystal planes, i.e. with transverse momentum  $p_t = 0$ , and during the motion the particle acquires a non-zero  $p_t$  in order to follow the channel bending. In other words the interplanar continuous potential exerts a force that modifies the particle momentum. On the other hand, in the comoving reference frame the particle momentum direction does not change, but a centrifugal force directed towards the external side of the channel appears. In the comoving frame, where  $z$  axis follows the direction of bent atomic planes and  $x$  is the transverse coordinate defined with

<sup>5</sup>In this Section, we follow mainly the book [42].

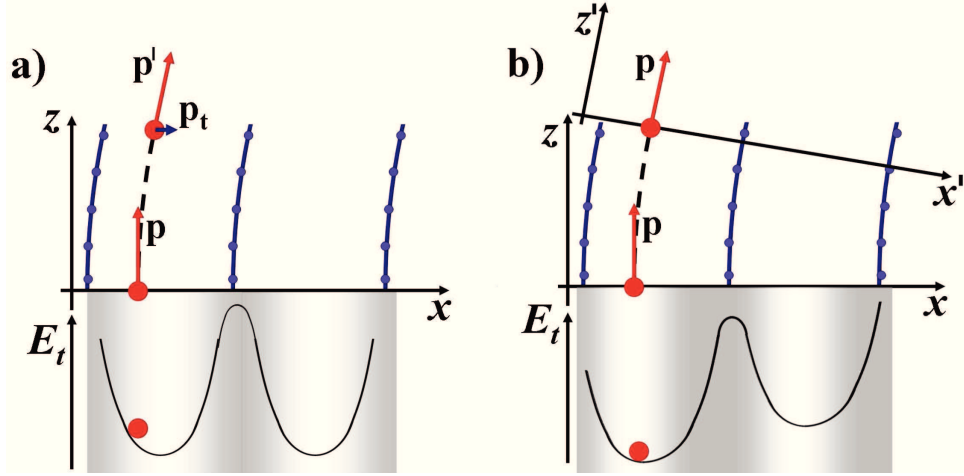


Figure 1.10: Scheme of the channeling motion of a positive particle that enters in the channel aligned with respect to the crystal planes: a) in the laboratory inertial frame; b) in the non inertial comoving reference system which rotates with the particle; the centrifugal force appear. Adapted from [43].

respect to atomic planes at some point  $z$ , the equation of motion 1.14 for a channeled particle becomes:

$$pv \frac{d^2 x}{dz^2} + U'(x) + \frac{pv}{R(z)} = 0, \quad (1.30)$$

$x$  and  $z$  being the transverse and longitudinal coordinates in the comoving frame, respectively, while  $1/R(z)$  is the local curvature of the channel. If the bending radius  $R$  is independent from  $z$ , the particle moves as if it was in an *effective* interplanar potential of the form:

$$U_{eff}(x) = U(x) + \frac{pv}{R}x, \quad (1.31)$$

with a transverse energy  $E_T = \frac{pv}{2}\theta^2 + U_{eff}(x)$ .

Fig. 1.11 shows some examples of  $U_{eff}(x)$  for different  $pv/R$  ratios for the Si planes (110), as compared to the case of unperturbed potential  $U(x)$  for positive particles. If  $pv/R$  increase, the depth of the effective potential well decreases and its minimum value is shifted towards the atomic plane. For these reasons, at some critical  $(pv/R)_c$  the well completely disappears and channeling becomes impossible. The critical radius of curvature is defined by the maximal interplanar electric field  $\varepsilon_{max}$  near the atomic planes:

$$R_c = \frac{pv}{e\varepsilon_{max}}. \quad (1.32)$$

For instance,  $e\varepsilon_{max}$  is about 6, 12 and 48 GeV/cm for (110) planes in Si, Ge and W,

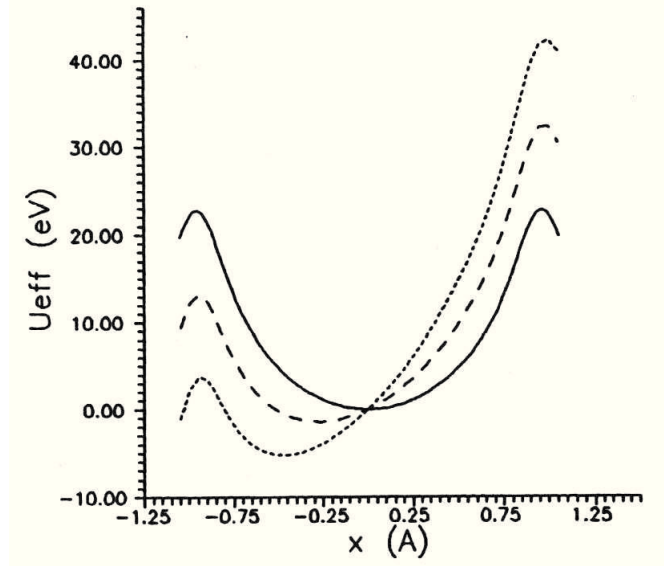


Figure 1.11: The interplanar potential in Molière approximation for Si (110) (*solid line*) and the effective potential for  $pv/R$  of 1 GeV/cm (*dashed line*) and 2 GeV/cm (*dotted line*) [42].

respectively. The critical energy in the case of bent crystal is  $E_c^b(R_c/R) = E_c(1 - R_c/R)^2$ , where  $E_c$  is the critical transverse energy in a straight crystal. Following this definition, it is possible to define the critical angle for bent crystals:

$$\theta_c^b(R_c/R) = \theta_c(1 - R_c/R), \quad (1.33)$$

$\theta_c$  being the critical angle for a straight crystal. One can notice that  $\theta_c^b$  is reduced of a factor  $(1 - R_c/R)$  from  $\theta_c$ .

## 1.2.2 Dynamics of over-barrier particles in bent crystals

If a charged particle moves within the crystal volume with a small angle (nearly aligned) to the atomic planes ( $\theta \ll 1$ ), but with a transverse energy larger enough to avoid channeling (over-barrier particles), its dynamics is influenced by the continuous potential and shows special features if the crystal is bent [16]. More precisely, two different effects have been discovered:

- Volume reflection (**VR**);
- Volume capture (**VC**).

Fig. 1.12 shows the scheme of the different possible planar coherent interactions between a charged particle and a straight or a bent crystal. Fig. 1.12(a)-(c) represents the motion of an unchanneled positive particle and a channeled one in a straight crystal in the plane  $(x, E_T)$  (a) and in the plane  $(x, z)$ , (c). On the other hand, in Fig. 1.12(b)-(d) the motion of positive particles in channeling, VR and VC conditions is shown in the planes  $(x, E_T)$  and  $(x, z)$ . In next paragraphs the VR and VC effects are described.

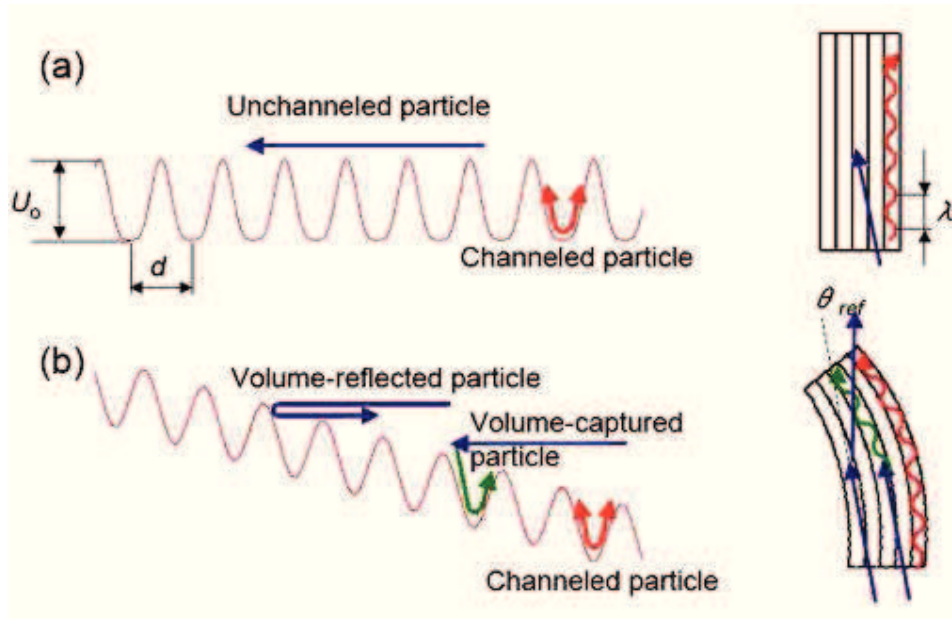


Figure 1.12: (a)-(c) Channeled and unchanneled particle in a straight crystal; (b)-(d) particle in channeling, VR and VC conditions in a bent crystal [20].

### Volume Reflection

In a bent crystal, even if a particle enter at crystal with an angle exceeding the critical one introduced by Lindhard, i.e. being over-barrier, its trajectory may become tangential to the crystallographic planes during the motion (and so tangential to the planar potential) due to the curvature of the plane itself (see Fig 1.13)). VR consists in the reversal of transverse momentum of over-barrier particles by the interaction with the planar potential barrier at the tangency point <sup>6</sup>. As a result, volume-reflected particles are deflected by an angle of the order of the Lindhard angle  $\theta_c$  to a direction opposite to that of crystal bending. In other words, in a bent crystal not only channeled but also unchanneled particles can be deflected. The angular acceptance for VR is equal to the bending angle of the crystal ( $l/R$ , where  $l$

<sup>6</sup>In this section we will follow mainly the paper [29].

is the crystal length) because any particle with an angle of incidence  $\theta_c < \theta_{in} < l/R$  will become tangent to bent crystal planes at some depth of the crystal. VR was experimentally proved to work for either positively [33, 34] or negatively [35] charged particles .

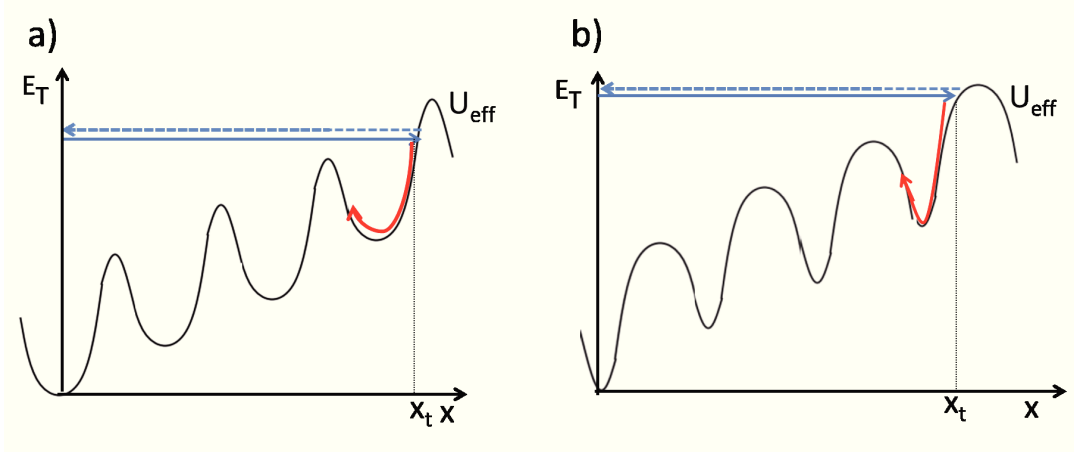


Figure 1.13: Reflection and capture of a charged particle in the crystal volume at the comoving transverse coordinate  $x_t$ . Phase space of the particle transversal energy as a function of  $x$  comoving with the bent planes either for positive (a) or negative (b) particles.

For large bending radius ( $R \gg R_c$ ), the deflection angle for VR, is about  $\theta_{VR} \approx 2\theta_c$ , for positively charged particles, while being smaller for negative particles, due to the shape of the effective interplanar potential [16]. Indeed, the reflecting region for a negative particle (between the planes) is nearly flat and the particle has to accomplish a longer path near turning points as compared to positive particles (see Fig. 1.13(b)).

If the curvature increases, the reflective area,  $\Delta U$ , increases (see Fig. 1.14), leading to deflection angles  $\theta_{VR}$  below  $2\theta_c$ . This can be ascribed to the fact that reflection may occur in points in which the interplanar potential is less intense. On the other hand, the increasing in the reflective area, increases the VR deflection efficiency [57].

Summarizing, VR shows a wider angular acceptance with respect to planar channeling, while a smaller angular deflection ( $\theta_{VR} \sim \theta_c$ ). With the aim of increasing the deflection angle of VR while maintaining a large angular acceptance, the possibility to exploit the effect of a multi-VR in a series of bent crystals or in a single crystal has been suggested and experimentally validated. Section 1.2.3 is dedicated to the description of this second case.

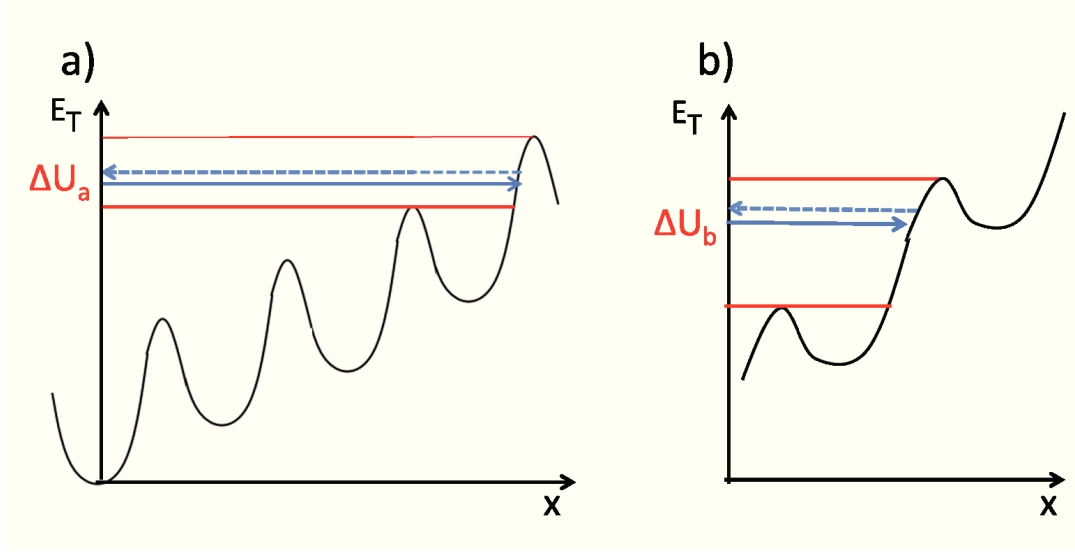


Figure 1.14: (a) and (b) are the phase spaces of the particles transversal energy, with  $R_a > R_b$ . The reflective area  $\Delta U_a < \Delta U_b$ .

## Volume Capture

In section 1.1.2, the dechanneling (*feeding out*) mechanism in a straight crystal has been described. The reversibility rule assures that if some particles leave the channel, there have to be particles entering in the channeling mode (*feeding in*) [1]. The feeding in/out processes are caused by the incoherent scattering that may change the transverse energy of the particle (see Fig. 1.13 red lines). More in details, the feeding out (dechanneling) is the transition of a particle from the channeled to the beam ('over barrier'), while the feeding in (rechanneling) describes the transition of a particle state from the random beam into a channeled state.

*Volume capture* is the feed-in process in bent crystals [31, 58]. The above paragraph painted out that when a beam passes through a bent crystal, a large part of the beam is reflected in the region of tangency with the bent planes. This is not the only type of motion possible for these particles. Indeed, a fraction of such particles are captured into the planar channel due to incoherent scattering with crystal atoms. In other words, VC is the mechanism that generates VR inefficiency. Since VC has the same broad angular acceptance of VR, it is more efficient than the feeding-in mechanism in straight ones. As a result, in a bent crystal the feeding out mechanism increases according to the reversibility rule. For instance, in the case of positive particles the dechanneling probability increases in a bent crystal because of the decreasing of the potential well  $E_c$  ( $\theta_c$ ) and because channeled particles are shifted towards atomic planes.

VC probability depends strongly on the bending radius: it decreases when  $R$  decreases, in agreement with the increasing of the reflective area for VR (see Fig. 1.14).

### 1.2.3 Multiple Volume Reflection in One Crystal

With the aim of increasing the small deflection angle achievable through VR, while maintaining the high efficiency and large angular acceptance, one may take advantage of the multiple volume reflection inside one bent crystal (MVROC)<sup>7</sup>. The VR effect has been studied principally as reflection from individual lying of crystalline planes normal to the bending plane, here called *vertical planes*. MVROC may occur under near-axis alignment with the particle beam. Since a crystal axis is the intersection of crystal planes (as an example, Fig. 1.15 shows the  $\langle 111 \rangle$  crystalline axis as the intersection of various crystal planes), repeated VRs on each of them may occur as a particle moves at small angle with respect to a major axis. As a consequence, VRs from several lying of planes sharing the same axis sum up leading to significant deflection increase.

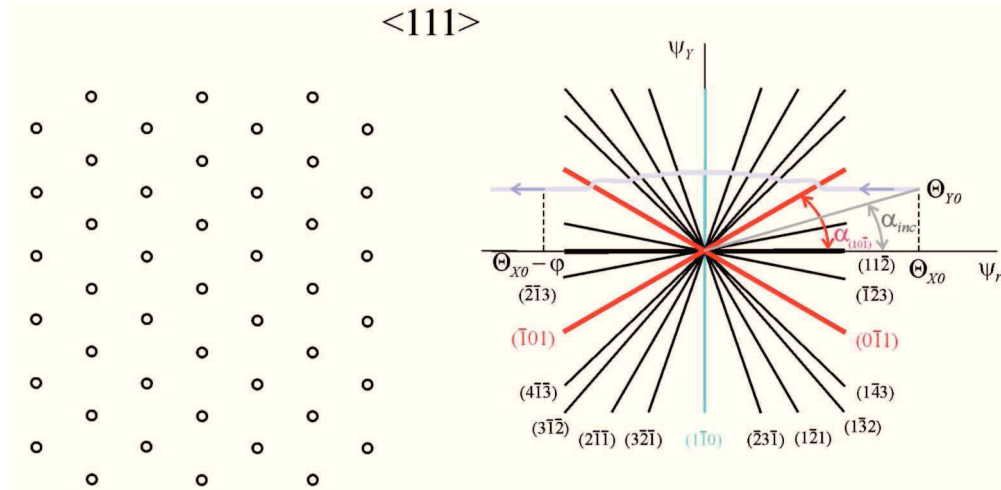


Figure 1.15: On the left: projections of the  $\langle 111 \rangle$  axes in a plane perpendicular to the axis (at the entry face of the crystal). On the right: projections of the plane in the plane  $(rY)$  or  $(\psi_r, \psi_Y)$  in the rotating reference frame.  $\alpha_{(-101)}$  is angle of inclination for the strong plane  $(-101)$  and  $\alpha_{inc}$  is the incidence angle of the particle in this plane. Adapted from [59].

Particle motion in the laboratory reference frame is studied in a cartesian coordinate system  $XYZ$  with the entry face of the crystal lying on the  $XY$  plane and  $Z$ -axis being parallel to a set of crystal axes at the latter (see Fig. 1.16). In this way the horizontal plane

<sup>7</sup>In this section we follow mainly the work presented in [59, 60]

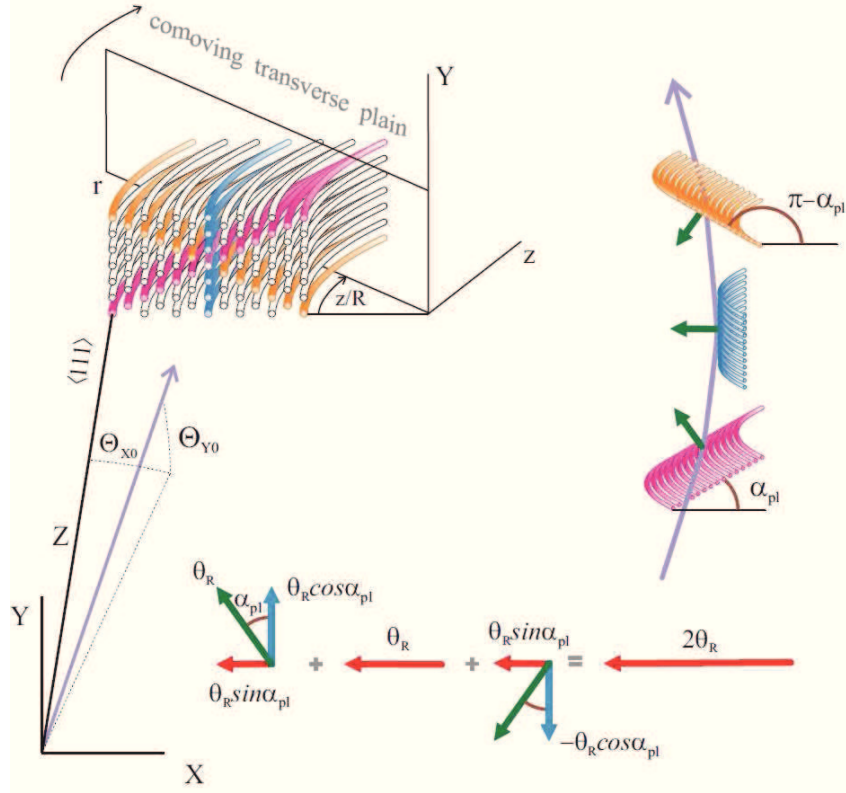


Figure 1.16: Particle which hits a crystal at small angles  $\Theta_{X0}, \Theta_{Y0}$  with respect to crystal  $\langle 111 \rangle$  axes experiences VRs from both the *vertical plane*, (1-10) and skew planes. The comoving reference frame  $rYz$  turns with the bent axis direction when a particle moves through the crystal. Adapted from [59].

$XZ$  is parallel to the plane of crystal bending. The description of particle reflection and channeling by skew planes in the reference frame  $rYz$ , comoving with a particle channeled with zero transverse momentum along bent crystal axes, should be used. Initial values of angles  $\psi_r$  and  $\psi_y$  are equal to those of particle incidence  $\Theta_{x0}, \Theta_{y0}$  with respect to the crystal axis at the entry face of the crystal (see Figs. 1.15 and 1.16). Since the angle  $\psi_r \simeq \Theta_{x0} - z/R$  decreases with  $z$  because of the crystal curvature ( $1/R$ ), the vector  $\psi = (\psi_r, \psi_y)$  becomes subsequently parallel to different layers of planes. Interaction with each of them is accompanied by VR in the direction normal to the plane at the tangency points and opposite to that of the crystal bending. As an example, Fig.1.17 shows a multi-reflected trajectory of a 120 GeV/c positron in the plane  $(\psi_r, \psi_y)$ .

The reflection onto skew planes results in deflection by the angles  $\theta_x = -\theta_R \sin \alpha_{pl}$  and  $\theta_y = \theta_R \cos \alpha_{pl}$  in the horizontal and vertical coordinate planes, respectively,  $\alpha_{pl}$  being the inclination of the skew plane and  $\theta_R$  the reflection angle by a plane bent with radius

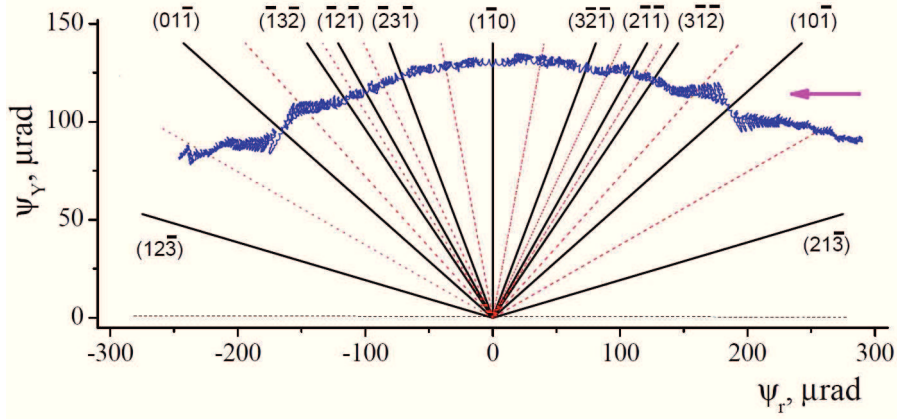


Figure 1.17: Particle trajectory in the plane  $(\psi_r, \psi_Y)$ : solid lines are the planes projections and dotted lines are the regions of influence of the planes.

$R/\sin \alpha_{pl}$  (as highlighted in Figs. 1.16 and 1.15(b)). Since  $\sin \alpha > 0$  for any  $0 < \alpha < \pi$ , all the horizontal deflection angles  $\theta_x$  sum up giving rise to considerable MVROC effect. On the contrary, since  $\cos(\pi - \alpha) = -\cos \alpha$ , the vertical deflections accompanying the reflection from symmetric skew planes with complementary inclination angles  $\alpha_{pl}$  and  $\pi - \alpha_{pl}$  compensate each other (see Fig. 1.17). Thus, if the horizontal incidence angle,  $\Theta_{x0}$ , and the bending angle of the crystal with thickness  $l$ ,  $\varphi = l/R$ , satisfy the condition

$$\Theta_{x0} = \varphi/2, \quad (1.34)$$

all the skew planes are involved in the VR process as symmetrical pairs, resulting in nearly zero net vertical deflection (see Fig. 1.17).

In order to reach the maximum deflection, it is necessary to involve the contribution of strongest skew planes in the multiple reflection process. The planes are involved when their inclination angle  $\alpha_{pl}$  does not exceed the inclination angle  $\alpha_{inc} = \arctan(\Theta_{y0}/\Theta_{x0})$  of the particle incidence plane to the axis. In more detail,  $\alpha_{inc}$  represents the projection of the direction of a particle nearly aligned with the axis  $\langle hkl \rangle$  on the plane  $(hkl)$ . Eq. 1.34 allows rewriting this condition in the form

$$\varphi > 2\Theta_{y0} \cot \alpha_{pl}. \quad (1.35)$$

According to Eq. 1.35, the strongest skew planes  $(\bar{1}01)$  and  $(0\bar{1}1)$  sharing the  $\langle 111 \rangle$  axis are involved in reflection if  $\varphi > 3.46\Theta_{y0}$ . Finally, effective particle reflection from main crystal planes formed by crystal axes becomes possible when the vertical incidence angle  $\Theta_{y0}$ , which is the minimal angle of particle motion with respect to the crystal axis, exceeds

the axial channeling angle at least three-four times, assuring effective averaging of the axial field over the reflecting crystal plane they form and the avoiding of axial channeling.



## Chapter 2

# Electromagnetic radiation emitted by ultrarelativistic electrons and positrons in straight and bent crystals

The radiation emission of a photon by a charged particle in a single crystal, when the initial particle is moving at a small angle,  $\theta_0$ , with respect to the direction of a crystal axis or plane, considerably changes in comparison with an amorphous medium. For example, in Chapter 1, it has been shown that the interaction of a charged particle with the planar potential generates a periodical motion in the transversal direction. This is valid not only for planar channeled particles, which oscillate between/around planes depending on the charge's sign, but also for overbarrier particles that cross several planes with a periodical motion with period  $T = \theta_0 d$ ,  $d$  being the interplanar distance. Such a situation can be generalized also to the case of particle motion in the field of axes, leading to the statement that the periodical structure of the crystal is responsible for a change in the process of radiation generation as compared to the common case of bremsstrahlung in an amorphous medium. If a crystal is slightly bent, the particle dynamics is modified and so the process of radiation generation.

In this chapter, a brief qualitative description of e.m. radiation emission process in straight and bent crystals is introduced.

## 2.1 General features of emission of radiation by high-energy particles in straight crystals

In this Section, a brief description of the radiation emission process in straight crystals is given following mainly the book of Baier, Katkov and Strakovenko [4]. From the classical electrodynamics it is well known that an accelerating charged particle in an external electromagnetic field emits electromagnetic radiation [61]. In the case of ultrarelativistic particles, the radiation weakly depends on the longitudinal component of the external force with respect to the motion direction<sup>1</sup>, being  $\gamma^2$  times weaker than the transversal one [4, 61], where  $\gamma = \varepsilon/mc^2 \gg 1$  is the Lorentz factor,  $\varepsilon$  and  $m$  the particle energy and mass, respectively. Under these conditions, the longitudinal acceleration can be neglected and the radiation intensity can be determined by the transverse force (acceleration) only. As a result, the e.m. radiation is emitted mainly forward into a narrow cone, with opening  $\theta_\gamma \sim 1/\gamma$ , along the particle velocity.

In general [61, 62], the main features of the radiation processes of ultrarelativistic particle are determined by the ratio between the total deflection angle  $\Delta\vartheta$  in the external field and the typical radiation angle  $1/\gamma \ll 1$ . If  $\Delta\theta \ll 1/\gamma$ , the whole radiation emitted by the particle is contained within the narrow cone with an opening angle  $\sim 1/\gamma$  and it is determined by nearly the whole particle trajectory. On the opposite side, if  $\Delta\theta \gg 1/\gamma$ , in a given direction the particle radiates from a small fraction of its trajectory where its direction is changed by an angle  $\sim 1/\gamma$ . This fraction of trajectory is called the radiation formation length  $l = R/\gamma$ , where  $R$  is the instantaneous bent radius. If the external field does not vary too much along  $l$ , one may neglect the variation of the field within the formation length, thus considering the external field as constant. This is the case of *uniform field approximation*, which is typical of synchrotron radiation.

In the case of periodical or quasi-periodical motion, which is typical for many cases of interactions between charged particles and crystals<sup>2</sup>, these two limits can be rewritten by comparing the radiation formation length (coherence length) with the oscillatory period ( $\lambda$ ) of the particle motion:

- CASE 1:  $\lambda \ll l$ , the radiation is formed on many periods  $\lambda$  and interference phenomena play a fundamental role.
- CASE 2:  $\lambda \gg l$ , the radiation is formed inside each period, so that the total intensity

<sup>1</sup>This is not valid if the force is directed along the particle velocity.

<sup>2</sup>In this list, we exclude the chaotic motion typical of above-barrier particles in the field of many crystal axes [63].

of radiation is a non-coherent sum of intensities for each  $\lambda$ .

With the aim of understanding the qualitative features of radiation emitted in quasi-periodical motion, it is more convenient to work in the co-moving frame, in which the mean particle velocity is zero. If the transverse velocity of the particle,  $v_{\perp}$ , remains non-relativistic in the co-moving frame, the radiation features a *dipole* nature (the transverse displacement of a radiating particle along the formation length  $\Delta x \sim \Delta\theta l$  is small compared to the emitted wavelength [63]) and completely determined by the Fourier components of the particle velocity. This corresponds to CASE 1, for which few first harmonics, multiples of the frequency of the particle motion, are emitted, *i.e.*, the radiation is nearly monochromatic. The frequency of radiated photon in the laboratory reference frame is obtained through a Lorentz transformation (Doppler effect):

$$\omega \approx \frac{\alpha\omega_0}{1 - \mathbf{n} \cdot \mathbf{V}} \approx \frac{2\gamma^2\omega_0\alpha}{1 + \gamma^2\theta^2}, \quad (2.1)$$

$\omega_0$  being the frequency of the particle's motion in the laboratory frame,  $\theta$  the photon emission angle with respect to the mean velocity of particle  $\mathbf{V}$ ,  $\alpha$  the number of harmonics and  $\mathbf{n} = \mathbf{k}/\omega$  where  $\mathbf{k}$  is the photon wave vector.

When the particle motion in the comoving frame becomes relativistic, the nature of radiation changes. Higher harmonics are emitted and the radiation spectrum becomes nearly continuous (CASE 2). If one assumes that  $|\mathbf{v}_{\perp}| \ll V$ , the expression for the frequency of radiation becomes:

$$\omega \approx \frac{2\gamma^2\omega_0\alpha}{1 + \gamma^2\theta^2 + \rho/2}, \quad (2.2)$$

where  $\rho^3$  is the parameter which characterize the multipolarity of radiation:

$$\rho = 2\gamma^2\langle(\Delta\mathbf{v})^2\rangle \quad (2.3)$$

where  $\langle(\Delta\mathbf{v})^2\rangle = \langle\mathbf{v}^2\rangle - \langle\mathbf{v}\rangle^2$  is equal to the mean square transverse velocity of the particle  $\bar{v}_{\perp}^2$  and it is of the order of the deflection angle squared ( $\sim \Delta\theta^2$ ) on particle trajectory.

At  $\rho \ll 1$  the radiation features a **dipole-like** nature, while at  $\rho \sim 1$  an important contribution is given by high harmonics. In the limit case,  $\rho \gg 1$ , mainly high harmonics are emitted and the radiation becomes **synchrotron-like**. As stated before, in the latter limit the radiation is formed over a short section of the particle trajectory,  $l$ , during the short time  $1/|\dot{\mathbf{v}}|\gamma$ . If one takes into account the Doppler effect, the characteristic frequency of the radiation is  $\omega \sim |\dot{\mathbf{v}}|\gamma^3$  which is typical of synchrotron radiation.

<sup>3</sup> $\langle \dots \rangle$  denotes averaging over time.

The two limit cases seen above about the type of radiation emitted by a charged particle in a quasi-periodical motion can be deepened in the case of interaction with a crystalline medium.

When an electron or positron moves inside a crystal with a small angle of incidence,  $\theta_0$ , with respect to atomic planes or axes, its maximum deflection angle,  $\Delta\theta$ , depends strongly on  $\theta_0$  itself. At an angle of incidence in the range  $\theta_0 \leq \theta_c$ , particles are captured into channels or low above-barriers states, thus  $\Delta\theta \sim \theta_c$ . On the other hand, if  $\theta_0 \gg \theta_c$ , the particles move high above the potential barrier, for which the approximation of rectilinear trajectory can be used.

A characteristic angle of this type of problems can be introduced as

$$\theta_v \equiv \frac{U_0}{mc^2} \quad (2.4)$$

$U_0$  and  $m$  being the potential well depth and electron mass, respectively. The value  $\theta_v$  is independent from the electron/positron energy.

For a given  $\theta_0$ , the type of radiation process depends strongly on the particle energy  $\varepsilon$ . Four regions of interest can be identified. As stated in Chapter 1, at very-low energies (up to several MeV in the axial case and up to tens of MeV in the planar case in *Si*) the number of energy levels inside  $U_0$  is limited and the particle motion cannot be described by classical mechanics. This energy range is out of the interest of this work of thesis.

In the hundreds MeV energy range,  $\theta_v \ll \theta_c \ll \theta_\gamma$ . The e.m. radiation is of dipole nature ( $\rho \ll 1$ ) for any incidence angle  $\theta_0$ . If  $\theta_0 \gg \theta_c$ , the coherent bremsstrahlung (CB) theory can be used. The CB theory is based on the Born approximation to the potential of a crystal and it is applicable in condition of emission of dipole radiation and in the validity of the rectilinear trajectory approximation. As shown in [63], the first Born approximation cannot be used in the case  $\theta_0 \sim \theta_c$ .

At higher beam energies, the relation between the characteristics angles becomes  $\theta_v \sim \theta_c \sim \theta_\gamma$ . In this case the radiation process is everywhere of dipole nature, except in the case of channeling with  $\theta_0 < \theta_c$ . The channeling radiation (CR) starts to become non-dipole-like ( $\rho \sim 1$ ) at  $\varepsilon > 5GeV$  ( $\varepsilon > 1GeV$ ) in the fields of strongest Si planes (axes).

At very-high energy,  $\theta_v \gg \theta_c \gg \theta_\gamma$ . As a consequence, for  $\theta_0 \ll \theta_v$  the synchrotron-like radiation applies ( $\rho \gg 1$ ), while the CB theory can be used in the opposite case for which  $\theta_0 \gg \theta_v$  and  $\rho \ll 1$ . The intermediate case  $\theta_0 \sim \theta_v$  implies that  $\rho \sim 1$  and the dipole emission condition is no longer obeyed. In this range of energies ( $\varepsilon \simeq 100GeV$ ), hard photon ( $\hbar\omega \sim E$ ) emission becomes possible and, therefore, it is necessary to take into account the quantum recoil in the process of radiation emission (see Chapter 3 for details).

Fig. 2.1 represents some typical  $e^\pm$  trajectories for different incidence angles with respect to crystal planes:

- **1**: high above-barrier motion with  $\theta_0 \gg \theta_c$ , which implies the possible to use the rectilinear trajectory approximation and so the CB theory;
- **2**: low above-barrier motion with  $\theta_0 \sim \theta_c$  and transverse energy,  $E_T$ , larger than  $U_0$ .
- **3**: channeling motion with with  $\theta_0 \sim \theta_c$  and  $E_T < U_0$

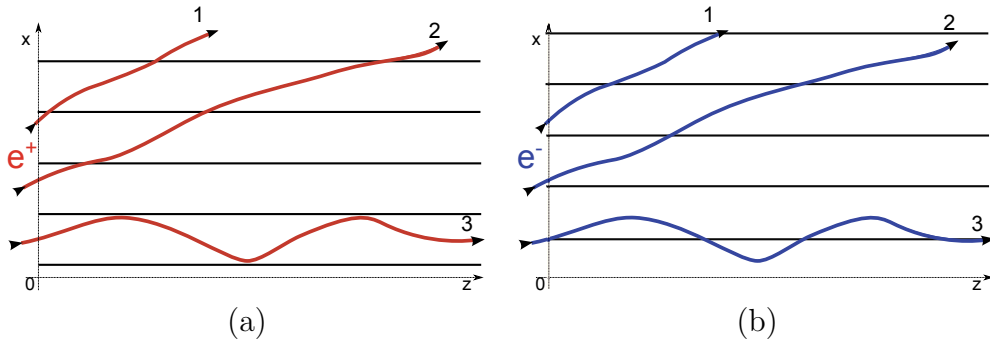


Figure 2.1: Typical positrons (a) and electrons (b) trajectories for different incident angles with respect to the planes: **1**  $\theta_0 \gg \theta_c$ ; **2**  $\theta_0 \sim \theta_c$  and  $E_T > U_0$ ; **3**  $\theta_0 \sim \theta_c$  and  $E_T < U_0$ .

## Coherent Bremsstrahlung

In this section, a brief introduction of the concept of coherent bremsstrahlung is given following the work of Ter-Mikaelian<sup>4</sup>. Bremsstrahlung is the process of electromagnetic radiation production by the deceleration of a charged particle when deflected by another charged particle, typically an electron by an atomic nucleus. In the process of bremsstrahlung, a photon with energy  $\omega = \varepsilon - \varepsilon'$ ,  $\varepsilon$  and  $\varepsilon'$  being the initial and final energies of the particle, is emitted in a direction  $\mathbf{n}$ , while a momentum  $\mathbf{q} = \mathbf{p} - \mathbf{p}' - \frac{\omega}{c}\mathbf{n}$ ,  $\mathbf{p}$  and  $\mathbf{p}'$  being the initial and final particle momenta, is transferred to the medium. The minimal value of transferred momentum along the direction of motion of the primary particle,  $q_{\parallel}$ , is equal to  $\delta$ , which is defined as

$$\delta = \frac{\omega m c^2}{2\varepsilon\varepsilon'} m c. \quad (2.5)$$

It is clear from eq. 2.5 that the value  $1/\delta$  has a length dimension and determines the distance which characterizes the order of dimensions of the region where bremsstrahlung

<sup>4</sup>In this section we use the units:  $\hbar = 1$

takes place:

$$l_c = \frac{1}{\delta} = \frac{2\varepsilon\varepsilon'}{\omega mc^2} \frac{1}{mc}, \quad (2.6)$$

where  $m$  is the mass of the particle.

For soft photon emission ( $\omega \ll \varepsilon$ ) at ultrarelativistic energies, eq. 2.6 becomes

$$l_c = \frac{2\varepsilon^2}{\omega mc^2} \frac{1}{mc} \simeq \frac{c}{\omega(1 - v/c)}, \quad (2.7)$$

$l_c$  is called coherence length and it was introduced for the first time by Ter-Mikaelian. The coherence length increases with the primary particle energy and with the decreasing of the energy of the emitted photon. At high energy,  $l_c$  may become large enough to introduce the idea that the emission of a photon is not a sudden process, while instead is formed in certain distance along the electron trajectory.

A classical interpretation of the coherence length can be given considering a particle which moves with a velocity  $v$  along a rectilinear trajectory and emits e.m. waves with a certain frequency during its motion [63]. The coherence length represents that distance along which all the e.m. waves are emitted in phase ( $\Delta\phi \leq 1$ ):

$$\Delta\phi = \omega l_c/v - k l_c = 1, \quad (2.8)$$

where  $\omega$  and  $k$  are the frequency and the wave vector of the emitted wave. From eq. 2.8, we found for ultrarelativistic energies:

$$l_c = 2c\gamma^2/\omega, \quad (2.9)$$

which coincides with eq. 2.7 introduced before and defines the order of magnitude of the space region along the particle momentum within which interference effects manifest themselves. If the trajectory is not rectilinear, the region in which the interference effects manifests may decrease with respect to  $l_c$ . This may occur for example due to multiple scattering inside a medium, leading to suppressions effects in the emitted bremsstrahlung radiation [64].

If the material under exam is crystalline, at enough high-energy,  $l_c$  may become of the order of the lattice constant  $d$ . For instance, for GeV electrons and MeV emitted photons,  $l_c \sim \mu\text{m}$ . As a consequence, the effect of the periodic structure in bremsstrahlung radiation should be taken into account, i.e., coherent bremsstrahlung (CB) occurs. More precisely, CB occurs when a charged particle crosses a crystal at an angle  $\theta_0 \gg \theta_c$  to fulfilled the

condition of nearly rectilinear trajectory and the condition of applicability of the first Born approximation, while being small enough for the continuum approximation to be valid.

Interference effects in the bremsstrahlung of electrons/positrons crossing the periodic structure of a crystal appeared for the first time during the 1950s in the works of Ferretti [8], Ter-Mikaelian [9], Dyson and Uberall [10]. Such effect took the name *coherent bremsstrahlung* (CB), to be distinguished from the ordinary bremsstrahlung in an amorphous medium described by Bethe and Heitler (BH)<sup>5</sup>. CB was experimentally proven true by Diambrini-Palazzi et al. at Frascati in 1960.

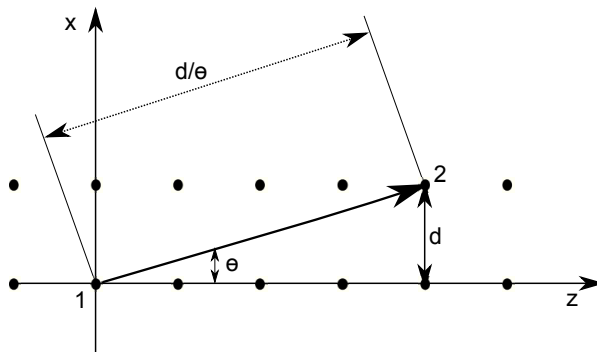


Figure 2.2: Illustration of the classical interpretation of interference processes in crystal [9].

Interference phenomena in bremsstrahlung radiation can be interpreted from the classical point of view (in this case  $\omega \ll \varepsilon$  is always valid). Let us consider a crystal with lattice constant  $d$ . If an  $e^\pm$  impinges onto a crystal with velocity  $v$  and with a small angle  $\theta$  with respect to an axis (or a plane) (see Fig. 2.2), we can deduce the condition of

<sup>5</sup>The quantum theory of bremsstrahlung has been developed by Bethe and Heitler [6]. The bremsstrahlung differential cross section in matter can be approximated in the complete screening case as:

$$\frac{d\sigma_{BH}}{d\omega} = \frac{16}{3} Z^2 \alpha r_e^2 \frac{1}{\omega} \left[ 1 - y + \frac{3}{4} y^2 \ln(183 Z^{-1/3}) + \frac{1}{12} \right], \quad (2.10)$$

where  $y = \omega/\varepsilon$  is the fraction of the electron energy transferred to the radiated photon,  $r_e = e^2/mc^2$  and  $Z$  are the classical electron radius and the atomic number, respectively. For rough estimation, eq. 2.10 can be rewritten in a simpler way as [48]:

$$\frac{d\sigma_{BH}}{d\omega} \approx \frac{A}{X_0 N_A \omega} \left( \frac{4}{3} - \frac{4}{3} y + y^2 \right), \quad (2.11)$$

where  $A$  and  $N_A$  are the mass and the Avogadro numbers, respectively, and  $X_0$  is the radiation length.  $X_0$  is an intrinsic characteristic of a material, representing the mean distance over which a high-energy electron loses all but  $1/e$  of its energy by bremsstrahlung.

*constructive interference* between the bremsstrahlung radiation emitted at point 1 and at point 2, respectively; here it has been assumed that radiation is emitted when the particle passes close to the atoms at point 1 and 2. If  $\theta$  is small, the radiation is emitted at point 1 at the instant  $t_0$ , while at point 2 at  $t_0 + d/\theta v$ ,  $v$  being the particle velocity. Since the first e.m. wave reaches the point 2 at the time instant  $t_0 + d/\theta c$ , the constructive interference condition is:

$$\frac{\omega d}{\theta} \left( \frac{1}{v} - \frac{1}{c} \right) = 2\pi n. \quad (2.12)$$

The condition 2.12 can be rewritten as:

$$\frac{\delta}{\theta} = n \frac{2\pi}{d} \quad (2.13)$$

where  $\delta$ , as before, denotes a minimal parallel momentum transferred,  $q_{\parallel}$ . In the second term of eq. 2.13 appears a factor  $\frac{2\pi}{d}$  that has the dimensions of a reciprocal lattice vector. This means that the bremsstrahlung radiation emitted in a crystal increases when the momentum transferred from the particle to the atoms matches a reciprocal lattice vector. In simple words, the reason of the different radiation spectra between the cases of incoherent and coherent bremsstrahlung can be ascribed to the fact that the first is a sum over a continuum of momentum-transfer vector, while the second is a discrete sum.

The electron/positron radiation differential cross section for CB can be represented as a sum of coherent and incoherent radiation [9, 63]:

$$d\sigma = d\sigma_{inc} + d\sigma_{coh}, \quad (2.14)$$

where  $d\sigma_{inc}$  the incoherent cross section

$$d\sigma_{inc} = Nd\sigma_{BH} + d\sigma_1, \quad (2.15)$$

$N$  being the number of independent atoms, and  $d\sigma_{coh}$  is the coherence (interference) cross section

$$d\sigma_{coh} = \frac{2e^2\delta}{m^2\Delta} \frac{d\omega}{\omega} \frac{\varepsilon'}{\varepsilon} \sum_{\mathbf{q}} |G(\mathbf{q})|^2 \frac{\mathbf{q}_{\perp}^2}{q_{\parallel}^2} \left[ 1 + \frac{\omega^2}{2\varepsilon\varepsilon'} - 2\frac{\delta}{q_{\parallel}} \left( 1 - \frac{\delta}{q_{\parallel}} \right) \right] e^{-\mathbf{q}^2 u_T^2} \times \theta_{hs} (|q_{\parallel}| - \delta) \quad (2.16)$$

where  $\Delta$  is the volume of the unit cell,  $u_T$  the RMS of thermal vibrations and  $G(\mathbf{q})$  is the

Fourier component of the crystal potential defined as [4]:

$$U(\mathbf{r}) \equiv \sum_{\mathbf{q}} G(\mathbf{q}) e^{-i\mathbf{q}\mathbf{r}} \quad (2.17)$$

where the sum is over the reciprocal lattice vectors  $\mathbf{q} = 2\pi(n_1, n_2, n_3)/d$ ,  $d$  being the lattice constant.  $q_{\parallel} = \mathbf{q}\mathbf{v}_0$  and  $\mathbf{q}_{\perp} = \mathbf{q} - \mathbf{v}_0(\mathbf{q}\mathbf{v}_0)$  are the parallel and the transverse transferred momenta, respectively, while  $\mathbf{v}_0$  is the initial velocity of the relativistic particle. The Heaviside step function  $\theta_{hs}(|q_{\parallel}| - \delta)$  denotes the edge of the peak and the region of  $|q_{\parallel}| \geq \delta$ . As a consequence, peaks of constructive interference appear in the radiation spectrum when this condition is fulfilled.

By returning to eq. 2.15, we may notice that, besides the BH cross section  $d\sigma_{BH}$ , there is a second term,  $d\sigma_1$ , which is not present in the case of amorphous material [9].  $d\sigma_1$  has the following form:

$$d\sigma_1 = -Nd\sigma_{BH} e^{-\mathbf{q}^2 u_T^2}, \quad (2.18)$$

which is independent of crystalline structure. The case of a perfect crystal (thermal vibrations  $u_T = 0$ ) leads to the disappearance of the incoherent cross section term  $d\sigma_{inc}$ . In realistic situations, the thermal vibrations modify the coherent cross section  $d\sigma_{coh}$  of eq. 2.16 and also the contribution of incoherent bremsstrahlung, which results to be decreased with respect to the Bethe-Heitler value of about 5-25 % [9].

In Fig. 2.3 is shown the intensity of CB radiation of 1 GeV electrons passing in a diamond crystal near plane (001) at angle of 4.6 mrad relative to the  $\langle 110 \rangle$  axis for the Frascati results[26], where sharp peaks can be noticed. At large photon energies,  $x = \omega/\varepsilon > 0.6$ .

## Channeling Radiation

The channeling of electrons and positrons may be accompanied by an intense radiation (CR). The features of this kind of radiation have been predicted by Kumakhov [11] in the mid-70s.

In the case of planar channeling, CR is generated by the nearly oscillatory motion of particles inside the channel caused by the interaction of an electron/positron with the strong planar field ( $\sim 10^{10}$  V/cm). The emission of radiation is caused by transitions from a bound-state in the transverse potential to another one. Even if the energy scale of the potential is in eV, the CR can be in the MeV-GeV range due to Lorentz-boosts [65] (see eqs. 2.1). We have seen before that the radiation regime of CR depends strongly on the particle energy,  $\varepsilon$ . At lower energy CR is dipole-like, becoming synchrotron-like at higher

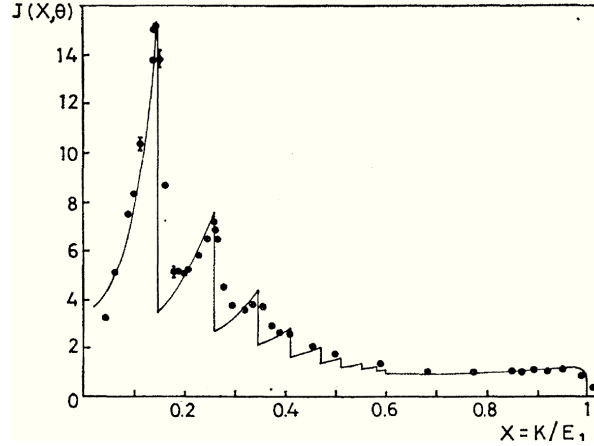


Figure 2.3: Bremsstrahlung intensity for 1 GeV electrons passing in a diamond crystal near plane (001) at angle of 4.6 mrad relative to the  $\langle 110 \rangle$  axis for the Frascati results[26].

energies. In practice, we can describe the planar CR with the eqs. 2.2 and 2.3 seen before for the simple case of periodical (or quasi-periodical) motions.

For instance, if we consider the motion of channeled positrons in the harmonic interplanar potential  $U = U_0(2x/d_p)^2$ , the frequency of motion results to be:

$$\omega_0 = \frac{2}{d_p} \sqrt{\frac{2U_0}{m\gamma}}, \quad (2.19)$$

$m$  being the positron mass. In the dipole limit, the emitted radiation frequency is shifted by the Doppler effect :

$$\omega = \frac{\omega_0}{1 - v/c \cos \theta}. \quad (2.20)$$

In the ultrarelativistic limit ( $\gamma \gg 1$ ), the radiation frequency emitted in the forward direction ( $\theta = 0$ ) becomes (see eq. 2.2):

$$\omega \approx 2\gamma^2 \omega_0 = \frac{4}{d_p} \sqrt{\frac{2U_0}{m}} \gamma^{3/2}. \quad (2.21)$$

Even if the motion of a channeled electron/positron resembles the one in a magnetic undulator, to calculate the emitted radiation one has to average on the contribution of all possible trajectories. The form of each trajectory is dependent on the transverse impact parameter with respect to the planar potential for a given angle of incidence  $\theta_0$ . Moreover, a significant difference between particles of opposite charges comes into play for CR. In the planar channeling mode, positrons move in an inter-planar potential well, while electrons

move around a plane. The particles that pass closer to planes feel a stronger electric field during their motion and so generate more intense radiation. Most of the intense radiation for planar channeled positrons is due to particles with high-amplitudes of oscillations, while for electrons is due to particles with small amplitude with respect to plane [42].

## 2.2 General features of emission of radiation by high-energy particles in bent crystals

In general, the curvature plays a role in particle's dynamics as well as in superposition of generated radiation. For instance, the motion of planar channeled particles in a bent crystal is composed of two different parts: the circular motion caused by the bending and the channeling motion itself. In the case of electrons or positrons, the first one may result in a synchrotron-like radiation, while the latter leads to the CR modified by the crystal curvature. If the curvature radius is large enough to have channeling, i.e., much larger than the critical radius (see Sec. 1.2.1), these two contributions can be well separated, because the synchrotron-like radiation contribution is usually much softer than the CR one [66, 67]. In [66], it was demonstrated that the CR emitted by 120 GeV/c positrons is nearly independent of the crystal curvature.

On the other hand, the electromagnetic radiation emitted by  $e^\pm$  in VR orientation is more complex, due to the changing of the angle between particle trajectory and crystal planes as the particle approaches to the reflection point. In the next section, a qualitative description of radiation accompanying single and multiple volume reflection is presented.

### 2.2.1 Radiation accompanying single and multiple volume reflection

The average incidence angle of over-barrier particles impinging onto bent crystal planes ( $\theta_0(t)$ ) changes during particle motion [20] (see Fig. 2.4). If the energy is high enough ( $> 10\text{GeV}$ ), this may result in a changing of the radiation regime from pure dipole far from the reflection point to synchrotron-like regime in the VR region [20, 68, 69]. Depending on the energy and crystal curvature, it may happen that far from the reflection point,  $\theta_0 \gg \theta_v$  (or  $\rho \ll 1$ ) and hence radiation is due to coherent bremsstrahlung, while approaching the reflection point, the parameter  $\rho$  increases and  $\theta_0 \sim \theta_v$ , causing the loss of validity of the rectilinear trajectory approximation and of dipole-radiation. During the transition from CB- to synchrotron-like radiation regime, the radiation intensity and multiplicity increase

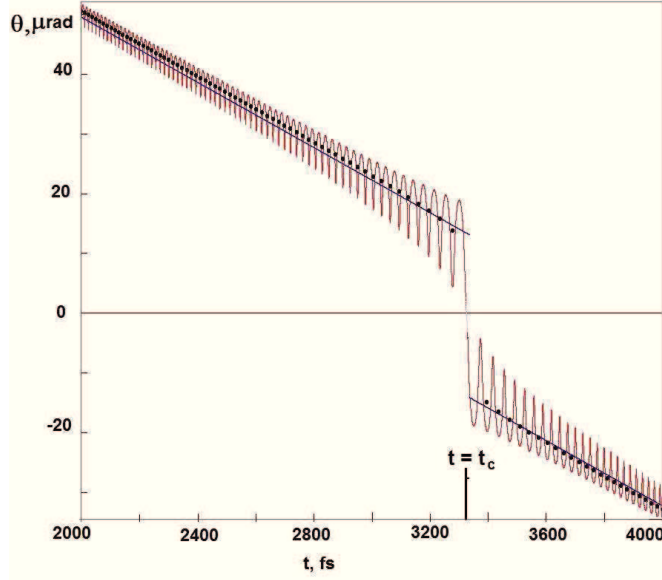


Figure 2.4: Example of possible time evolution of  $\theta_0(t)$  in the area near the reflection point: a 120 GeV/c positron performs an aperiodic oscillation in the transverse plane and the amplitude of the oscillations increases as the particle approaches the reflection point, becoming parallel to (110) crystallographic planes. Adapted from [66].

while radiated photon energy decreases.

Before the experiments described in this thesis in Chapters 4 and 5, some other experiments to investigate the radiation accompanying VR of electrons and positrons have already been done [20, 22, 66]. In these preliminary studies, it was proved the low dependence of VR radiation of charge's sign [20] and of bending radius [66]. Moreover, the wide angular acceptance of VR, which is equal to the bending angle of the crystal, is reflected in a similar radiation emitted by particles impinging onto the crystal with an angle within the whole angular acceptance [66]. In more details, the velocity evolution near the reflection point is similar for particles moving in the wide interval of the directions touching bent planes inside the crystal. As a result, the radiation accompanying VR is characterized by the low dependence on particle beam incidence direction and divergence. These features make this type of radiation suitable for the conversion of divergent electron and positron beams to  $\gamma$ -beam with no strict requirement on the crystal-to-beam orientation [A1] or for a crystal-based collimation in future electron/positron colliders [19]. A detail description of such opportunities is presented in Sec. 4.3.

Despite many advantages, VR radiation is limited by the relatively weak strength of the field of crystal planes, which may limit the possibility of high-intense  $\gamma$ -production through VR. A possibility to increase the intensity of radiation, while maintaining the

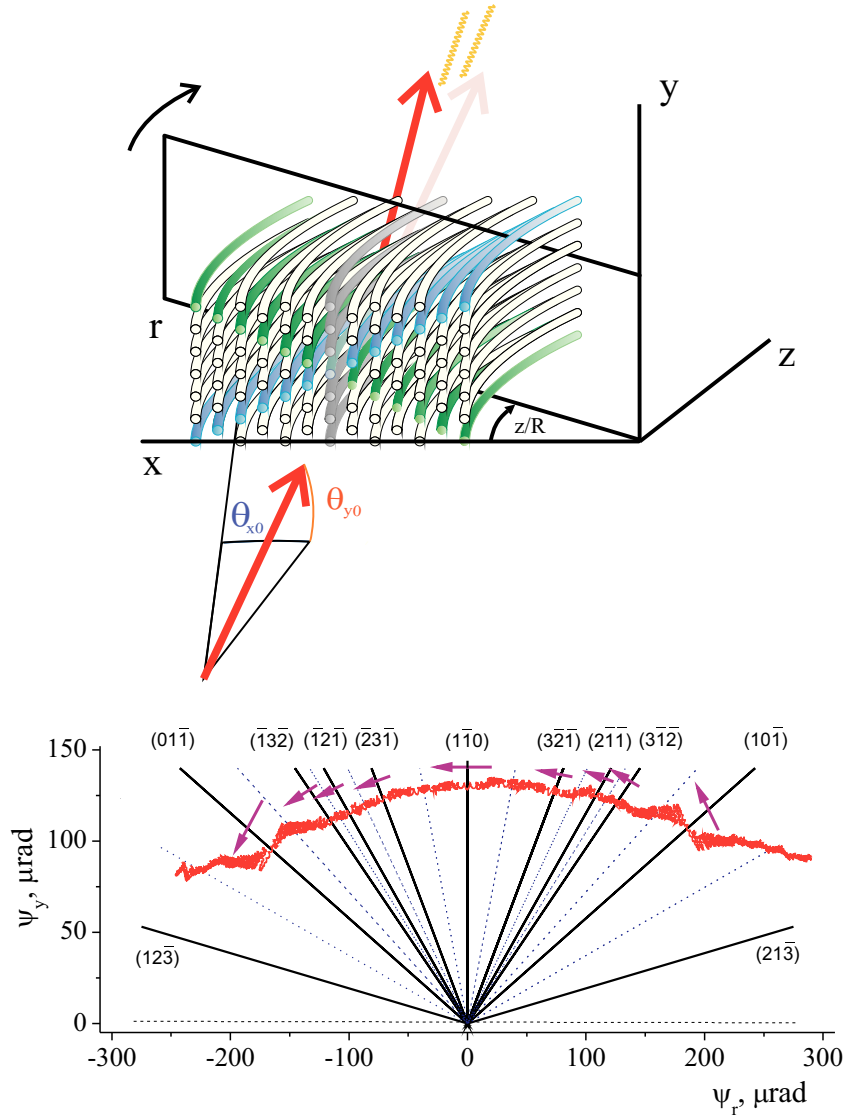


Figure 2.5: 120 GeV/c positron hitting the crystal at small angles with respect to  $\langle 111 \rangle$  axis, experiences VR from both the vertical,  $(\bar{1}\bar{1}0)_v$ , and numerous skew planes. (a) The comoving reference system  $ryz$  rotates with the bent axis direction  $z$  when a particle is moving through the crystal. (b) Evolution of particle transverse velocity in the  $ry$  plane. Figure also contains the projections of the crystal planes intersecting along the  $\langle 111 \rangle$  axis (solid) and the borders of the regions of influence by each plane (dashed). Small multiple arrows indicate the directions of particle reflection from different planes. The vertical projections of the angles of reflection from symmetric skew planes compensate each other while the horizontal ones sum up leading to the MVROC effect. Adapted from [A1].

good features of radiation accompanying VR, is given by the MVROC effect.

In the case of MVROC, many VRs occur when a particle crosses the crystal, thus changing the  $e^\pm$  dynamics and hence the process of photon emission as compared to the case of a single VR. As an example, Fig. 2.5 displays the evolution of a 120 GeV/c multiple volume-reflected positron transverse velocity in the  $ry$  plane (for comoving coordinates system see Sec. 1.2.3). Figure also contains the projections of the crystal planes intersecting along the  $\langle 111 \rangle$  axis (solid) and the borders of the region of influence by each plane (dashed). The typical evolution of the transverse velocity component of a positron in the comoving reference frame (see Fig. 2.5) highlights two strong reflections by the low-index skew planes  $(10\bar{1})$  and  $(01\bar{1})$  and weaker reflections by the others planes. In close vicinity of the reflection points, the particle experiences most pronounced oscillations in the field of the reflecting set of planes, resulting in a planar contribution to the radiation [70]. We can also notice that the plane influence angular region is shorter than in the case of single VR (for which it is about half of the bending angle), thus practically eliminating the possibility to have CB-like radiation. In the case of Fig. 2.5, if only the single VR with the vertical  $(1\bar{1}0)_v$  plane is considered, a positrons would cross the crystal passing from an incidence angle with the plane of about  $300 \mu\text{rad}$  (the angle with planes is  $\psi_r$ ) to 0 in the reflection zone, up to  $-250 \mu\text{rad}$  at the exit from the crystal. Since  $\theta_v = 40 \mu\text{rad}$  in the field of the  $(1\bar{1}0)_v$  planes, this means that the regime of radiation passes from CB-like to synchrotron-like to return back to CB-like. This does not happen for the case of MVROC, because the particle passes from the influence of one type of planes to another type, remaining not more than  $50 \mu\text{rad}$  in the region of the strongest  $(110)$  planes. Therefore, as a result of multiple reflections, the role of synchrotron-like radiation increases in the case of MVROC at high energies.

Since MVROC occurs at relatively small angles of the particle motion with respect to a crystal axis, electrons experience the so-called scattering by *strings of strings* (SOS) [1], rather than scattering by the smooth crystal planes. By combining the wealth of planar reflections occurring for MVROC with the contribution of atomic strings, the expected spectral intensity should be very strong as compared to that of an individual VR. Furthermore, since the axial electric field is six times stronger than for the planes, SOS contribution should considerably increase the probability of hard-photon emission [71].

Since the ideal condition for MVROC (eq. 1.35) does require that the incidence angle of particles with respect to a major crystal axis should exceed the angle of axial channeling by three-four times at least, the contribution of the planes to the radiation cannot be neglected, as it is instead for perfect alignment with axes.

Summarizing, the radiation accompanying MVROC is expected to be more intense than

the one for single VR due to the multiple-reflection from vertical and skew planes in the relatively soft spectrum region and to the scattering by separate axes in the harder one. The first experimental results on the radiation accompanying MVROC are presented in Chapter 4, where they are compared with the results obtained for the single VR case.

The strong variation of radiation conditions during the motion of ultra-high energy electrons/positrons subject to single and multiple volume reflections rises up a new challenge for both theory and simulations. No simple theories, such as CB or CR, can be used and a more general approach has to be applied.



## Chapter 3

# A method for calculation of emitted radiation in straight and bent crystals based on the Baier Katkov quasiclassical formula

As seen in Chapter 2, no simple model, such as CB or CR, to calculate the electromagnetic radiation emitted by electrons and positrons in bent crystals exists. This fact can be extended to the case of straight crystals, because the particle interaction with continuous potential is spoiled by the incoherent interaction with electrons and nuclei [4, 63], which could be very important, especially for electron channeling.

A general way to deal with the radiation emitted by ultrarelativistic particles in crystals is based on the usage of the general quasiclassical operators method proposed by Baier and Katkov (BK) in 1967-1968 [4]. Because the BK formalism takes into account real trajectories, it can be readily applied to study radiation generation also in deformed crystals, e.g., bent and periodically bent crystals.

### 3.1 The Baier-Katkov quasiclassical formula

As introduced in Chapter 1, the motion of ultrarelativistic charged particles in crystals can be well described by classical mechanics due to the high number of quantum states in the transverse potential well. Nevertheless, for sufficiently high-energies, even if the particle motion can be considered classically, this is not true for the process of radiation emission. In fact, it may happen that the emitted photon energy,  $\hbar\omega$ , becomes of the order of particle

energy  $\varepsilon$ . In such a case, one should consider the quantum recoil in the process of photon emission.

The question is: when the quantum corrections in the process of radiation emission must be taken into account? The answer can be given in QED, by introducing the Schwinger critical fields

$$E_0 = m^2 c^3 / e \hbar \simeq 1.3 \times 10^{16} \text{V/cm}, H_0 \simeq 4.4 \times 10^9 \text{T}. \quad (3.1)$$

The continuous potential of a crystal is of the order of  $10^{10} - 10^{11}$  V/cm, which is much smaller than the critical field. Nevertheless, if the particle is ultrarelativistic with  $\gamma > 10^5$ , in the rest-frame the particle feels a Lorentz-boosted field comparable to the critical field,  $E_0$  [72]. In such a case, the classical description of the process of radiation emission is no more valid.

In 1967-1968, Baier and Katkov (BK) proposed the usage of a *quasiclassical operator method* to solve the QED problem of emission of radiation by a charged particles in an external fields [73, 74]. In the QED description of this kind of processes, two types of quantum effects, i.e., the quantization of particle motion and the quantum recoil of the primary particle in the  $\gamma$ -quantum emission, are taken into account. The BK method is based on the fact that for the case of ultrarelativistic particles the motion can be consider classically, while the quantum recoil may not be negligible.

With the usage of the BK quasiclassical method, a QED problem is then reduced to the problem of solving the classical equations of motion of a charged particle in an external field and then calculating some integrals along the classical trajectory. This method has the advantage to be applicable in the whole photon energy range, except for the extreme limit where  $\hbar\omega \cong \varepsilon$ . The radiated energy, written in BK quasiclassical formalism [4] (in  $c = \hbar = 1$  natural system of units) is:

$$\frac{dE}{d^3k} = \omega \frac{dN}{d\omega d\Omega} = \frac{\alpha}{4\pi^2} \int \int dt_1 dt_2 \bar{N}_{21} \exp [ik'(x_1 - x_2)], \quad (3.2)$$

where  $dN(\omega)$  is the photon emission probability,  $\Omega$  the solid angle of photon emission,  $\alpha = 1/137$  is the fine structure constant,  $k = (\omega, \mathbf{k})$  is the 4-momentum of the photon radiated with energy  $\omega$  and 3-momentum  $\mathbf{k}$ ,  $k' = \varepsilon k / \varepsilon'$ , where  $\varepsilon$  and  $\varepsilon' = \varepsilon - \omega$  are, respectively, the particle energy before and after the photon emission,  $x_{1,2} = (t_{1,2}, \mathbf{r}(t_{1,2}))$  and  $\mathbf{v}(t_{1,2})$  are the particle coordinate 4-vector and 3-velocity at instants of time  $t_1$  and  $t_2$ .

The integrals in eq.3.2 are taken along the whole particle trajectory and

$$N_{21} = \frac{1}{2} \sum_{\mathbf{e}, \zeta_i, \zeta_f} N_{21}(\mathbf{e}, \zeta_i, \zeta_f) = \left[ (\varepsilon^2 + \varepsilon'^2)(\mathbf{v}_1 - \mathbf{n})(\mathbf{v}_2 - \mathbf{n}) + \omega^2/\gamma^2 \right] / 2\varepsilon'^2, \quad (3.3)$$

is the radiation polarization matrix averaged over the initial particle polarization  $\zeta_i$  and summed over the final particle  $\zeta_f$  and photon  $\mathbf{e}$  ones, where  $\mathbf{n}$  is the photon direction.

The main difference with the general classical equation for radiation emission in an external field (see eq. 1.23 of [4]) is the substitution of  $\omega \rightarrow \omega' = \varepsilon\omega/(\varepsilon - \omega)$ . In the limit of  $\omega \ll \varepsilon$ , these two expressions coincide and the radiation can be treated in the classical framework.

## 3.2 Algorithm for the Direct Integration of BK formula

In this section, an algorithm for the numerical calculation of the radiation spectrum based on the direct integration of the BK formula (DIBK) is introduced. Such algorithm has been developed by V. Tikhomirov and briefly presented in [A1], where comparison with existing data is also shown.

Since the coherent effects in the process of radiation emission in crystals appear when the angle between particle trajectories and crystal planes or axes is small and at ultra-relativistic energies the radiation angle  $1/\gamma$  is much smaller than unity, we can simplify the BK formula for radiated energy (Eq. 3.2) by using the small-angle approximation. For that, let us introduce a unit vector  $\mathbf{e}_z$  oriented as the initial particle velocity (or at a small angle). Therefore, the particle velocity  $\mathbf{v}$  and gamma-quantum momentum  $\mathbf{k}$  can be represented in the form:

$$\begin{aligned} \mathbf{v}(t) &\simeq \mathbf{e}_\perp v_\perp(t) + \mathbf{e}_z [1 - 1/2\gamma^2 - v_\perp^2(t)/2], \\ \mathbf{k} = \mathbf{n}\omega &\simeq \mathbf{e}_\perp \omega \theta + \mathbf{e}_z \omega (1 - \theta^2/2), \end{aligned} \quad (3.4)$$

by neglecting higher order terms than the second one. The angle  $\theta \ll 1$  represents the radiation angle referred to the longitudinal  $z$ -axis. In the small angle approximation, eq. 3.2 becomes [70, 75]:

$$\frac{dE}{d^3k} \sim \frac{\alpha}{8\pi^2} \frac{\varepsilon^2 + \varepsilon'^2}{\varepsilon'^2} \omega^2 C, \quad (3.5)$$

where  $C$  is equal to

$$C = |\mathbf{I}_\perp|^2 + \gamma^{-2} \frac{\omega^2}{\varepsilon^2 + \varepsilon'^2} |J|^2. \quad (3.6)$$

Hence, the evaluation of the radiated energy 3.2 is reduced to the calculation of the integrals:

$$\left\{ \begin{array}{c} J \\ \mathbf{I}_\perp \end{array} \right\} = \int_{-\infty}^{\infty} \left\{ \begin{array}{c} 1 \\ (\mathbf{v}_\perp(t) - \boldsymbol{\theta}) \end{array} \right\} \exp[i\phi(t)] dt, \quad (3.7)$$

where

$$\phi(t) = k'x(t) = \omega'[t - \mathbf{n} \cdot \mathbf{r}(t)] \simeq \frac{\omega'}{2} \int^t [1/\gamma^2 + (\mathbf{v}_\perp(t) - \boldsymbol{\theta})^2], \quad (3.8)$$

and

$$\omega' = \omega\varepsilon/\varepsilon'. \quad (3.9)$$

The basis of the DIBK algorithm is to start from a classical trajectory. The electron/positron trajectory can be build with any of the Monte Carlo code available based on the integration of particle trajectories under the continuum potential approximation, thus solving the classical equation of motion through numerical integration. In [A1], the code used for integration of motion allows taking into account the contribution of multiple and single incoherent scatterings by both atomic nuclei and electrons [76].

The particle trajectory is then divided in  $N$  small steps. During the step, the particle trajectory is calculated through integration of equation of motion in the continuous potential. The step length is not set a priori, but it depends on the averaged field derivative [77]. In other words, the step-length decreases if the particle is close to axes/planes. At the end of each step the multiple and single scattering by nuclei and electrons is sampled and the transverse velocity of the particle for the  $i$ -step becomes

$$\mathbf{v}_{\perp,i} \rightarrow \mathbf{v}_{\perp,i} + \boldsymbol{\theta}_{s,i}, \quad (3.10)$$

$\boldsymbol{\theta}_{s,i}$  being the cumulative scattering angle. Then, a numerical integration of eq. 3.6 is performed. With the aim of improving the the precision of the time-integrals in eq. 3.2, an integration by parts has been made and after some mathematical simplifications we obtain:

$$J = \int_{t_{in}}^{t_{fin}} \exp [i\phi(t)] dt \quad (3.11)$$

$$= \sum_{i=1}^N \int_{t_{i-1}}^{t_i} \exp [i\phi(t)] dt \quad (3.12)$$

$$\approx \sum_{i=1}^N \left\{ \exp [i\phi(t_i)] \left[ \frac{1}{i\dot{\phi}} \Big|_{t_{i-1}}^{t_i} \right] + \frac{\ddot{\phi}}{i\dot{\phi}^3} \Big|_{\bar{t}_i} (\exp[-i\phi(t_i)] - \exp[-\phi(t_{i-1})]) \right\} \quad (3.13)$$

$$\approx i \sum_{i=1}^N \left\{ \exp [i\phi(t_i)] \left[ \frac{1}{\dot{\phi}_{t_i+0}} - \frac{1}{\dot{\phi}_{t_i-0}} \right] - \exp [i\phi(\bar{t}_i)] \left[ \frac{2\ddot{\phi}}{\dot{\phi}^3} \Big|_{\bar{t}_i} \sin ([\phi(t_i - 0) - \phi(t_{i-1} + 0)]/2) \right] \right\} \quad (3.14)$$

where  $N$  is the total number of steps,  $\bar{t}_i = (t_{i-1} + t_i)/2$ ,  $\dot{\phi}$  the first time derivative of the phase in eq. 3.8, defined as follows:

$$\dot{\phi}(t < t_i) = \frac{\omega'}{2} [1/\gamma^2 + (\mathbf{v}_\perp(t) - \boldsymbol{\theta})^2], \quad (3.15)$$

$$\dot{\phi}(t_i + 0) = \frac{\omega'}{2} [1/\gamma^2 + (\mathbf{v}_\perp(t) + \boldsymbol{\theta}_{s,i} - \boldsymbol{\theta})^2], \quad (3.16)$$

eqs. 3.15 and 3.16 being the phase variations before and after step-end scattering and  $\ddot{\phi}$  second time derivative of the phase in eq. 3.8

$$\ddot{\phi}(t) = \omega' (\mathbf{v}_\perp(t) - \boldsymbol{\theta}) \dot{\mathbf{v}}_\perp(t), \quad (3.17)$$

where  $\dot{\mathbf{v}}_\perp = -\frac{1}{\varepsilon} \frac{\partial U(\mathbf{r})}{\partial \mathbf{r}_\perp}$ ,  $U(\mathbf{r})$  being the continuous potential. The integral  $\mathbf{I}_\perp$  can be represented in an analogous way. Such representation of the BK formula improved the convergence of its integration over time as well as over the photon emission angle  $\theta$ . We omit here the contributions of the trajectory ends, thus neglecting the soft contribution of the transition radiation that weakly affects both CR and CB spectra.

The integration over  $\boldsymbol{\theta}$  leads to the radiation spectral intensity,  $\omega dN/d\omega$ , i.e. the physical value measurable experimentally.

In principle, the BK formula should be integrated along the whole particle trajectory. Nevertheless, at very-high energy it may happen that the total probability of radiation exceeds unity, which means that multiple photon emission may occur. With the aim of simulating multiple photon emission, the classical trajectory is divided into some

”intermediate-lengths”. By intermediate length we mean a length much larger than the coherence length and much shorter than the typical distance between two sequential photon emission points, in order to allow for multiple photon emission to be treated correctly. The intermediate lengths are chosen a way that the total probability of radiation on such trajectory part does not exceed 0.1.

From the spectral intensity, one calculates its maximum and total probabilities of radiation. This two values are then used to determine the energy of the emitted photon through the acceptance-rejection method. If a photon is emitted, its energy is then subtracted from the particle energy and simulation proceeds in the same way for a new ”intermediate length” starting from the emission point until the particle had left the crystal.

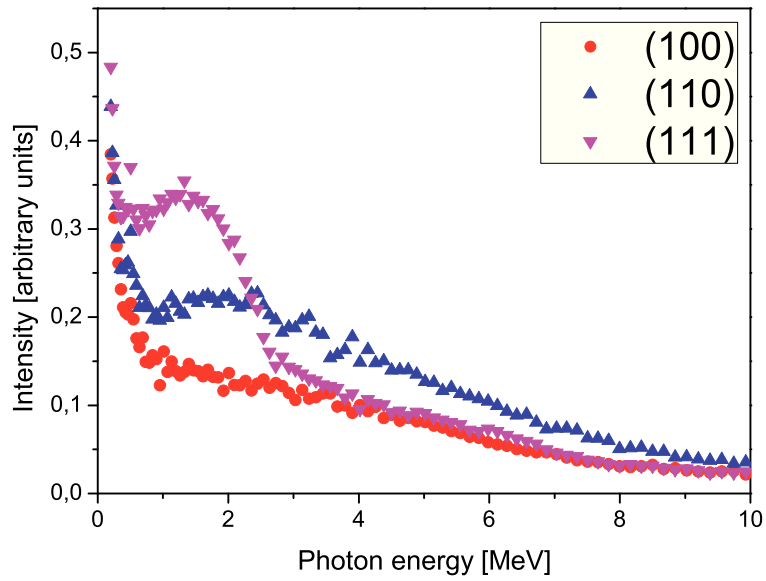
The presented approach to the integration of the BK formula, is similar to the one implemented by Artru [77], who was the first that treated both multiple coherent and incoherent radiation.

The developed code has been used by the author of this thesis to evaluate the radiative energy-losses by 120 GeV/c electrons in 2 mm Si bent crystal through VR in the field of (110) planes and through MVROC in the field of  $\langle 111 \rangle$  axes. The 2 mm crystal length has been divided in intermediate lengths for which the total probability of radiation on such trajectory parts did not exceed 0.1, while the number of such parts on one full trajectory was about a few dozens. Due to the finite resolution of the calorimeter used in the experiment, a cut-off at photon energy  $\geq 1$  GeV has been selected. Simulation results and comparison with experiments are presented in the Chapter 4.

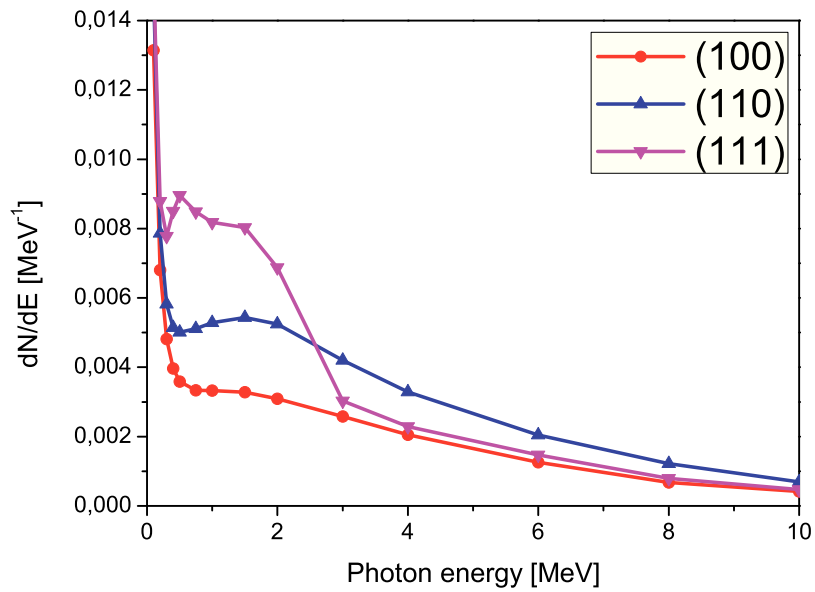
### 3.3 RADCHARM++

The DIBK algorithm for radiation computation has been used by the author of this thesis to develop a C++ routine for the computation of the processes of radiation in crystals and complex structure, named RADCHARM++ [A8]. An expansion of the Monte Carlo code DYNECHARM++ [78], which simulates the charged particle trajectories inside crystals and more complex structures, has been made in collaboration with E. Bagli through the implementation of the RADCHARM++ routine [A8].

The outcomes of DYNECHARM++ have already been successfully compared with the experiments with bent [79, 80] and periodically bent [81] crystals. The supplement of the DYNECHARM++ code with the RADCHARM++ routine extends it to the processes of e.m. radiation generation. The particle trajectory is simulated by the DYNECHARM++ code, which is capable of evaluating the electrical characteristics of complex atomic struc-



(a)



(b)

Figure 3.1: (a) Experimental spectra for electrons under planar channeling inside the (100), (110) and (111) planes of a 175 thick Si crystal. The spectra have been obtained through a deconvolution procedure performed by H. Backe starting from the row data collected by the NaI scintillator detector with a collimator aperture of about 1.31 mrad. (b) Simulated spectral distribution ( $dN/dE$ ) for the cases of Fig. 1(a). Adapted from [A8].

tures and to simulate and track the particle trajectory within them. The electrical characteristic of the crystal are evaluated through the ECHARM software [82, 83], which computes the atomic form factors by using x-ray diffraction data. The core of the code relies on the full integration of particle trajectories under the continuum potential approximation, thus solving the classical equation of motion through numerical integration via the Velocity-Verlet algorithm. At the end of each step the multiple and single scattering by nuclei and electrons is sampled [76].

In order to test the capability of the new version of the code, the outcomes of the simulations are critically compared with experiments performed at the MAInzer MIcrotron (MAMI) [84] with 855 MeV electrons.

Fig. 3.1(a) shows the experimental radiation spectra for planar channeling at the (100) (circles), (110) (up-triangles) and (111) (down- triangles) planes, in a 175  $\mu\text{m}$  thick Si straight crystal [53]. The experimental spectra have been obtained through a deconvolution procedure applied to the raw data collected by a NaI scintillator detector with a collimator half-aperture of about 1.3 mrad. Their reproduction here is a courtesy of prof. H. Backe.

Since in this case, the total emission probability is much smaller than unity, the code simply calculates the spectral distribution  $dN/dE$  (the same as  $dN/d\omega$ ),  $E$  being the photon energy, by integrating eqs. 3.7-3.14 along the classical particle trajectory as simulated by DYNECHARM++. Fig. 3.1(b) represents the simulated spectral distribution,  $dN/dE$ , for the experimental cases presented in Fig. 3.1(a). The difference in the y-scale between experimental and simulated spectra is due to the fact that in the first case the whole radiation collected by the NaI detector is shown, while the latter represents the photon emission spectral distribution. A direct comparison of the spectra in Fig. 3.1(a) and (b) highlights a good agreement in both shape and ratios between the three plots.

The RADCHARM++ routine can be easily updated by taking into account new physical effects, such as transition radiation, multi-photon emission etc.. For instance, the latter will improve not only the radiation emission evaluation, but also the simulation of particle trajectory made with DYNECHARM++ in the case of large radiative losses. On the other hand, any addition to the *physics list* of the DYNECHARM++ code, e.g. , the crystalline defects [85], results in an improvement of the RADCHARM++ computational precision. Because of the object-oriented programming mode, the RADCHARM++ routine itself can be easily updated and inserted into other Monte Carlo codes.

The DYNECHARM++ code with its extension RADCHARM++ has been used by the author of this thesis to compute the radiation emitted by sub-GeV electrons in a tens  $\mu\text{m}$  bent Si crystal. The results are shown in Sec 5.3.

## Chapter 4

# Radiation emitted by 120 GeV/c electrons through single and multiple volume reflection in a short bent crystal

The electromagnetic radiation emitted by 120 GeV/c electrons through single and multiple volume reflection in a bent silicon crystal have been investigated at CERN SPS-H4 beamline. The trajectories of electrons crossing a silicon strip-like crystal have been reconstructed through a telescope system composed by high precision microstrip detectors. A spectrometer and an electromagnetic calorimeter have been used to measure the energy loss by particles. The trigger strategy used during the experimental test allowed one to measure all the photon spectrum, up to the nominal energy of the beam, generated by volume-reflected particles for the first time with energies in the hundred-GeV range. Indeed, in previous experiments [20, 66], detection of the full photon spectrum was not possible due to a cutoff in the experimental setup which was limited to about half of the maximum allowed photon energy. Moreover, the results on radiation accompanying MVROC represent the first experimental evidence of this kind of radiation. The experimental results for either VR or MVROC have been compared with Monte Carlo simulations.

## 4.1 Experimental setup

Fig. 4.1 shows a scheme of the experimental setup set on the H4 beamline, which allowed measuring the energy lost by particles crossing a short bent crystal. It consisted of two part, one to measure the particle deflection after interaction with the crystal (part A) and a second dedicated to the measurement of the radiation spectrum (part B).

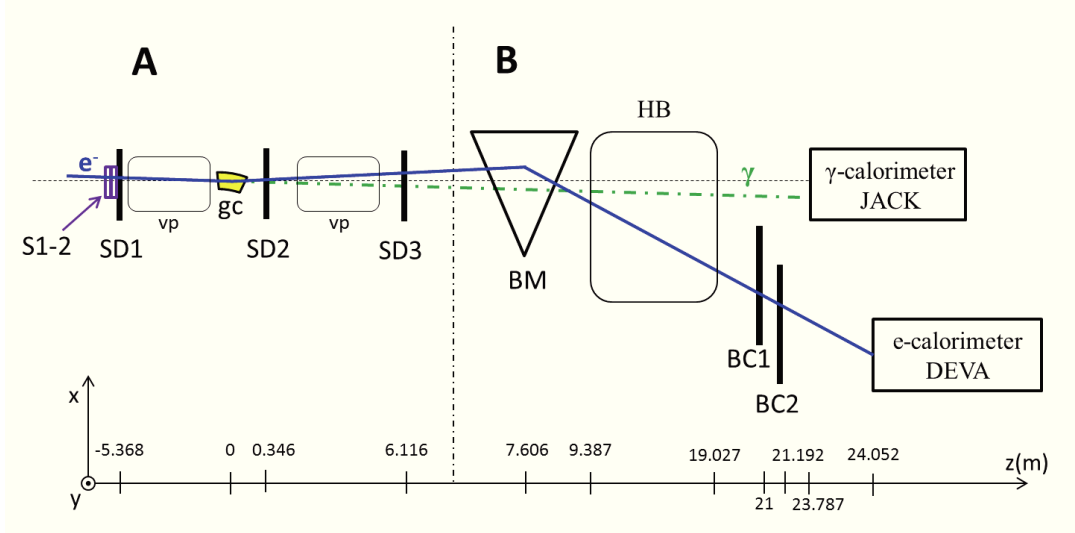


Figure 4.1: Scheme of the experimental setup on the H4 beamline at CERN SPS. The part A consists of a tracking (telescope) system composed by 3 silicon modules (SD<sub>i</sub>) separated by vacuum pipes (vp) and the high precision goniometer on which has been installed the StR3 crystal (gc). Two scintillator S1-2 are mounted on SD1 and are used for the trigger system. The part B consists of a spectrometer composed by a bending magnet (BM), a helium bag (HB), two large area silicon beam chambers (BC<sub>i</sub>) and two electromagnetic calorimeters DEVA and JACK, to measure the primary beam energy and the photon beam energy, respectively. Adapted from [A2].

### 4.1.1 Part A of the experimental setup: the tracking system

The study of coherent interactions of charged particles with bent crystals requires a high-precision in deflection measurements, i.e., a resolution lower than the critical angle  $\theta_c$ , which is of the order of  $20 \mu rad$  for planar channeling in Si at 100 GeV energies. A basic setup system that addresses these requirements is constituted by an high precision goniometric system to modify the relative orientation between the particle beam and the crystal and a full tracking system to measure both the incoming and outgoing particles angle [43].

A MICOS high-precision goniometer, composed by different stages (see Fig. 4.2), two linear and two rotational movements with the possibility to align the crystal in either horizontal (x) or vertical (y) directions, was used. All the stages are equipped with two-

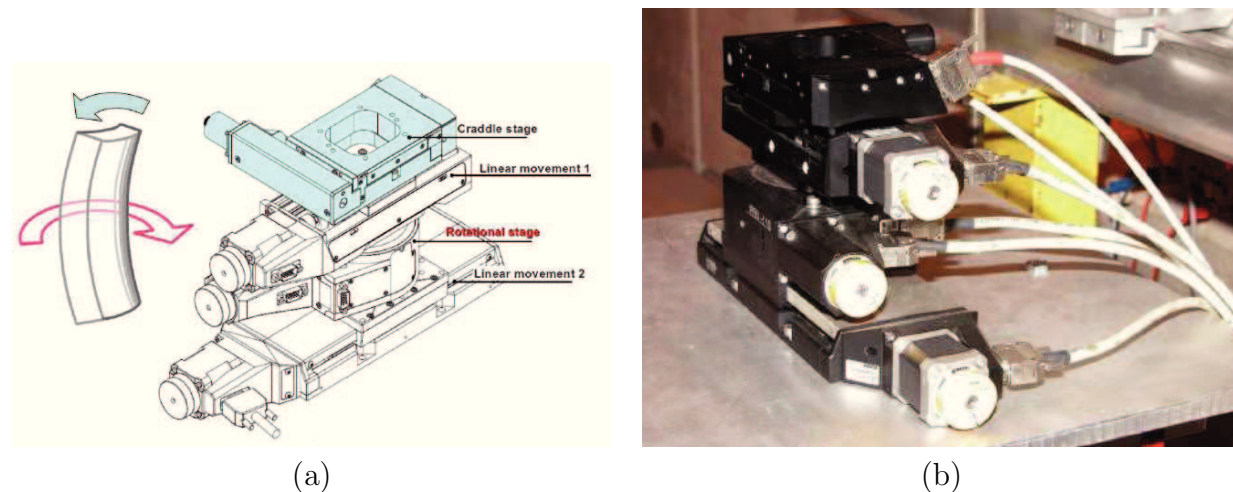


Figure 4.2: (a) A scheme of the goniometric system and of the rotational movements of a strip-like bent crystal. (b) A picture of the goniometric system [66].

phase microstep motors and mechanical limit switches are integrated in the two linear stages [86]. The linear stages and the two goniometers are equipped with a feedback mechanism, i.e., are read continuously by the electronic equipment and are constantly corrected to obtain the desired position through a feedback mechanism. The horizontal-rotational stage, which provides rotation around the Y-axis, has an angular range of  $360^\circ$ . The other rotational stage is more properly a cradle and varies the angle around the X axis with a limited angular range of about  $9 \text{ mrad}$ . Both the two goniometers have an accuracy of  $1 \mu\text{rad}$ . By means of the DAQ system, the motor positions are stored in the data files.

Deflection was measured by tracking the particle trajectory before and after the crystal through a telescope system of 3 double-sided silicon microstrip detectors (SDi in Fig. 4.1 part A) [87]. The SDi were developed by INFN of Trieste. Each of them consists in a box ( $12 \times 50 \text{ cm}^2$  and 4 cm thick) formed by a double sided silicon strip detector ( $1.92 \times 1.92 \text{ cm}^2$ ,  $300 \mu\text{m}$  thick) and its frontend electronics (see Fig.4.3). Each SDi is composed by two sides, p-side and n-side; the first one has a  $p^+$  implantation strip every  $25 \mu\text{m}$ , while the other one (perpendicular to the p-side) has a  $n^+$  implantation strip with a pitch of  $50 \mu\text{m}$ . The incoming and the outgoing angles of particles with respect to the crystal orientation have been determined by using information acquired from the detectors SD1-2 and SD2-3, respectively.

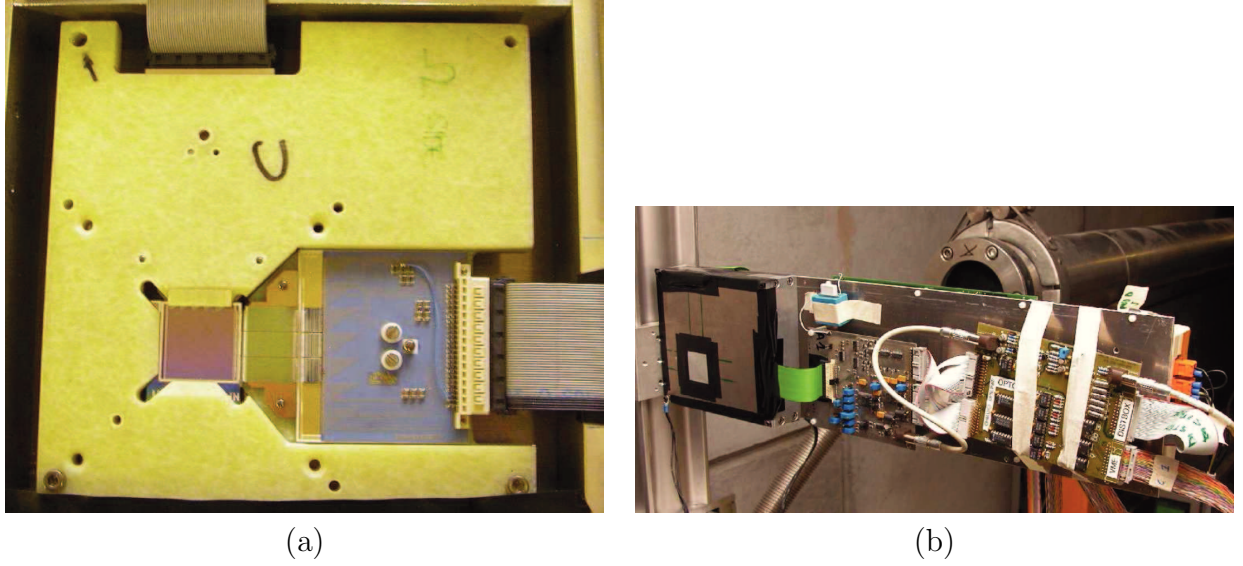


Figure 4.3: Two pictures of the double sided silicon detector: a) detail of detector [66]; b) the complete module.

The usage of double sided microstrip detectors has several advantages: good intrinsic spatial resolution both in the horizontal and in the vertical direction ( $\delta x \approx 6.4 \mu rad$  for p-side and  $\delta y \approx 10.5 \mu rad$  for n-side); a limited amount of material ( $\approx 300 \mu m$  each module) along the beamline to reduce the contribution of multiple scattering and background radiation, thus limiting the errors in the spatial and energy resolutions; simplicity and versatility in their installation due to their compactness [86]. The intrinsic resolution on the deflection angle could be computed by using the intrinsic resolution of one detector through the error propagation, resulting to be about  $4.8 \mu rad$  for the deflection angle in horizontal direction for the part A of the setup in Fig. 4.1. Since most of the phenomena usually investigated, such as planar channeling or volume reflection, generate deflection in one direction, for example the horizontal,  $x$ , direction in Fig 4.1, we had chosen the p-side, that provides a better angular resolution, to measure  $x$  position.

A Si strip-like crystal, labeled as StR3, of size  $70 \times 2 \times 0.3 \text{ mm}^3$  with the largest faces oriented parallel to (110) planes was mounted on the high-precision goniometer. A scheme of the crystal with its crystallographic orientations highlighted is depicted in Fig. 4.4(a). The crystal was fabricated through anisotropic chemical etching of 4-inch Si wafer at the Sensor and Semiconductor Laboratory of Ferrara University according to the procedure described in Refs. [88, 89]. An aluminum mechanical holder (see Fig. 4.4(b)) bents the crystal along its major direction, resulting in a primary curvature ( $R$ ). Anticlastic forces, caused by the necessity of the material to vary its structure to avoid breakage after the

main bending, generate a secondary curvature (anticlastic curvature,  $R_a$ ), which is used to deflect the beam particles [90]. The usage of the anticlastic curvature assures to maintain the interaction region between the beam and the crystal far from the mechanical parts, which may cause perturbations.

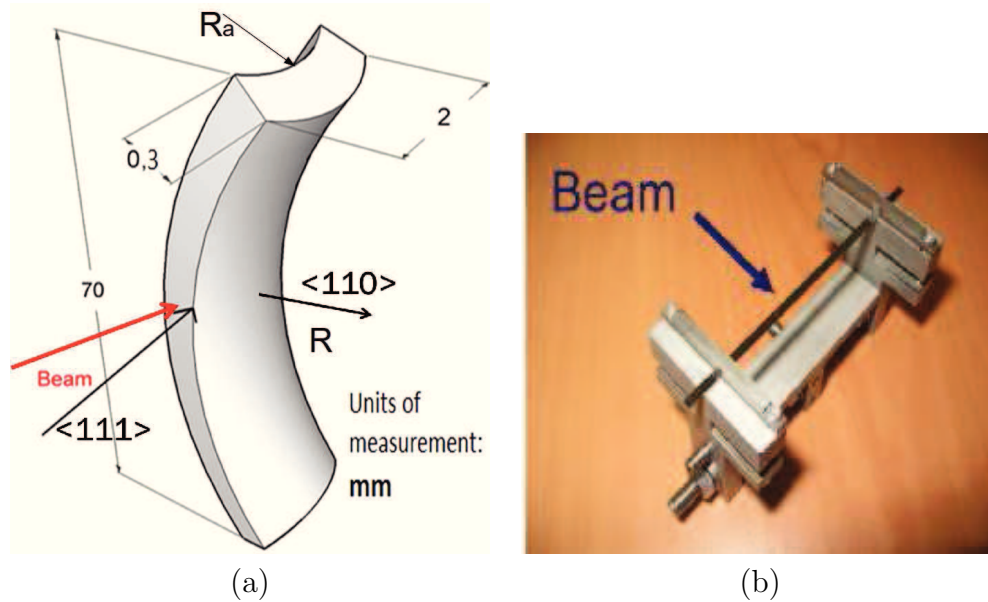


Figure 4.4: a) The primary ( $R$ ) and secondary anticlastic ( $R_a$ ) bending of the strip crystal and its crystallographic orientations. b) A scheme of the strip crystal bending device (the crystal holder). Adapted from [90].

#### 4.1.2 Part B of the experimental setup: the spectrometer and the electromagnetic calorimeter

The radiation spectrum was analyzed by the part B of the experimental setup presented in Fig. 4.1, consisting in a spectrometer to measure the energy lost by the particles and an electromagnetic calorimeter to achieve directly the emitted photons. The spectrometer was composed by a bending magnet (BM), to separate the electron and the neutral photon beams, and 2 large area silicon microstrip chambers (BCi), to measure the deflection angle of particles after the magnet (see Fig. 4.1 part B). Each of the two large area ( $9.5 \times 9.5 \text{ cm}^2$ ) silicon beam chambers [91] consists of two single sided  $410 \mu\text{m}$  thick silicon microstrip tiles, arranged in a x-y planes. The chambers BC1-2 were not aligned in horizontal position in order to increase the range of  $x$  deflection. In fact, a small portion of the chambers overlapped in horizontal position allowing to check the energy loss measured by both chambers and thus improving their alignment during off-line data analysis.

In the magnet length a charged particle is deflected along the  $x$  direction, due to the Lorentz force, by an angle calculated as follow:

$$\phi_b \approx \frac{eBL}{p} = \frac{0.3BL(Tm)}{p(GeV/c)}, \quad (4.1)$$

$\phi_b$  being the deflection angle (rad),  $p$  the particle momentum ( $GeV/c$ ),  $B$  the magnetic field (T) and  $L$  the magnet length (m). The H4 beamline setup provides a bending magnet with  $BL \sim 3.6$  Tm. By measuring the particle deflection after the magnet with the usage of BC1-2, it is possible to calculate the particle momentum and hence its energy loss as follow:

$$E_{loss} = E_0 - \sqrt{p^2c^2 + m^2c^4} \quad (4.2)$$

$E_{loss}$  and  $E_0$  being the energy loss and the initial energy of the particle ( $GeV$ ), respectively, while  $m$  being the particle mass ( $GeV/c^2$ ). For  $pc \approx 120$  GeV, the deflection angle of unperturbed particles was  $\phi_{b,0} = 9$  mrad, while for particles that had lost energy inside the crystal or along the beamline the deflection angle  $\phi_b$  was larger.

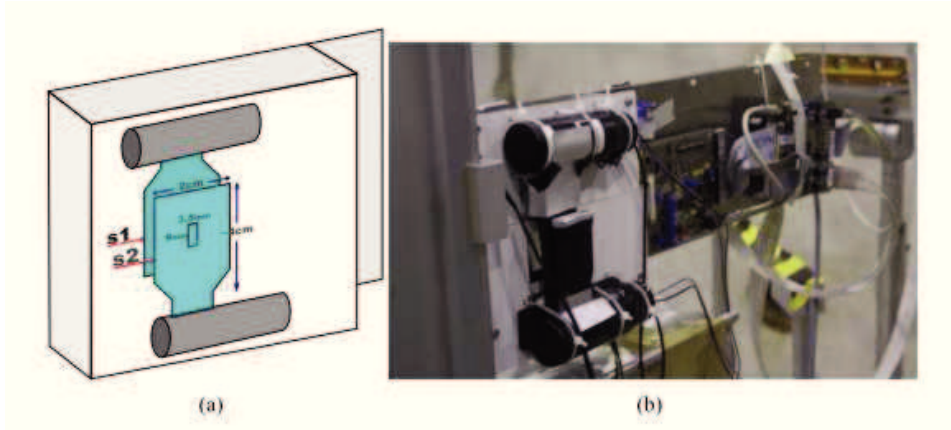


Figure 4.5: a) A picture of the trigger system: the scintillators S1-2 are mounted on the SD1 silicon detector. b) A photo of the S1-2 scintillators. Adapted from [86]

In order to reduce the multiple scattering contribution in the air, most of the space between the magnet and the chambers was covered by a helium bag. The electron beam of the H4 line is a tertiary beam and so it can contain also other kind of negative particles (mainly muons and light hadrons). To discriminate the electron part of the beam from these impurities, an electromagnetic lead-scintillator calorimeter (e-calorimeter DEVA in Fig. 4.6) was located after the chambers BCi.

The experimental setup was the one used in Ref. [21] with a few changes. The changes

consisted of a new trigger system, a different arrangement of detectors, beam-chambers and calorimeters and the introduction of a new calorimeter dedicated to the detection of electromagnetic radiation emitted by the particles. The new trigger system was composed by two plastic scintillators, one in front to the other, mounted on the first detector of the telescope system (see Fig. 4.5). Both scintillators were made of polystyrene with an area of  $2 \times 4 \text{ cm}^2$  and a thickness of 7 mm. One of the two scintillators had an hole of  $3.5 \times 9 \text{ mm}^2$  at the center of its area and it was used in anti-coincidence with the other scintillator to increase the acquisition of interesting events corresponding to particles impinging on the crystal [86]. Another advantage of the anti-coincidence trigger was to reduce the contribution of the background radiation (bremsstrahlung) due to a decrease in the amount of material crossed by the beam (one scintillator instead of two). The old trigger system was based on DEVA calorimeter; an high discrimination threshold of the calorimeter signal was used to increase the percentage of acquired electrons, exploiting the fact that muons and hadrons do not generate a shower in the calorimeter itself. The new trigger strategy was introduced in order to collect all the particles, with an energy loss value larger than what the spectrometer can measure. The energy losses for such particles were measured by the electromagnetic  $\gamma$ -calorimeter called JACK (see Fig. 4.6). In this way it was possible to acquire all particles that lost energy inside the crystal and hence determine the entire radiation spectrum. The last novelty of the new setup was the introduction of the new  $\gamma$ -calorimeter (JACK). It is a shashlik calorimeter composed by 70 tiles, 4 mm thick, of plastic scintillator and 69 tiles, 1.5 mm thick, of lead, for a total of 19 radiation lengths [92]. It was characterized by a larger active volume of plastic scintillator and it is readout using a larger area SiPM with 3600 pixels.

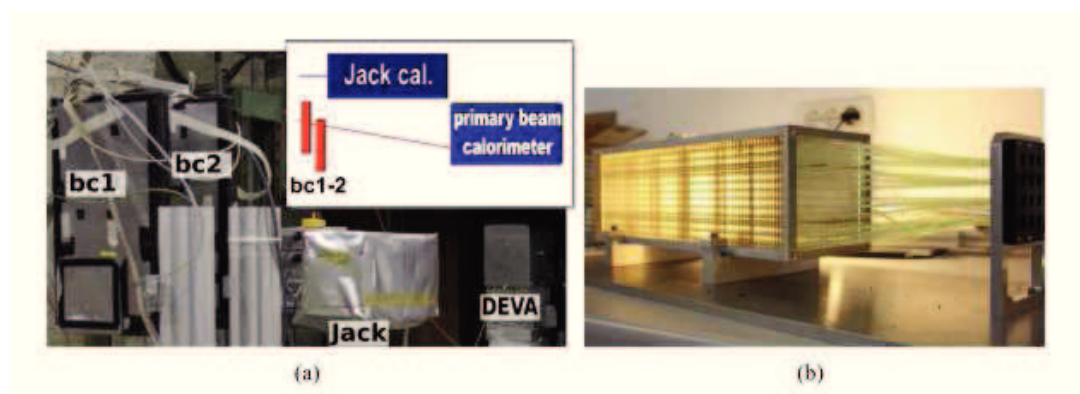


Figure 4.6: a) A photo of the calorimeters (DEVA e JACK) and a schematic view of their positions. b) A photo of JACK calorimeter: its front part contains the active region while fibers and SiMPs are interfaced in the black box. Adapted from [86].

A DAQ system developed by the INSULAB group (University of Insubria, It) collected all signals from various parts of the experimental system (e.g. silicon detectors, calorimeters..) and was based on the VME bus [86]. The analogical signals were discriminated by NIM modules and sent to the VME trigger board (INFN Trieste). The communication with a PC was provided by a SBS3 Bit3 board. The PC was also linked to the goniometer controller in order to change the crystal position and inclination. Finally the DAQ software generated output ASCII files in which all data were recorded.

## 4.2 Experimental measurements

### 4.2.1 Single Volume Reflection

In this section, the experimental results about radiation emitted by 120 GeV/c electrons volume-reflected onto (110) bent planes in the Si crystal StR3 are presented. In the first part of this section, we briefly describe the analysis method and the achieved results about the deflection of particles under VR conditions. The last part is dedicated to the analysis and the experimental results about radiation production.

#### Preliminary analysis

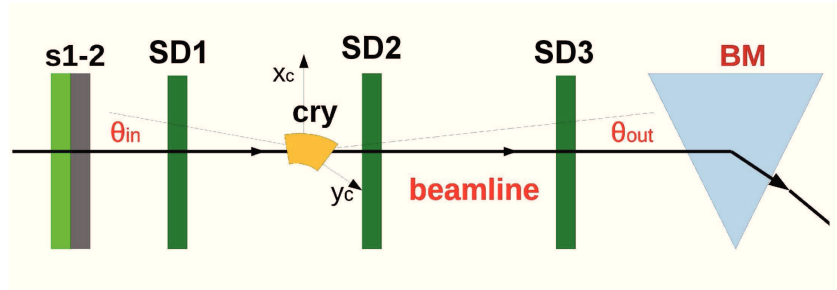


Figure 4.7: Part A of the experimental setup mounted on H4 beamline at CERN SPS: **the telescope system**. SD2-3 measure the  $\theta_{out}$  from the crystal. The position  $(x_c, y_c)$  on the crystal is estimated via projection and later use this information together with SD1 to evaluate the incoming angle  $\theta_{in}$ . The deflection angle is thereby obtained as  $\Delta\theta = \theta_{out} - \theta_{in}$ .

In order to improve the analysis we only examined the single tracks recorded in ASCII files by detectors SD<sub>i</sub>, thus avoiding the double and the missed tracks. Furthermore, some preliminary measurements were necessary to determine the bending angle of the StR3 crystal. This preliminary analysis was performed with the usage of a 120 GeV/c positron beam. The usage of a positron beam assured to avoid the spoiling effect of dechanneling

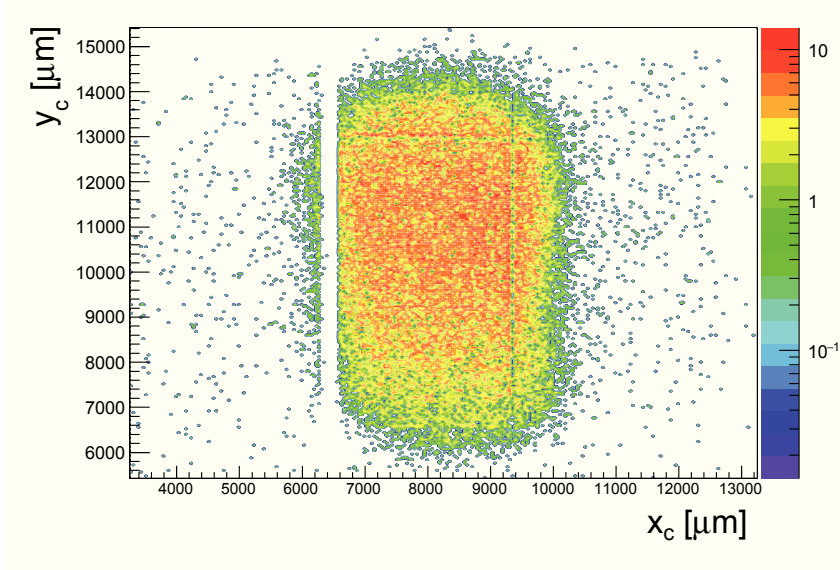


Figure 4.8: Space distribution of the beam in horizontal and vertical direction at the crystal position  $(x_c, y_c)$ . The empty strips in the 2D-distribution have to be ascribed to dead-strips in the strip detectors.

(see Sec. 1.1.2). The SPS H4 beamline assures the possibility to switch from a negative to a positive beam of the same energy simply by changing the current sign in magnetic dipoles of the beamline optics. The beam was about 88% of positrons and the other 12% was composed by positive particles, mainly protons, muons and light hadrons.

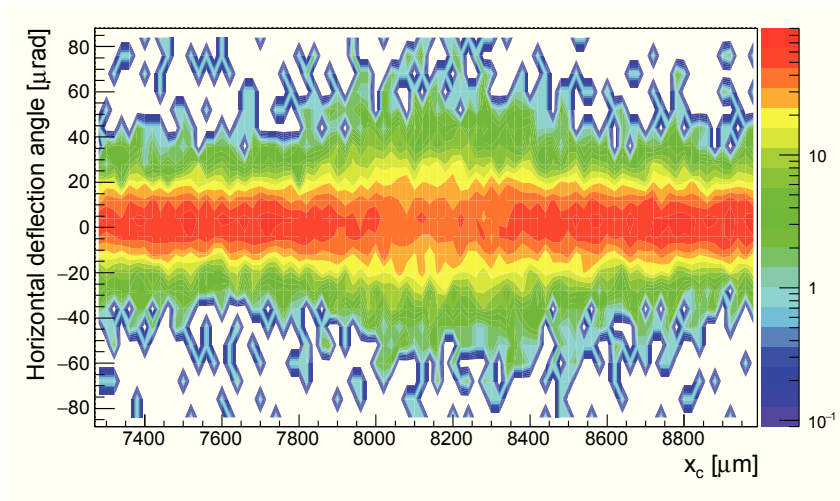


Figure 4.9: Horizontal deflection angle  $\Delta\theta_x$  vs. the horizontal position on the crystal  $x_c$ .

In the approximation of small angles, the horizontal incoming,  $\theta_{x,in}$ , and outgoing,

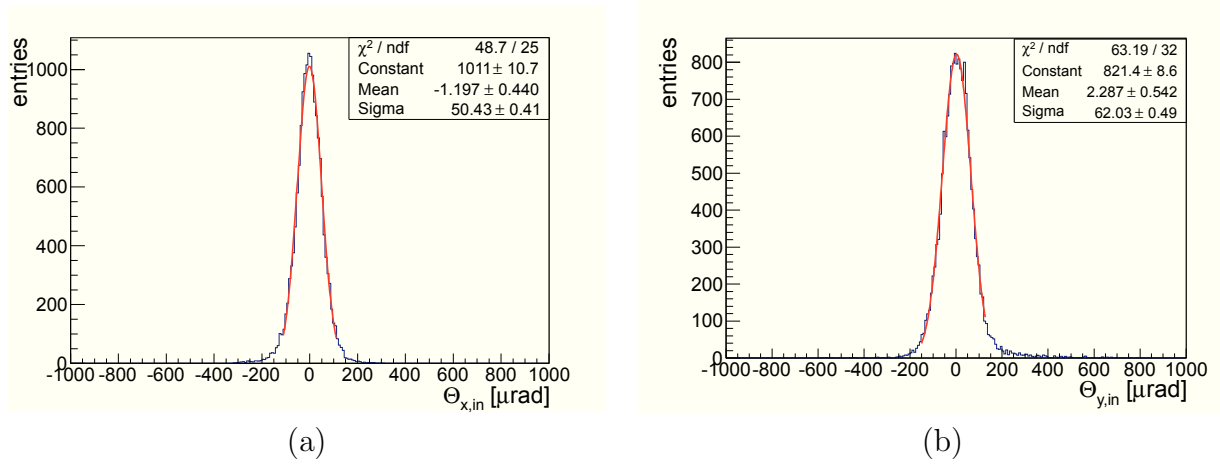


Figure 4.10: Incidence beam divergence in horizontal (a) and vertical (b) directions, respectively.

$\theta_{x,out}$ , angles of each particle with respect to the crystal and the corresponding deflection angle,  $\Delta\theta_x$ , were computed as following :

$$\theta_{x,out} = \frac{x_3 - x_2}{D_{2,3}} \quad (4.3)$$

$$x_c = x_2 - (\theta_{x,out} \cdot D_{c,2}) \quad (4.4)$$

$$\theta_{x,in} = \frac{x_c - x_1}{D_{1,c}} \quad (4.5)$$

$$\Delta\theta_x = \theta_{x,out} - \theta_{x,in} \quad (4.6)$$

being  $x_i$  the horizontal positions of each particle on the detectors SD1-3 and on the crystal;  $D_{i,j}$  are the distances between detectors (or crystal position) (see Fig. 4.7). The same procedure has been implemented to determine  $\Delta\theta_y$ .

With the aim of selecting only the particles that crossed the crystal, a geometrical cut has been implemented during data analysis. Since the beam dimension at the crystal position was  $4 \times 8 \text{ mm}^2$  wide (see Fig. 4.8), a range of  $300 \text{ μm}$  in the horizontal coordinate has been set for the off-line analysis. Fig. 4.9 displays the horizontal deflection angle  $\Delta\theta_x$  vs. of the horizontal position on the crystal  $x_c$ . The spreading of the deflection distribution in the central region (around  $x_c = 8150 \text{ μm}$ ) of the plot is caused by the increasing of the multiple scattering suffered by the particles due to the interception of the crystal. Moreover, to avoid any possible effects due to crystal deformation along the  $y$  direction, a range of  $\pm 500 \text{ μm}$  in the vertical coordinate with respect to the crystal center has been selected. The angular divergence of the selected portion of the positron beam

measured by the telescope is shown in Fig. 4.10 and resulted to be  $\sigma_x = (50 \pm 1) \mu\text{rad}$  and  $\sigma_y = (62 \pm 1) \mu\text{rad}$  in the horizontal and vertical direction, respectively.

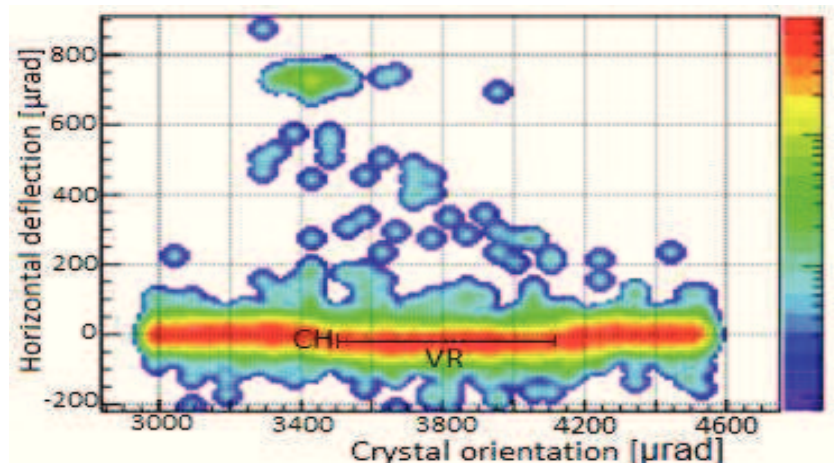


Figure 4.11: Horizontal deflection angle vs. the crystal-to-beam orientation. Channeling and VR angular regions are highlighted.

With the aim of finding the position for planar channeling, an horizontal angular scan was done by moving the rotational stage of the goniometer. Fig. 4.11 shows the horizontal deflection angle vs. the crystal-to-beam orientation. In spite of the low statistics, one can distinguish the channeling region, where a channeling peak is clearly visible, and the broad volume reflection region (about  $700 \mu\text{rad}$  wide in incidence angle), in which a small but intense particle deflection in the direction opposite to channeling is achieved. Then, the beam was aligned with the bent (110) planes and characterized in planar channeling condition. The resulting deflection distribution is displayed in Fig. 4.12. The highest peak on the left is formed by the overbarrier particles (included the volume-reflected particles), while the lowest peak on the right is due to the planar channeled particle. A Gaussian fit to the channeled peak yielded an average channeling deflection  $\phi = (735 \pm 19) \mu\text{rad}$ , resulting in a curvature radius  $R = L/\phi = (2.71 \pm 0.07) \text{ m}$ , where  $L = (2 \pm 0.01) \text{ mm}$  is the crystal length along the beam direction.

## Deflection measurements

After the determination of the correct curvature, the StR3 crystal was aligned with the 120 GeV/c electron beam for optimal bending through VR, corresponding to a horizontal average incidence angle with respect to the  $(110)_v$  vertical planes<sup>1</sup> of  $\theta_0 = 295 \mu\text{rad} \approx$

<sup>1</sup>The label *vertical planes* is referred to the planes normally used for beam steering through VR, to be differentiated by the *skew* planes of the same type.

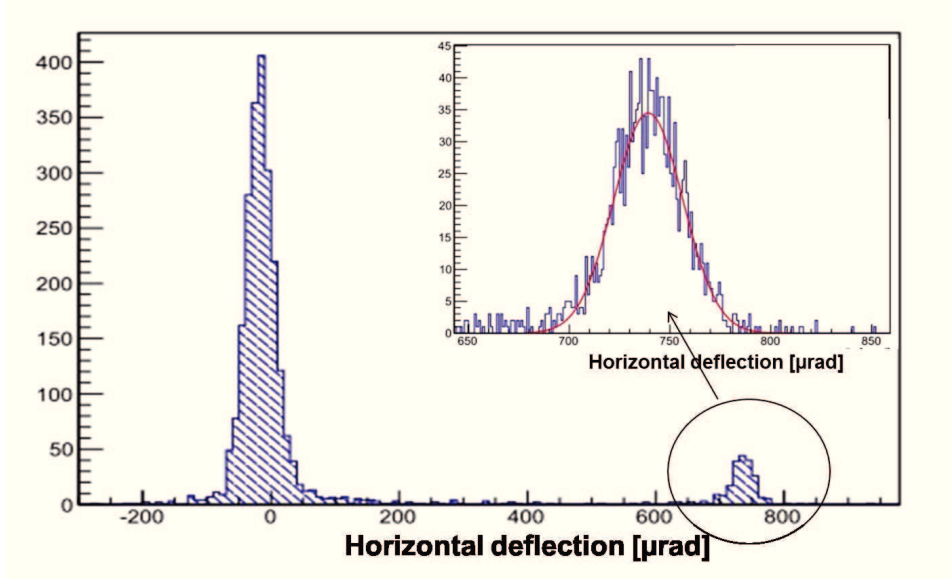


Figure 4.12: X-deflection distribution of the particles in planar channeling conditions in the field of vertical planes  $(1\bar{1}0)$ . The highest peak on the left is formed by the overbarrier particles, while the lowest peak on the right is due to the planar channeled particle. A Gaussian fit to the channeled peak yielded an average channeling deflection  $\phi = (735 \pm 19) \mu\text{rad}$ .

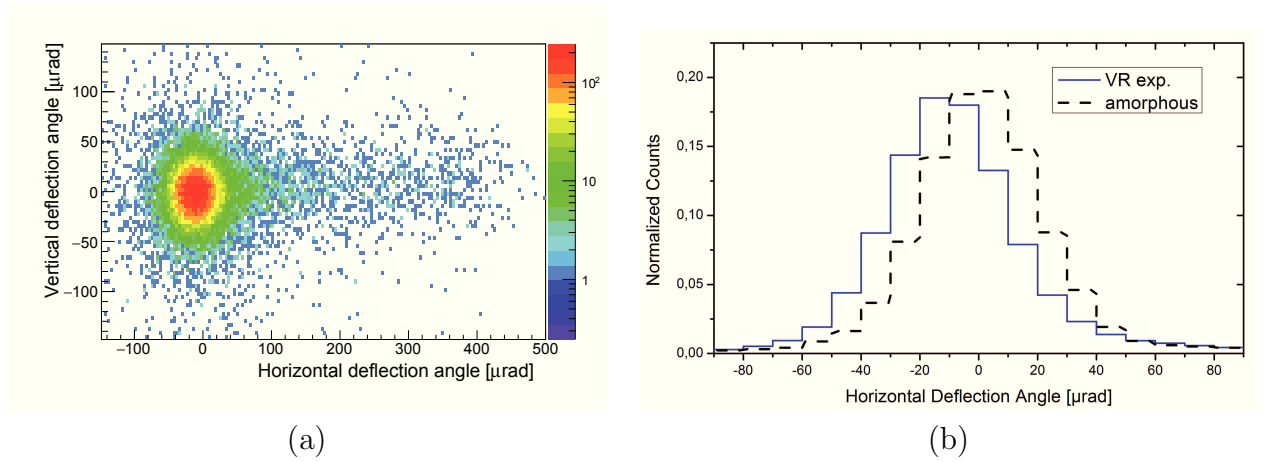


Figure 4.13: (a) XY-distribution of deflection angle of particles interacting with StR3 crystal aligned on volume reflection with the  $(110)_v$  planes. (b) X-distributions of deflection angle for VR (solid) and not-aligned (dashed) orientations.

$0.4\phi$ . The angular divergence of the analyzed portion of the electron beam was  $\sigma_x = (55 \pm 1) \mu\text{rad}$ , being larger than  $\theta_c = \sqrt{2U_0/pv} = \sqrt{2 * 22\text{eV}/120\text{GeV}} \sim 19\mu\text{rad}$  and  $\sigma_y = (65 \pm 1) \mu\text{rad}$ . Fig. 4.13(a) shows the XY-distribution of deflected particles. One

can notice that the most of the beam is deflected towards negative horizontal direction, while a tail of volume-capture particles is visible towards the positive angles. The average deflection in vertical direction is about zero. Fig. 4.13(b) shows the distribution of deflected particles in the horizontal direction for both VR (solid line) and not-aligned (dashed line) cases. A Gaussian fit to the reflected beam distribution yielded a mean deflection angle  $\theta_{VR} = (-11.4 \pm 0.7) \mu\text{rad} \sim 0.6\theta_c$  along the horizontal direction. Deflection efficiency was computed as considering the percentage of events under VR peak within the range  $\in [-\infty < \Delta\theta_x < \theta_{VR} + 3\sigma]$ ,  $\sigma$  being equal to  $(19.9 \pm 0.3) \mu\text{rad}$ , resulting to be  $\varepsilon_{VR} = (95.5 \pm 0.8) \%$ .

### Radiation measurements

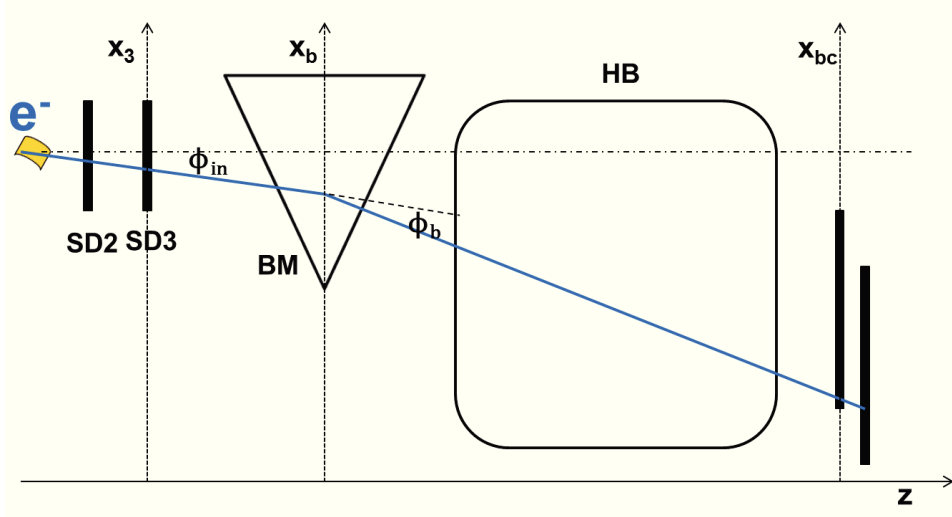


Figure 4.14: A scheme of the spectrometer: the bending magnet (triangle), the helium bag (HB), the silicon beam chambers ( $x_{bc}$ ). The blue line represents an electron trajectory.

By exploiting a *spectrometer method* as in [21], it was possible to measure the particle momentum  $p$  and thereby the energy  $E \approx pc$  of electrons after interaction with the StR3 crystal. Here below a scheme of the method is presented:

- The outgoing angle from the crystal,  $\theta_{x,out}$ , as measured by the tracking system, becomes the incoming angle into the magnet,  $\phi_{x,in}$  (see Fig. 4.14).
- Then, the horizontal position in the magnet center,  $x_b$ , can be determined as:

$$x_b = x_3 + \phi_{x,in} \cdot D_{3,b}, \quad (4.7)$$

$x_3$  being the horizontal position on detector SD3 and  $D_{3,b}$  is the distance between the magnet center and the detector itself.

- Beyond the magnet, the particle crosses the horizontal position where the two large area detectors (BC1-2) are located. The  $x_{bc1}$  ( $x_{bc2}$ ) position measured at detector BCi is used to determine the outgoing angle from the magnet,  $\phi_{x,out}$ :

$$\phi_{x,out} = \arctan \frac{x_{bc} - x_b}{D_{b,bc}} \quad (4.8)$$

where  $D_{b,bc}$  is the distance between the magnet center and the chamber itself.

- Finally, the deflection angle due to the magnet itself is calculated as  $\phi_b = \phi_{x,out} - \phi_{x,in}$ .  $\phi_b$  is connected to the particle energy and the energy lost through eq. 4.1 and 4.2, respectively.

The distance from the magnet to detectors BCi was large enough ( $\sim 13.5m$ ) to achieve a good angular resolution and also to separate the beam from the emitted photons. For instance, those particles that did not lost energy before the magnet ( $E = E_0$ ) were deviated in horizontal position of about  $\phi_{b,0} \cdot 13.5m = 12.15$  cm.

Fig. 4.15 presents a comparison of the beam profile measured by the two chambers  $BC_i$ . BC1 was able to measure the unperturbed beam (corresponding to the main peak) and some of the electrons that did lost energy (the right tail on the plot), while BC2 measured a portion of the perturbed beam.

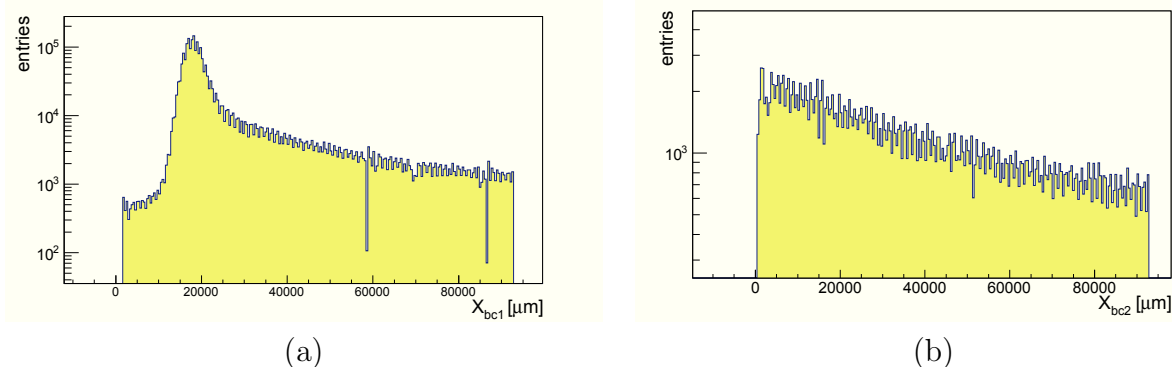


Figure 4.15: The electrons horizontal position,  $x_{bc}$ , measured by the silicon chambers BC1 (a) and BC2 (b), before the alignment.

Since the relative displacement between the chambers in horizontal direction is not known a priori with the required precision, an off-line alignment procedure has been implemented. Fig. 4.16(a) shows the deflection angle measured by the BC1 chamber,  $\phi_{bc2}$ ,

as a function of the angle measured by the BC2 chamber,  $\phi_{bc1}$ , after the alignment procedure, in the region where the chambers overlap. Fig. 4.16(b) the linear fit of this plot is displayed, showing a perfect alignment between the chambers BC1-2.

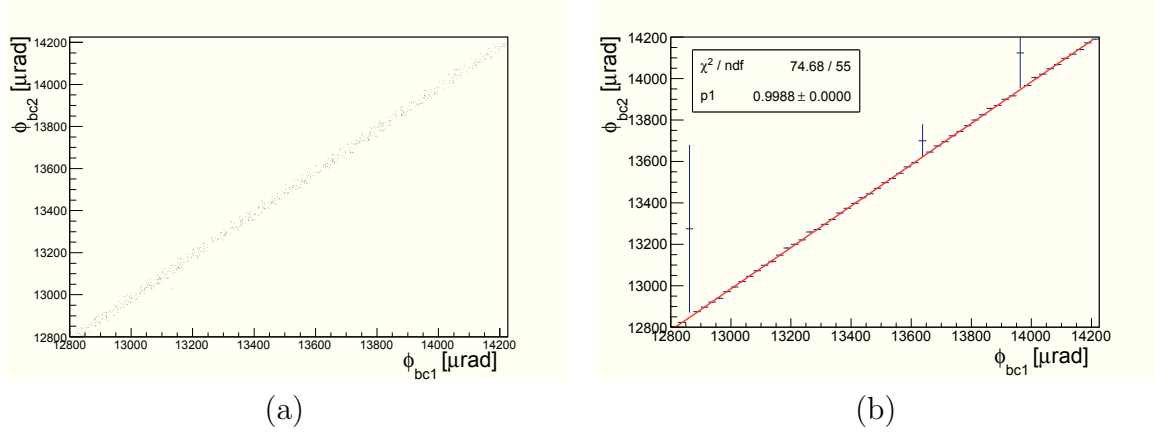


Figure 4.16: (a) The deflection angle  $\phi_{bc2}$  vs.  $\phi_{bc1}$ , after the alignment procedure. (b) Linear fit of the deflection angle  $\phi_{bc2}$  vs.  $\phi_{bc1}$ .

Fig. 4.17 displays the energy distribution of the whole beam measured with both chambers BC1-2: the overlap region results to be in the energy range  $\in [71\text{GeV} \leq E \leq 85\text{GeV}]$ . In our analysis procedure, every time the two chambers measured the same beam energy, a single  $E$  value for each incoming particle is selected in the following way: if the first chamber measures an energy  $E_{bc1} \geq 80$  GeV, it implies that  $E = E_{bc1}$ , whereas when  $E < 80$  GeV, it follows that  $E = E_{bc2}$ .

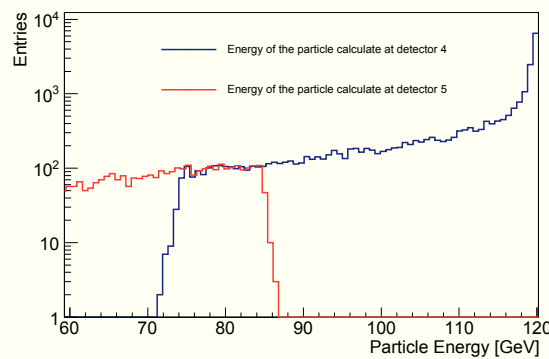


Figure 4.17: The energy distribution of the whole beam measured with both chambers BC1-2.

Figure 4.18(a) shows the total energy distribution measured by the spectrometer. The curve peaks at 120 GeV with a tail due to the particles that had lost energy; events with an

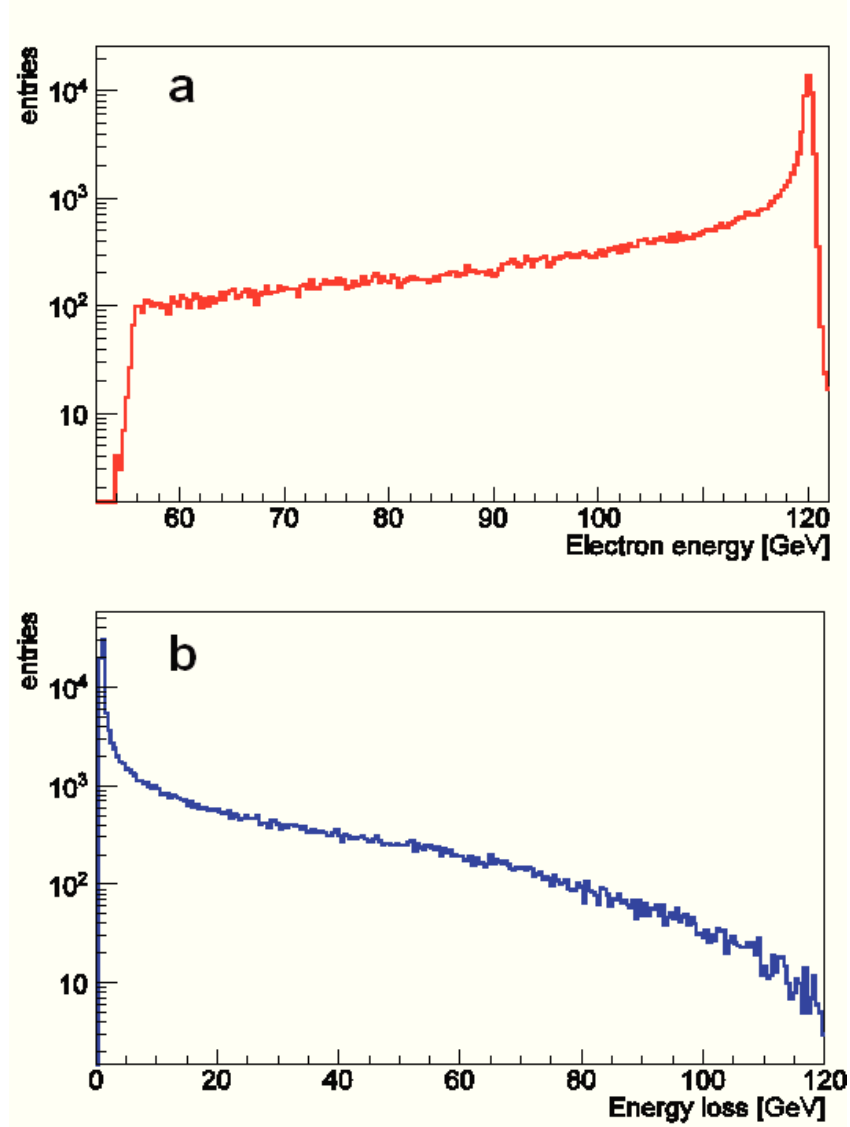


Figure 4.18: a) Electron energy distribution measured by the spectrometer. b) Energy loss distribution measured by the JACK-cal in the full energy range, up to  $E_{loss} \approx 120$  GeV. Adapted from [A2].

energy larger than 120 GeV are due to the intrinsic resolution of the apparatus. The energy-resolution of the apparatus is determined by the energy spread of the particle beam and by the characteristics of the spectrometer itself [86, 92]. The latter is due to the detectors system accuracy (measurement error) and to the multiple scattering contribution of the material before the bending magnet. The various contributions to the energy resolution are generally well approximated by Gaussians [86, 92]. We can estimate the energy resolutions of the spectrometer (at  $E_0 = 120$  GeV), applying a Gaussian fit to the 120 GeV peak of

the whole beam, which resulted to be about 0.33 MeV.

The energy loss of a particle,  $E_{loss}$ , was computed as the difference between the nominal energy of the beam ( $E_0 = 120$  GeV) and the particle energy  $E$ . Due to the finite size of the Si chambers (BCi) the maximum energy loss measurable by the spectrometer was about 62 GeV. Any energy loss larger than this threshold was assessed by the  $\gamma$ -calorimeter JACK, which covers a total of  $19 X_0$ .

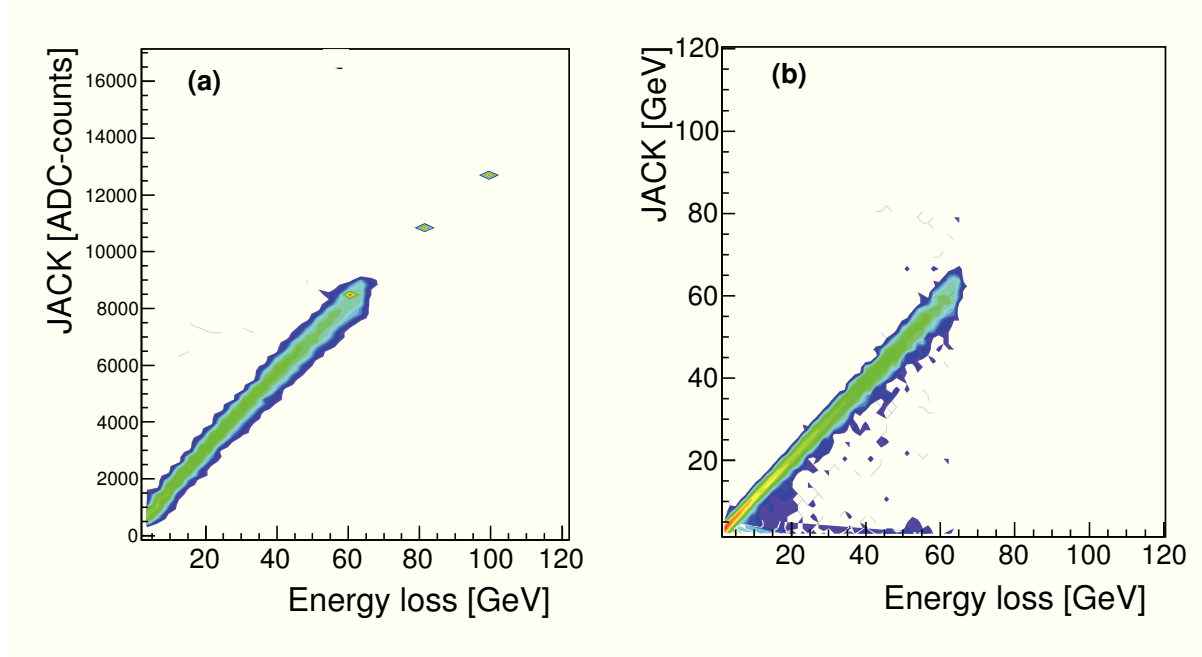


Figure 4.19: a) The energy deposited in JACK-cal (ADC) vs. the energy loss measured by the spectrometer. b) The energy deposited in JACK-cal (GeV) vs. the energy loss measured by the spectrometer.

In order to accept only electrons, an event corresponding to an energy deposition in the DEVA-cal less than the maximum value, i.e., 120 GeV, and for which no photon radiation was recorded by JACK-cal was not identified as an electron and in turn rejected during off-line analysis. The JACK-cal was calibrated by comparing its ADC signals to the energy losses measured by the spectrometer up to 62 GeV. Fig. 4.19(a) shows the JACK-cal output in ADC counts (after the pedestal subtraction) as a function of the energy loss measured by the spectrometer. The transverse spread of the plot is due to the finite resolution of the spectrometer, that implies a finite resolution also for the calorimeter, which was measured to be about 0.5-0.6 MeV at  $E_{loss} = 1$  GeV [92]. Since the correlation between the JACK-cal ADC counts and the energy losses measured by the spectrometer is not linear, the calorimeter calibration was done by plotting the X-mean value and relative RMS for each

Y-bin of Fig. 4.19(a) and then applying a 4<sup>th</sup> degrees polynomial fit. With the aim of calibrating the JACK-cal up to the nominal beam energy, beyond  $E_{loss} = 62$  GeV, the calibration was done through a direct irradiation (with the bending magnet switched off) of a positron beam into the JACK-cal. Three energies were used, i.e., 60, 80 and 100 GeV. The ADC values obtained were also used in the polynomial fit (see Fig. 4.19(a)). Fig. 4.19(b) shows the energy lost in JACK-cal in GeV after the calibration vs the energy loss measured by the spectrometer. The validity of this operation is demonstrated by the perfect linear correlation between the energy loss measured by the spectrometer and the JACK-cal.

Fig. 4.18(b) displays the obtained energy-loss distribution in the full energy range up to the nominal beam energy. Since one of the JACK-cal channels saturated in the region of high energy loss ( $E_{loss} > 75$  GeV) for  $\sim 0.65\%$  of total events, such events were not taken into account in the energy-loss distribution. The normalized energy-loss distribution,  $dn/dE$ , was computed as follows:

$$\frac{dn}{dE} = \frac{\Delta N}{N\Delta E}, \quad (4.9)$$

where  $\Delta N(E)$  is the number of events acquired in the range  $(E - \Delta E/2) \leq E_{loss} \leq (E + \Delta E/2)$ ,  $\Delta E$  being the bin size of the  $E_{loss}$  distribution and  $N$  the number of entries of the histogram including the number of saturated events. The errors were estimated as:

$$\sigma_{\frac{dn}{dE}} = \frac{\sqrt{\Delta N}}{N\Delta E}, \quad (4.10)$$

by neglecting the error on  $\Delta E$  and by assuming  $N \gg \Delta N$ .

The experimental setup of Fig. 4.1 was designed to measure the radiative energy losses of electrons inside the crystal. Nevertheless, one has to consider that bremsstrahlung processes occur also when particles cross the other materials than the crystal along the beamline (such as detectors, scintillator, etc.). This effect originates a background contribution as a result of interaction with the materials before the bending magnet; in fact an electron that lost energy after the magnet cannot be distinguished from an unperturbed one by the spectrometer. An estimate of such contribution was computed during off-line analysis by selecting events that did not cross the crystal.

Fig. 4.20 shows the measured energy loss spectrum,  $(dn/dE)E$ , of volume-reflected electrons (squares with bars) after subtraction of the background contribution. The intensity of the measured VR spectrum starts growing with energy and reaches a plateau at  $\approx 0.11$  within 25-70 GeV, then it slowly vanishes. As expected, the radiation accompanying VR is way more intense than for an amorphous material, which is ruled by Bethe-Heitler

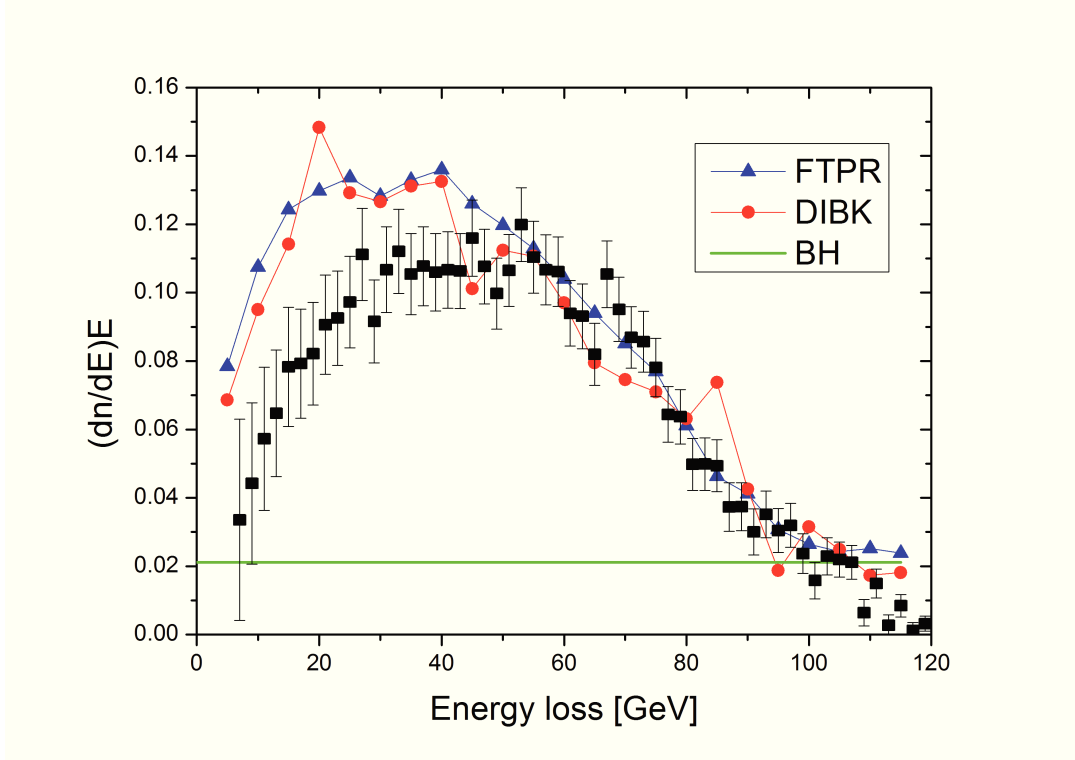


Figure 4.20: Energy-loss spectrum for electrons under VR onto bent Si  $(110)_v$  planes of the StR3 crystal; experimental results (squares with bars); amorphous estimation (solid-line); FTPR (triangles) and DIBK (circles) calculations. Adapted from [A2].

formula and holds  $[(dn/dE)E]_{BH} \approx 0.02$  for a 2 mm long Si crystal (green line).

### Discussion and comparison with Monte Carlo simulations

Two methods of simulations of the radiation generated by high-energy electrons and positrons in crystals implemented by V. Tikhomirov [A1] were used to reproduce experimental results on the radiation accompanying VR and to investigate its behavior while changing some beam parameters.

As introduced in Chapter 2, the mechanism of e.m. radiation emission by high-energy  $e^\pm$  under VR condition is quite complex because the type of radiation changes during the particle motion inside the crystal. In fact, the average misalignment angle between particle trajectory and crystalline planes decreases as the particle approaches to the reflection point [20, 22, 66, 70]. Since the incidence angle is equal to  $295 \mu\text{rad}$ , far from the reflection point the angle between bent planes and particle motion,  $\theta$ , is larger than  $U_{0,p}/(mc^2) \simeq 40 \mu\text{rad}$ ,  $U_{0,p} \simeq 21.5 \text{ eV}$  being the  $(110)_v$  planar potential well depth and  $m$  the electron

mass, ensuring the dipole approximation to be valid and CB theory applicable [4, 9, 63]. While approaching the reflection point, the amplitude of the quasi-oscillatory motion of particles crossing the planes increases, leading to a deflection angle,  $\Delta\theta$ , of the order of the channeling angle  $\theta_{c,p} \simeq 19\mu\text{rad}$ , which is larger than the typical radiation angle  $1/\gamma \simeq 5\mu\text{rad}$ ,  $\gamma$  being the Lorentz factor. It is well known that if  $\Delta\theta > 1/\gamma$  more harmonics can be emitted by the particles and the radiation process turns to synchrotron-like [4, 63]. For this reason, a general way to calculate e.m. radiation generated by volume-reflected particles is to work in the frame of the quasi-classical method developed by Baier and Katkov (BK), as described in Chapter 3.

First, a method for reliable direct integration of BK formula (DIBK) has been worked out and briefly presented in Chapter 3. The other method proposed in Ref. [A1], namely the Fourier transform method for planar radiation (FTPR), consists in the application of the BK formula, simplified by the straight crystal approximation as in Refs. [60, 93, 94] and speeded by fast Fourier integration [95]. This second method is faster but less general than the DIBK one. Both methods take into account realistic trajectories of the particles in the field of coherent interaction with planes and incoherent scattering by nuclei and electrons. Moreover, DIBK and FTPR take into full consideration both the non-dipole nature and arbitrary multiplicity of the radiation process, i.e., the multiple photon emission. Both methods were worked out to investigate the electromagnetic radiation generated by electrons through VR in a bent crystal, according to the experimental conditions presented in the Sec. *Deflection measurements*.

Fig. 4.20 displays the energy-loss spectra as calculated through DIBK method for 10k volume-reflected 120 GeV/c electrons in the StR3 crystal (circles) and obtained through simulation by FTPR method of 200k electron trajectories (triangles). We found good agreement between the results of the two simulations. Direct comparison of the outcomes of the simulations with experimental results highlights a fairly good agreement. In the medium-high energy region of the spectrum the agreement is very good, while in the softer region the calculations overestimate the experimental results. As the energy loss exceeds 108 GeV, the experimental spectrum vanishes instead to attain the BH value. This feature can be explained by the lack of data in the region of high energy loss due to saturation of the calorimeter, which may reduce the energy-loss spectrum at such energies. The similarity between the results of both simulations however suggests that the partial agreement with the experimental results in the soft region of the spectrum requires further investigation. A possible explanation could be the procedure used for background subtraction. In fact, when the probability of radiation emission is small enough ( $\ll 1$ ), the process of VR radiation can be determined by a simple subtraction of the background. In our case, the probability

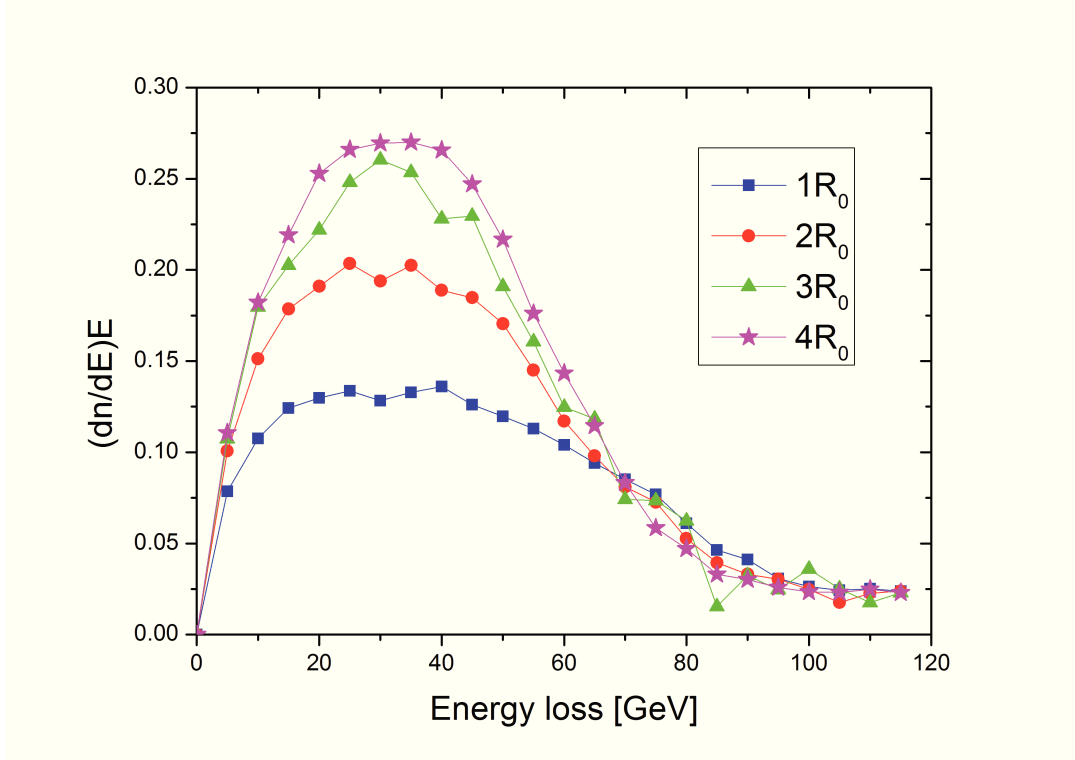


Figure 4.21: Energy-loss spectra calculated through FTFR method for 120GeV/c electrons under VR onto bent Si (110) planes of four 2 mm Si crystals with different bending radii equal to  $R = 1R_0 = 2.71$  m (squares),  $R = 2R_0 = 5.42$  m (circles),  $R = 3R_0 = 8.13$  m (triangles) and  $R = 4R_0 = 10.84$  m (stars). Adapted from [A2].

of radiation emission is not so small, therefore this method does not work properly and has some limitations [96].

Achieved experimental results of Fig. 4.20 can be compared to the existing data in the literature, in particular with those in Ref. [66] obtained with 120 GeV/c positrons. In that paper, it was shown that the shape of VR spectrum depends on the curvature radius. In particular, the more the crystal is bent the greater the contribution of  $\gamma$  emission due to interactions with the planes that are more misaligned with respect to the particle trajectory. These photons are typically harder though radiation is less intense, resulting in a broadening of the spectrum. Therefore, since the StR3 crystal is more bent than the ones tested in Ref. [66], the spectrum exhibits lower intensity and wider distribution.

In order to deepen our understanding on the features of the VR spectrum vs. the curvature radius, we simulated the energy-loss spectra of volume-reflected electrons in four 2 mm crystals with different bending radii, which are integer multiples of the bending radius of the StR3 crystal ( $R_0 = 2.71$  m). For direct comparison, we maintained the same

experimental conditions for data of Fig. 4.20 (squares with bars) excepted for the incidence angle  $\theta_0$ . Since the angular acceptance of VR depends on the bending radius, the ratio  $\theta_0/\phi = 0.4$  was kept constant. The simulations results are shown in Fig. 4.21, confirming the expectation of previous experiments [66], namely the larger the curvature radius the more intense the energy-loss spectrum in the soft-medium region, up to about  $E_{loss} \sim E_0/2 = 60$  GeV. In any case, the increase in intensity due to larger curvature for the hard part of the spectrum appears to be rather modest. In conclusion we claim that the radiation spectrum can be adjusted by changing the curvature of the crystal while using the same beam.

## Summary

A study on the radiation accompanying volume reflection in a curved crystal generated by 120 GeV/c electrons has been presented. First of all, the capability of the St3R strip crystal to efficiently deflect electrons through VR was tested. VR deflection angle and efficiency were found to be  $(11.4 \pm 0.7) \mu\text{rad}$  and  $(95.5 \pm 0.8)\%$ , respectively. The radiation spectrum has been measured by a Si-based spectrometer together with a shashlik electromagnetic calorimeter and resulted to be more intense than for an amorphous medium. With this system, it was possible to measure for the first time the entire VR radiation spectrum of ultra-high-energy electrons, till the nominal energy of the beam. The experimental results are in agreement with theoretical calculations based on the Baier-Katkov quasi-classical method for radiation emission in the field of crystalline planes.

On the strength of the recorded full spectrum, one can conclude that VR is a powerful method for production of hard  $\gamma$  quanta with an energy up to the nominal energy of the particle beam. Moreover, we also investigated the features of VR radiation vs. the bending radius, showing that the radiation can be arbitrary adjusted by changing the curvature of the crystal. We remind here that the most peculiar characteristics of VR radiation are weak dependence on the particle incidence direction, the wide angular acceptance and the low dependence on charge's sign [20]. For all these reasons, VR radiation can be envisaged as a good candidate for interesting applications that will be described in details in Section 4.3.

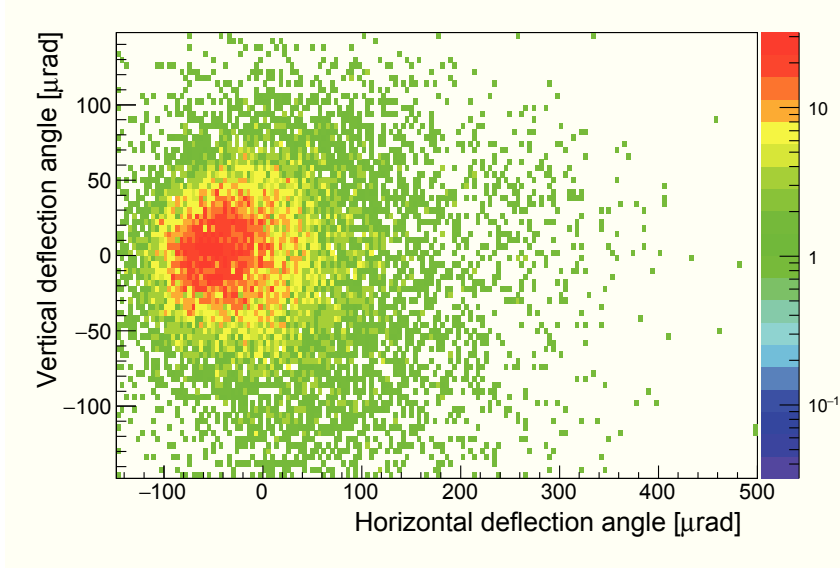


Figure 4.22: Experimentally recorded angular distribution of the deflection angle of particles interacting with the strip crystal aligned on MVROC.

## 4.2.2 Multiple Volume Reflection

### Deflection measurements

A campaign of measurements to investigate the characteristics of the radiation generated by 120 GeV/c electrons under MVROC was carried out at the H4 extracted beamline at CERN SPS with the same experimental setup and crystal that were used to measure the radiation accompanying VR (see Sec. 4.1). The same geometrical cut used in Sec 4.2.1 was implemented during the off-line analysis. Beam divergence of the selected portion of the beam was  $\sigma_x = (50 \pm 1)\mu\text{rad}$  and  $\sigma_y = (65 \pm 1)\mu\text{rad}$  in the horizontal and vertical directions, respectively.

The crystal was aligned with the beam to fulfill Eqs 1.34-1.35 for optimal MVROC, i.e., for horizontal and vertical incidence angles of  $\Theta_{X0} = (365 \pm 5)\mu\text{rad} \approx \phi/2$  and  $\Theta_{Y0} = (205 \pm 10)\mu\text{rad} \approx \phi/3.59$ , respectively. The deflection distribution under MVROC conditions was recorded to determine the MVROC deflection efficiency. The resulted deflected-beam distribution is presented in Fig. 4.22. One can notice that most of the electrons are deflected in horizontal direction, while the vertical deflection is on average zero. Fig. 4.23 shows the horizontal deflection distribution for multi-reflected particles (solid-line). A Gaussian fit of the main peak provided a mean deflection angle in the horizontal direction equal to  $\Theta_{MVROC} = (-43.1 \pm 2.2)\mu\text{rad}$ , i.e., 3.8 times larger than for an individual VR deflection operated by the vertical  $(110)_v$  plane. Deflection efficiency was computed as

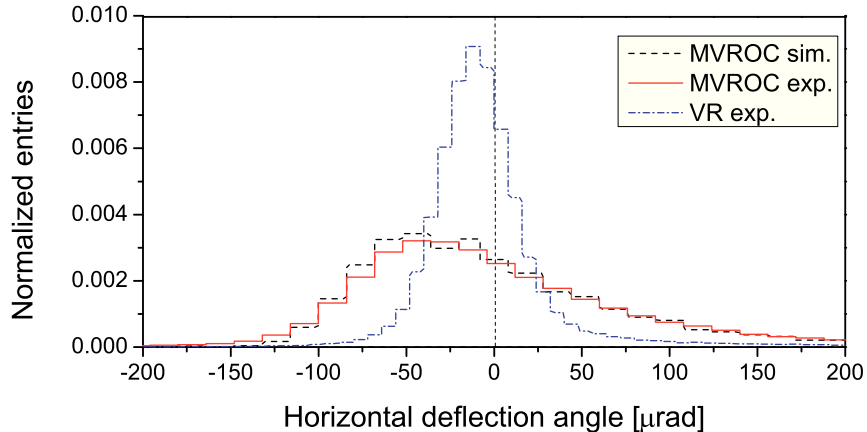


Figure 4.23: Horizontal deflection distribution of volume-reflected (dot-dashed line) and multi-volume-reflected (solid line) electrons. Comparison with simulation results for MVROC condition (dashed line) is also shown. Adapted from [A3].

the ratio between the number of beam particles under the MVROC peak within the range  $\in [-\infty < \Delta\theta_x < \theta_{MVROC} + 3\sigma]$ ,  $\sigma$  being equal to  $(40.8 \pm 1.9) \mu\text{rad}$ , and the total beam particles. It resulted to be  $\varepsilon_{MVROC} = (85 \pm 2)\%$ . The comparison between experimental results and the distribution computed through the Monte Carlo method of Ref. [59] (dashed-line of Fig. 4.23) shows a good agreement.

### Radiation measurements and comparison with theory

Fig. 4.24 displays the experimentally recorded energy-loss spectra under VR (circles with bars) and MVROC conditions (squares with bars). The procedure carried out to determine the energy-loss spectrum,  $(dn/dE)E$ , vs. the energy lost by electrons,  $E$ , is the same of Sec. 4.2.1. Differently from the previous experiment on radiation accompanying VR, the background contribution produced by the material (detectors, etc.) placed before the bending magnet is included in the experimental data. As expected, measured spectral intensity under MVROC conditions is much more higher than the Bethe-Heitler (BH) value (see Fig. 4.24 solid line), typical for bremsstrahlung in amorphous materials. As the energy loss exceeded 105 GeV, experimental spectra vanished instead to attain the BH value. As before, this feature is explained by the lack of data in the region of high energy loss due to the saturation of the calorimeter, which reduced the spectral intensity at such energies. The energy-loss spectrum under MVROC condition exceeds that for VR beyond 10 GeV, being 3 or 4 times stronger within  $60 \text{ GeV} \leq E \leq 80 \text{ GeV}$  and peaks at an energy

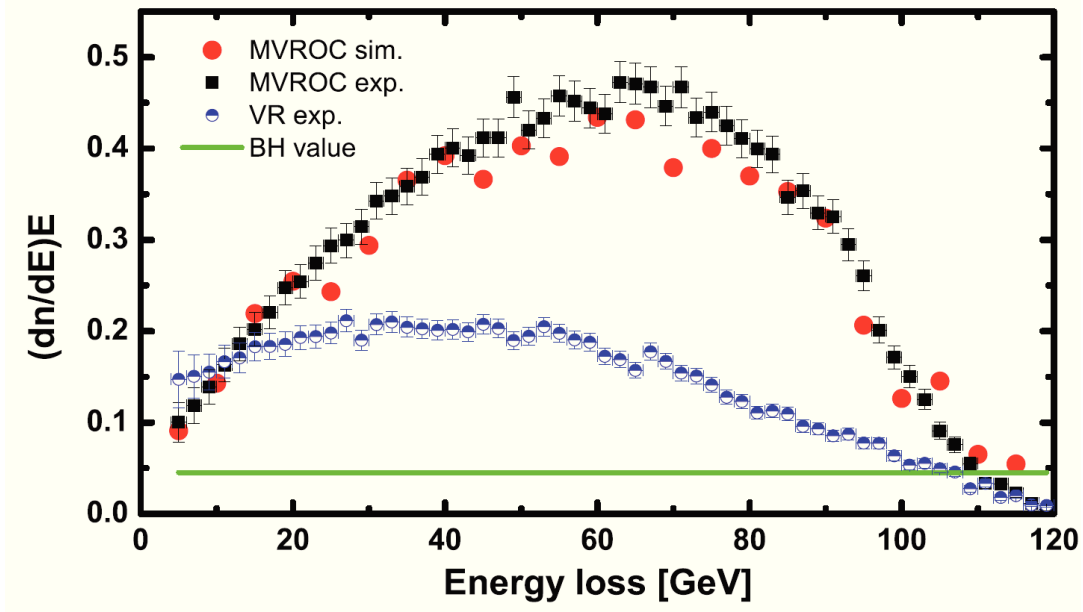


Figure 4.24: Energy-loss spectra for 120 GeV/c electrons in the StR3 crystal; VR experimental results (circles with bars); amorphous estimation (solid-line); MVROC experimental results (squares with bars) and DIBK (circles) simulations. The simulations have been done for 10k electron trajectories in the bent Si crystal. Adapted from [A3].

two/three times larger.

The angle between the particle trajectory and crystal  $\langle 111 \rangle$  axes is about  $\psi = \sqrt{\Theta_{X0}^2 + \Theta_{Y0}^2} = 418 \mu\text{rad}$  at the particle incidence, while decreasing up to  $\psi \sim \Theta_{Y0} = 205$  at the tangency point with  $(110)_v$  bent planes (see schematic view of the transverse plane to the  $\langle 111 \rangle$  axes in Fig. 1.15). As a consequence, since the angle  $\psi$  between atomic strings and particle trajectory is of the order of  $V_{0,a}/m \simeq 200 \mu\text{rad}$ ,  $V_{0,a} = 106 \text{ eV}$  being the depth of the  $\langle 111 \rangle$  axial potential well, the string-of-strings (SOS) radiation under MVROC condition (see Eq. 1.35) can be emitted at very-high energies both in intermediate regime between dipole- and synchrotron-like ones at  $\psi \leq V_{0,a}/m$  and in nearly dipole regime at  $\psi > V_{0,a}/m$ , when the modified CB theory is applicable [4]. Since the multi-reflected particles suffer a strong change in radiation regime during their motion, as for VR the only way to account for all regimes quantitatively is to use the Baier Katkov quasiclassical method.

Fig. 4.24 also shows the energy-loss spectrum simulated for MVROC condition (circles), performed through the DIBK method<sup>2</sup> of Ref. [A1] (see Sec. 3.2). An improvement of calculations allows taking into account the background contribution into in the Monte

<sup>2</sup>In this case, the FTPR method cannot be used, since has been developed to simulate planar effects.

Carlo. Direct comparison of the outcomes by the DIBK method and the experimental results highlights a very good agreement.

The single-photon spectrum (see Fig. 4.25 solid line) is more useful than energy-loss distribution to study the relative contributions of axial and planar fields to the radiation spectrum. According to what expected in theory (see Chapter 2) and to previous simulations (see Fig. 4 in Ref. [60]), the greater intensity for MVROC than for VR in the soft-medium region of the spectra ( $< 30$  GeV) naturally arises from the contribution of several reflecting planes. In more detail, the larger intensity in the soft region ( $< 20$  GeV) is due to synchrotron-like photons, formed in the field of one plane in the region of reflection. Far from the latter, CB-like, and thus harder, photons ( $20 \text{ GeV} \leq \hbar\omega \leq 30 \text{ GeV}$ ) are emitted in the field of several neighboring atomic planes. In fact, the formation of photons in this medium energy range is simultaneously determined by both SOS scattering and planar field contribution. Finally, harder photons ( $\hbar\omega \geq 30 \text{ GeV}$ ) are emitted due to the SOS CB-like process in the field of axis [71], explaining the much stronger intensity of radiation accompanying MVROC in the hard region of the spectrum. One of the consequences of the multiple reflections is the larger number of soft photons than for a single VR, leading to a mean number of photons emitted by each particles (multiplicity factor) equal to  $2.2/e^-$  for  $\hbar\omega > 1 \text{ GeV}$ , which is larger than the value for a single VR for which the multiplicity factor is equal to  $1.35/e^-$ . The MVROC multiplicity factor explains the difference between the single-photon spectrum (see Fig. 4.25 solid line) and energy-loss spectra (see Fig. 4.25 down triangles).

As for VR, the most important advantage of MVROC consists in a wide angular acceptance. The main point is that the dynamics of particles under MVROC conditions is similar to each other for different incidence angles within the total angular acceptance. In other words, particles trajectories under MVROC conditions remain more or less in the same interval of directions of motion with respect to crystal planes and axis for the total angular acceptance. Similar particle's dynamics means similar radiation generation.

Owing to the good agreement between experimental results and simulations, we investigated through simulations the robustness of radiation generated in MVROC orientation vs. beam charge and divergence. Fig. 4.25 displays the results of DIBK simulations for the energy-loss and single-photon spectra of electrons (down-triangles and solid line) and positrons (circles and up-triangles) under the same conditions as in the experiment. Fig. 4.25 also shows the simulated energy-loss spectrum of  $120 \text{ GeV}/c$  electrons with a beam divergence of  $150 \mu\text{rad}$  (squares) and the other parameters unchanged. It is evident that the energy-loss and single-photon spectra in Fig. 4.25 are very similar, demonstrating that radiation is nearly independent of beam charge and divergence. Such features are

explained by a similar dynamics for  $e^\pm$  and for particles with different incidence angles with the crystal.

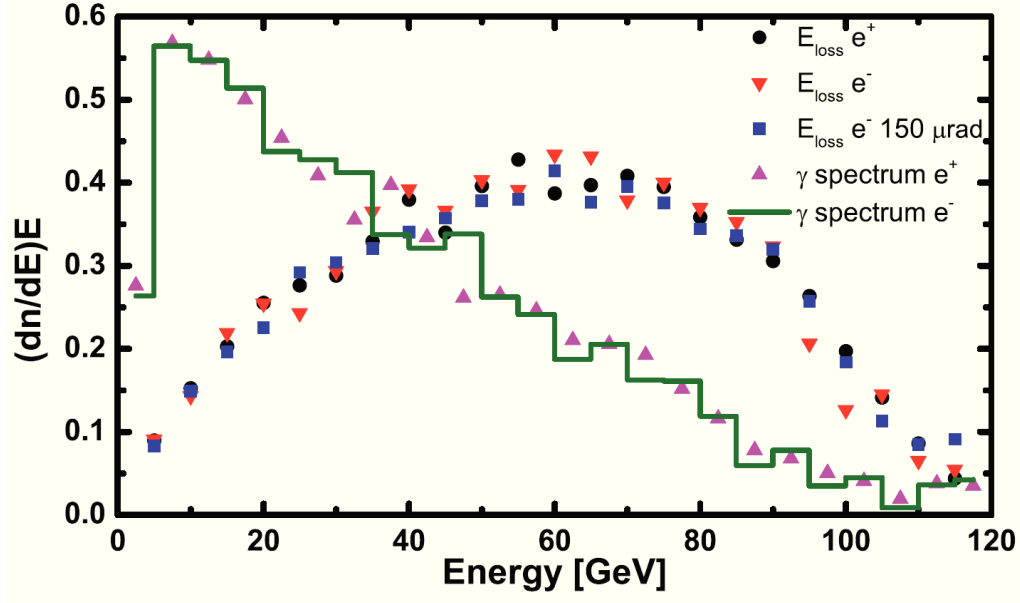


Figure 4.25: Energy-loss and single photon spectra for either 120 GeV/c electrons (reverse-triangles and solid line) and positrons (circles and triangles) simulated under MVROC conditions. Simulated energy loss spectrum for an electron beam with a divergence of 150  $\mu\text{rad}$  and other parameters unchanged (squares). The simulations have been done for 10k particles trajectories in the bent Si crystal under MVROC conditions by using the DIBK method. Adapted from [A3].

## Summary

In summary, the radiation emitted by 120 GeV/c electrons traversing a single bent crystal under multiple volume reflection orientation has been experimentally investigated for the first time. First of all, the deflective power of MVROC has been studied and compared to the case of single VR. The comparison between the two cases is summarized in table 4.1. The energy-loss spectrum of electrons resulted to be very intense over the full energy range up to the nominal energy of the beam. As compared to the radiation emission by an individual volume reflection, the energy-loss spectrum is more intense and peaked at an energy two/three times larger. Experimental results were compared to a theoretical approach based on the direct integration of quasi-classical Baier and Katkov formula (DIBK). In this way, it was possible to determine the mean number of photons emitted by each electron and thus to extract the single-photon spectrum, which resulted to be broad and intense.

Effect	Deflection angle ( $\mu\text{rad}$ )	Deflection efficiency (%)	Comparison with $(110)_v \theta_c$
VR	$-11.4 \pm 0.7$	$95.5 \pm 0.8$	$0.6 \theta_c$
MVROC	$-43.1 \pm 2.2$	$85 \pm 2$	$2.27 \theta_c$

Table 4.1: Deflection angle and efficiencies for single and multiple volume reflection of 120 GeV/c electrons in the St3R crystal.

The soft part of the radiation spectrum is due to the contribution of coherent interaction between electrons and several reflecting planes intersecting the same crystal axis, while the hard part is mainly connected to coherent bremsstrahlung induced by correlated scattering of electrons by atomic strings (strings of strings scattering and radiation, SOS). As for VR, the radiation generation by multiple volume reflection takes place over a broader angular range of the incident beam with respect to channeling radiation and, at ultra-high energies, also to coherent bremsstrahlung in straight crystals [97]. Therefore, this type of radiation can be exploited for interesting applications that will be presented in Sec. 4.3.

## 4.3 Possible applications

### 4.3.1 Intense $\gamma$ -source

All the features of the radiation accompanying VR and MVROC presented in previous sections, such as the high-intensity and the wide angular acceptance, make these kinds of radiation very attractive for several applications at once. Additional advantage of radiation generation relying on VR is its robustness vs. crystalline imperfections as compared to channeling-based effects [79]. In contrast to channeling, the presence of crystal defects is not crucial in the case of VR and the deflection efficiency is practically the same as for a perfect bent crystal. Moreover, the local nature of the reflection effect will also assure the weak sensitivity to crystal mosaic structure. Such a possibility envisages also the usage of higher-Z materials, which are better than Si for e.m. generation because of their higher atomic potential [98], but they cannot be produced with the same perfection as Si. For instance, since the average electric field strength in W is about an order of magnitude stronger than in silicon, we expect that the advantages of the radiation accompanying VR and MVROC measured in Si at 120 GeV will be maintained in W at lower energies (about 10 GeV), available at many worldwide electron accelerators. In order to maintain the advantages of a broad angular acceptance at lower energies, one has simply to adjust the crystal curvature. For all these reasons, e.m. radiation under VR and MVROC in

a tungsten crystal could be exploited to convert high-emittance electron beams to high-intensity  $\gamma$ -beam. In order to obtain an high-intensity gamma source, MVROC could be a preferable choice than VR due to the contribution of both crystal axis and multiple reflecting planes.

### 4.3.2 Crystal-assisted collimation in electron/positron colliders

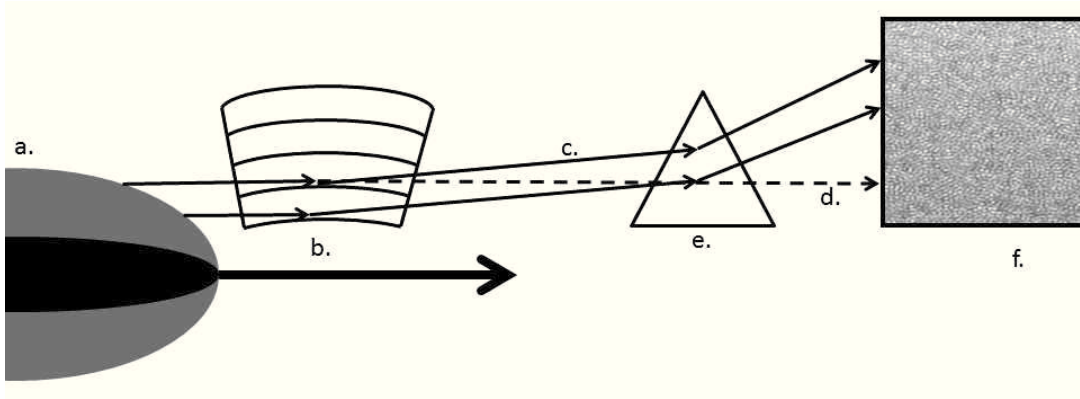


Figure 4.26: Concept of linear collider collimation system based on VR-MVROC radiation phenomenon [39]. In the figure a. is the beam, having a core and a halo, b. is the bent crystal oriented in VR-MVROC conditions, c. solid lines are the particles from the beam halo that have been deflected and have lost energy due to VR-MVROC, d. dashed-line represents the photons produced during VR-MVROC, e. is the bending magnet, separating halo particles that have lost a significant part of their energy during VR-MVROC, and f. is the absorber of halo particles and photons. Adapted from [A4].

One of the most attractive applications that would take advantage of the features of VR and MVROC from both the points of view of radiation and deflecting power could be a crystal-assisted collimation device for future electron-positron colliders, e.g., the International Linear Collider (ILC) [99] or the Future Circular Collider (FCC) [100]. ILC is a proposed electron-positron collider with a planned collision energy of 500 GeV and a possible upgrade to 1000 GeV. The beam will be delivered in pulsed bunches; these bunches are not uniformly distributed and have *halo* particles which need to be removed to avoid unacceptable background in the detectors. To remove the halo particles, the beam will be collimated in its delivery system. The baseline design requires two-part collimators made up of small aperture spoilers with  $0.5-1$  radiation length ( $X_0$ ) thickness close to the beam, and downstream absorbers  $30 X_0$  thick [101]. Since the spoilers are placed very close to the beam, the beam-spoiler interactions result in wakefield perturbations [102].

The insertion of a short (1-2 mm  $\sim 0.02 X_0$ ) Si crystal instead of a Ti spoiler of some cm of length would diminish the wakefield perturbations. A proposal in this sense has already been put forward by Seryi [19]. Such collimation scheme consists in replacing one or more spoilers with bent crystals oriented with the beam under VR. The choice of VR instead of channeling is connected to its larger angular acceptance and larger deflection efficiency with respect to channeling [35]. Particles deflection by VR would increase halo-cleaning efficiency per unit of length as compared to the case of an amorphous spoiler. Furthermore, the larger energy-loss spectrum in VR than in amorphous media would improve the discrimination of halo particles, which will be deflected by forward magnets. The larger deflection and the greater energy loss in MVROC condition than the case of an individual VR, makes MVROC radiation even more suitable for crystal-assisted collimation of future linear colliders. The choice between VR and MVROC will depend only on the required deflection efficiency and on the possibility of crystal-beam alignment in one or two directions. Fig. 4.26 shows a possible scheme for crystal assisted collimation through VR-MVROC and briefly summarizes the various steps described above. Finally, it should be reminded that the energy-loss spectrum under VR-MVROC conditions is nearly independent on the particle charge and so it is almost the same for either electrons or positrons, which makes these two coherent effects even more attractive for collimation in  $e^\pm$  colliders.

## Chapter 5

# Investigation on coherent interactions of sub-GeV electrons for beam steering and high intense e.m. radiation generation

To date, crystal-assisted beam steering has been extensively investigated for positively charged particle beams, spanning from MeV [103] to 1 GeV [104], to hundreds GeV [105] up to TeV energies [106]. The usage of bent crystals has also been suggested to collimate the 7 TeV beam in the Large Hadron Collider (LHC) [17] and to realize an extracted beamline from the LHC [107].

On the contrary, little has been investigated concerning the steering of negatively charged particle beams via channeling in bent crystals because, unlike the positive particles, negative particles repeatedly oscillate across the nuclei of the crystal, leading to an increase of particle dechanneling about ten times larger than for positive charges (see Sec 1.1.2). The first experiments attempting the steering of negative-particle beams through bent crystals were unsuccessful [108, 109] because crystals with length much larger than the dechanneling length were used. In such cases, channeled particles were scattered out of the crystal and no particle arrived at the angle of the nominal deflection of the crystal. Only in the last years, experiments performed with 150 GeV negative pions [35, 110] demonstrated that a crystal with a length comparable with the dechanneling length (about 1 mm at that energy) allowed the achievement of channeling up to the nominal bending of the crystal as for their positively charged counterparts.

Concerning the steering of coherent interactions of negatively charged particles in bent

crystals, relevant applications have been suggested over a wide range of energies. The main interest is on electrons, which can be exploited not only in beam-steering, but also in  $\gamma$  radiation generation. Positrons also can generate e.m. radiation, but  $e^+$  beams are rare and usually cannot be provided with the same high-quality as for  $e^-$  beams. As we have seen in Chapter 4, the combination of steering and intense radiation generation, can be exploited for a crystal-assisted collimation in future  $e^\pm$  colliders. Moreover, the radiation accompanying volume reflection (VR) in curved crystals can be exploited for a  $\gamma$ -source with low-emittance beams. The few existing studies on VR radiation have been done with hundreds-GeV beams [20, 22, 66, 68, 69], because of the technological difficulties to build a crystal with the needed characteristics to steer GeV electrons. Nevertheless, the possibility to steer sub-GeV and GeV electron beams via channeling and VR in bent crystals would open up a new challenge for e.m. radiation generation in bent crystals within the energy range accessible by many electron accelerators worldwide. In fact, there is some wealth of data concerning the radiation emitted by electrons in straight crystals in the sub-GeV/GeV energy range interesting for X- or  $\gamma$ -ray sources, while no data for radiation with bent crystals does exist in the literature. Furthermore, beam steering in periodically bent crystals has been proposed for the realization of innovative high-intensity radiation sources ([23] and references therein).

In the GeV energy range, steering of negatively charged particles through bent crystals has never been reported mostly because of the difficulties to fabricate a bent crystal featuring a short thickness along the beam. Indeed, since the dechanneling length for GeV electrons is of the order of tens of  $\mu\text{m}$  [53], their efficient steering requires a bent crystal with a thickness comparable with such a length.

In this Chapter, we report about efficient steering of 855 MeV electrons by means of planar channeling and VR performed at the MAInzer MIkrotron (MAMI) [A5]. The same crystal has been used to investigate the radiation generated by the same electron beam through the same coherent phenomena [A9]. Such study allows one to investigate the influence of the crystalline curvature on the radiation emitted by sub-GeV electrons in a bent crystal and thereby the radiation accompanying VR within an unexplored energy range.

## 5.1 Experimental Setup at MAMI B

The Mainz Microtron (MAMI) is an accelerator for electron beams with a maximum energy of 1.5 GeV available at the Institute for Nuclear Physics of the University of Mainz [84].

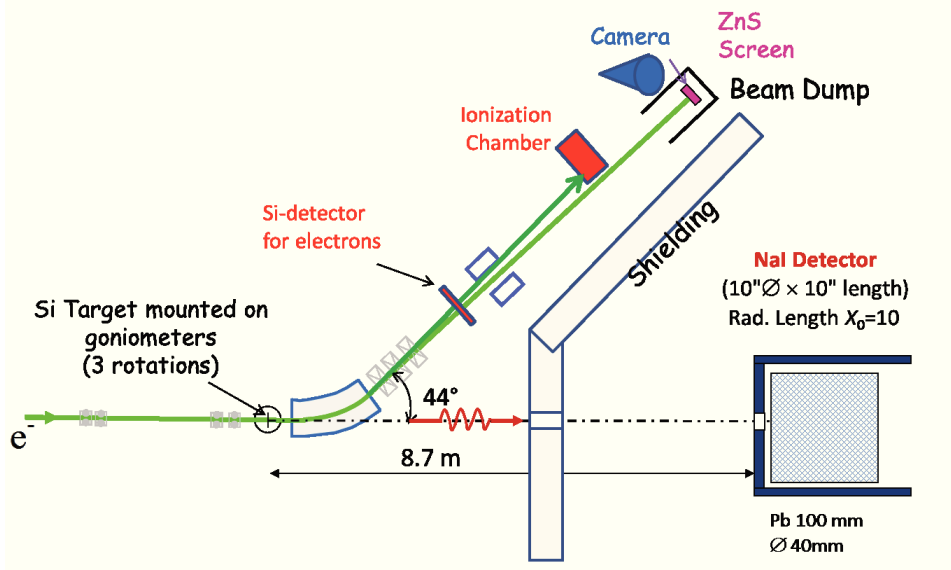


Figure 5.1: Scheme of the experimental setup at MAMI B. After the interaction with Si target mounted on a high precision goniometer, the 855 MeV electron beam is deflected horizontally by a bending magnet. A Si strip detector is placed 5.973 m downstream of the crystal to measure the beam distribution after interaction. Then a ionization chamber is positioned after a second dipole-magnet, which deflects particle along the vertical direction. It is employed to detect channeling. Just in front of the beam dump the beam spot can be monitored with a ZnS luminescent screen which is viewed by a CCD camera. The neutral beam of photons arrives at a NaI scintillator detector after 8.627 m from the crystal. The NaI detector is shielded by a 100 mm thick lead wall with a 40 mm opening to accept most of the photons. The scheme is adapted from a previous one presented in [53].

MAMI is a so-called continuous wave accelerator, thus the electron beam is not clustered in bunches as it is the case for most accelerators. On the contrary, the beam is seen by detectors as a continuous current.

An 855 MeV electron beam, available at the MAMI B facility, was conditioned to a beam size of  $200 \times 70 \mu\text{m}^2$  and a divergence of 70 and  $30 \mu\text{rad}$  along the horizontal and vertical directions, respectively, i.e., much less than the planar critical angle, being about  $217 \mu\text{rad}$  at 855 MeV for the Si (111) planes.

The experimental setup of [53] was upgraded with a single-sided microstrip Si detector [111], namely a unit of the INSULAB Telescope of the University of Insubria, Italy (see Fig. 5.2(a)). The Si detector has an intrinsic spatial resolution of  $10 \mu\text{m}$  [112] and was used to reconstruct the beam profile after the interaction with the crystal (see Fig. 5.1). A bending magnet separates the photons emitted by the 855 MeV electrons inside the crystal from the charged beam. The Si detector was placed 5.973 m downstream of the crystal along the  $e^-$ -

beamline, allowing an angular resolution of better than  $10 \mu\text{rad}$ , i.e., much smaller than the critical angle. On the other hand, the photon beam, which is not deflected by the magnet, after 8.627 m from the crystal arrives at a  $10'' \times 10''$  NaI scintillator detector, readout by three standard PMTs. An aperture of 40 mm diameter in the lead shield surrounding the detector permits the collection of a portion of the emitted photons, resulting in a collimator aperture of 4.63 mrad, i.e., equal to  $\sim 7.8$  times the typical radiation angle,  $1/\gamma$ . In this way, it was possible to collect most of the emitted photons. The entire experimental setup was kept under vacuum to avoid multiple scattering of the beam by air.

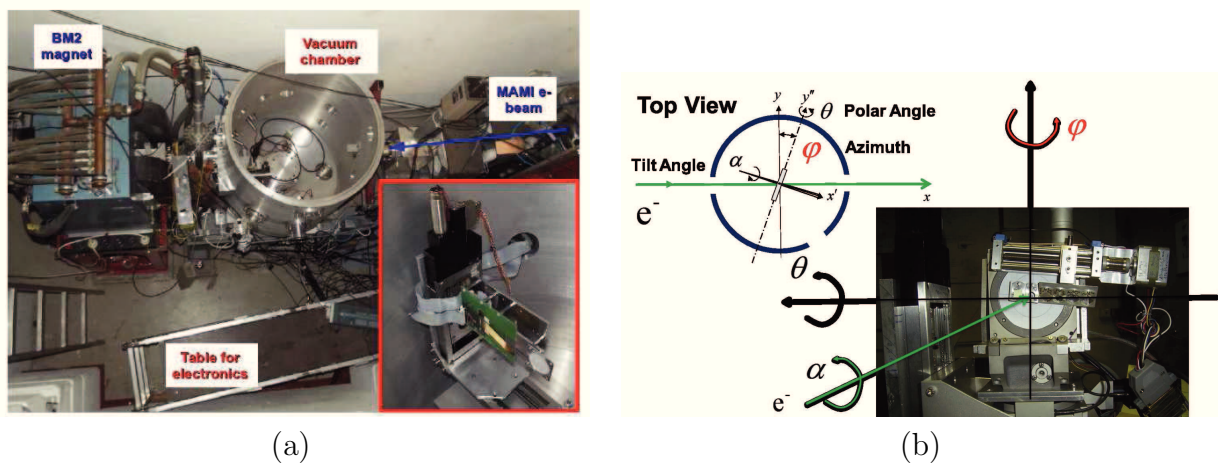


Figure 5.2: (a) Picture of the Si single-sided detector station (b) A scheme and a picture of the goniometric system. Adapted from [111].

A bent crystal suited for steering of sub-GeV electrons was manufactured through a newly developed technique at the Sensors and Semiconductor Laboratory (SSL) of the University of Ferrara [113, 114]. It consists of a plate-like Si crystal with  $(30.5 \pm 0.5) \mu\text{m}$  thickness along the beam, fabricated by starting from a  $500 \mu\text{m}$  thick (211) Si wafer. These crystallographic orientations were selected to obtain (111) bent planes, which are the most efficient for the deflection of negative-charged particles. The  $30.5 \mu\text{m}$  thick crystal was mounted onto a mechanical bending holder. A bending moment supported the crystal at two opposite edges, while it was free at the remaining edges. As one can see in Fig. 5.3, the crystal surface, which is parallel to the (211) planes, was bent along the  $\langle 111 \rangle$  direction. In this way a secondary bending of the (111) planes was obtained due to the quasi-mosaic effect [115]. The advantages of a quasi-mosaic crystal is the possibility to manufacture ultra thin crystals being large enough to intercept wide beams.

Then, the crystal was characterized by high-resolution x-ray diffraction (Panalytical X-Pert MRD-PRO), measuring a bending radius of 33.5 mm, being approximately 23 times

the critical radius for electron channeling at 855 MeV ( $R_c = 1.5$  mm). The crystal lateral sizes were optimized to suppress parasitic anticlasic deformation across the central region of the crystal [113]. The small dimension of the beam ( $\sim$  hundreds microns) as compared to the crystal surface ( $23 \times 15$  mm<sup>2</sup>), assures that the whole beam impinged onto a uniform flat surface.

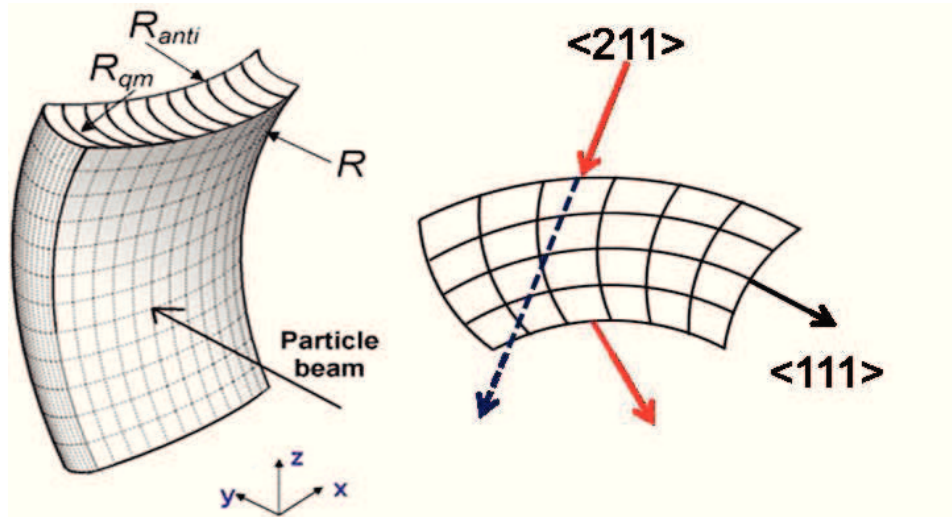


Figure 5.3: (a) Sketch of the bent silicon plate-like crystal. External forces generate a primary curvature with radius  $R$ , which results in a secondary (quasi-mosaic) curvature with radius  $R_{qm}$  due to anisotropy-induced deformation. Unwanted anticlasic deformation with radius  $R_{anti}$  also appears as a result of primary bending. (b) Scheme of the top view of the beam interaction with the quasi-mosaic crystal, with highlighted the crystallographic directions. Solid arrows correspond to incoming and outgoing channeled particles from the crystal, while dashed arrow represents the incident direction of the particle. Adapted from [113].

The crystal holder was mounted on a high-precision PI-MICOS goniometric system equipped with 5 degrees of freedom (see Fig. 5.2(b)). The crystal was oriented to deflect particle in vertical direction, i.e., opposite to that of the bending magnet. Translations along the  $x$  and  $y$  axes were used to geometrically align the crystal with the beam with an accuracy of  $1 \mu\text{m}$ , while rotations around the  $x$ ,  $y$  and  $z$  axes with an accuracy of 50, 9 and  $175 \mu\text{rad}$ , respectively, were used to achieve angular alignment of the crystal planes with the electron beam.

Fig. 5.4 represents a scheme of the Si quasi-mosaic crystal used in MAMI (a) and of the experimental setup on the *electron-beamline* after the magnet (b). The red arrow indicates the incoming beam, impinging on the crystal mounted on a high-precision goniometer (G). The gold arrow indicates particles deflected thanks to planar channeling, pink arrow

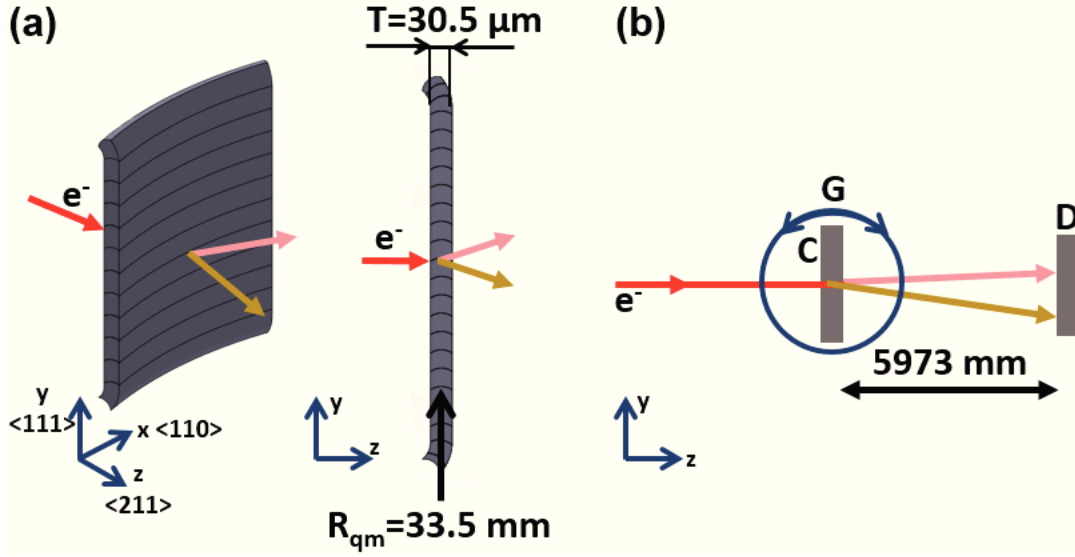


Figure 5.4: (a) Bending of a silicon plate-like crystal with properly chosen crystallographic orientations generates the quasi-mosaic effect, resulting in a secondary bending of the planes lying in the crystal thickness. (b) Sketch of the experimental setup on the electron-beamline. The red arrow indicates the incoming beam, impinging on the crystal mounted on a high-precision goniometer (G). The gold arrow indicates particles deflected thanks to planar channeling, pink arrow corresponds to over-barrier particles. A silicon detector, (D), reconstructs the beam profile after interaction with the crystal. Adapted from [A5].

corresponds to over-barrier particles. A silicon detector, (D), reconstructs the beam profile after interaction with the crystal.

## 5.2 Steering of sub-GeV electrons

A preliminary alignment between the beam and the bent crystal was done with the usage of the ionization chamber as in [53]. Then the crystal was rotated around the x axis and, for each angular position (one every 0.003 degrees  $\approx 52\mu\text{rad}$ ), the particle distribution after interaction with the crystal was recorded. A peculiarity of this experimental scheme is the separate observation of channeled and dechanneled particles, which cannot be done by using a straight crystal.

The electron deflection distribution after interaction with the crystal vs. the crystal-to-beam angle is shown in Fig. 5.5(a). In regions (1) and (6), the beam trajectory is always misaligned with bent (111) planes. In region (2), the crystal is oriented for channeling, which arises as the beam impinges onto the crystal planes at an angle less than the critical angle for channeling ( $217\mu\text{rad}$ ) [1]. Under such conditions, particles with a transverse

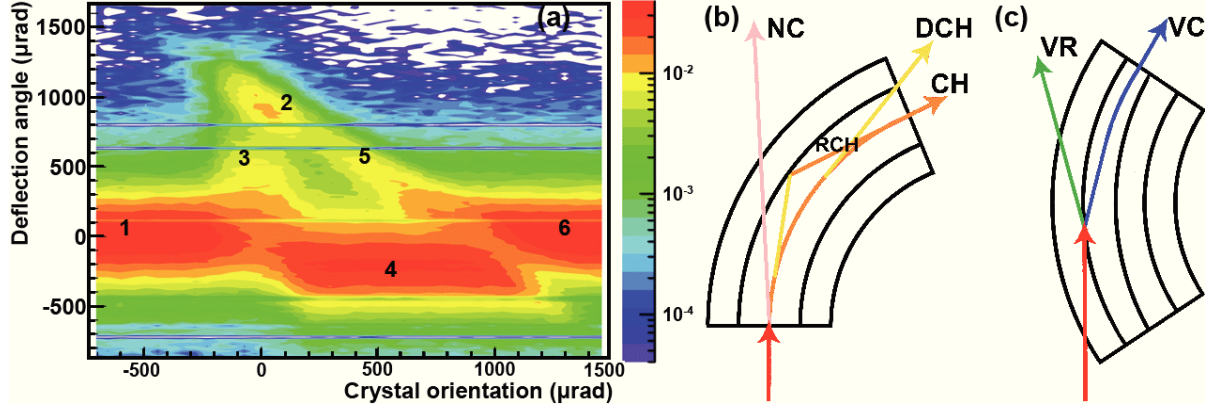


Figure 5.5: (a) An angular scan recorded during the interaction between the crystal and the electron beam. Six different regions can be distinguished: (1) and (6) non-channeling; (2) channeling; (3) dechanneling; (4) volume reflection and (5) volume capture. (b) The bent crystal planes are aligned with respect to the charged particle beam within  $\pm$  the critical angle, i.e., channeling is possible (red straight arrow). Over-barrier particles are deflected toward the opposite side as that of crystal bending. Under-barrier particles are captured under the channeling regime (orange arrows). Due to multiple scattering, channeled particles may suffer dechanneling (yellow arrow). A fraction of dechanneled particles experiences rechanneling. (c) Bent crystal is aligned with respect to the incoming particle beam (red arrow) in such a way that the beam trajectory becomes tangent to the atomic planes inside the crystal. Under such regime, either VR (green arrow) or the competitive process of VC (blue arrow) occurs. Adapted from [A5].

energy  $E_T < U_0$ ,  $U_0$  being the planar potential well depth for the bent Si (111) planes are captured into the channel. However, due to multiple scattering, channeled electrons may be subject to an increase in their transverse energy and overcome the interplanar potential barrier, i.e., the electron is dechanneled (region (3)). The inverse of such a process may also occur, i.e., an over-barrier electron, with  $E_T > U_0$ , loses part of its transverse energy due to multiple scattering and gets trapped in channeling mode, i.e., the particle is rechanneled (see Fig. 5.5b). The mechanism of rechanneling regards also particles that have been previously dechanneled. Regions (4) and (5) correspond to VR and volume capture (VC), respectively. Those phenomena manifest as the crystal is oriented in such a way that, even in the case of an incidence angle larger than  $\theta_c$ , the beam trajectory becomes tangent to the bent atomic planes in the crystal bulk. Under such conditions, most of the particles undergo VR [16], while a fraction of the beam may be captured into the channeling regime (VC) due to incoherent scattering with nuclei and electrons [34] (see Fig. 5.5(c)). Fig. 5.5(a) highlights also the large angular acceptance for both VR and VC, which is equal to the crystal bending angle.

Finally, we can notice that the 2D-distribution of Fig. 5.5(a) has the same structure of the one obtained with a hundreds-GeV negative beam (150 GeV  $\pi^-$ ) interacting with a bent Si crystal of millimetric thickness [35]. As a result, we can state that the same phenomena of deflection through coherent interactions were observed both at 150 GeV and at 855 MeV.

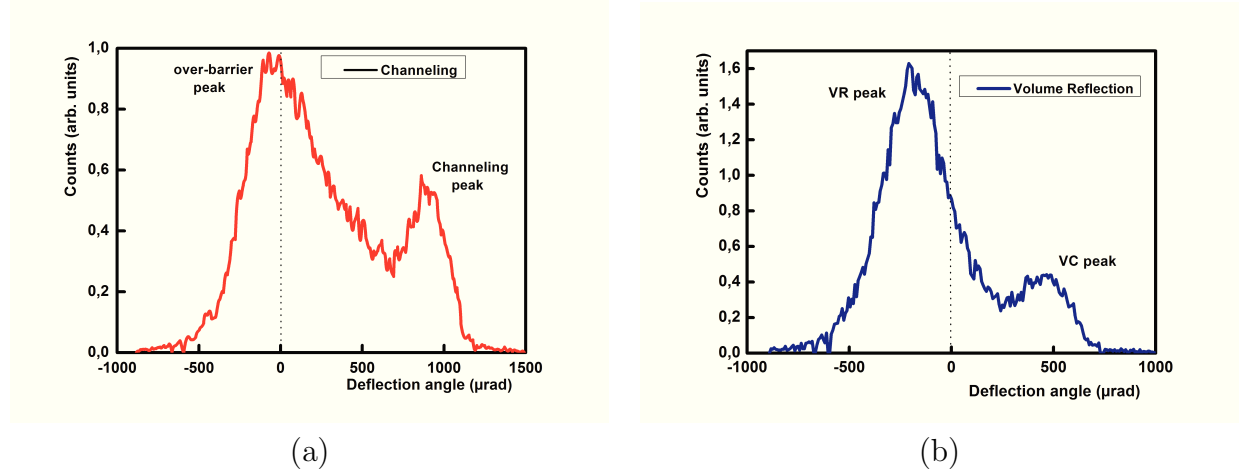


Figure 5.6: (a) Beam profile recorded after interaction of electrons with the crystal aligned for channeling. As the crystal is oriented in channeling, a large fraction of the beam is deflected to the nominal deflection of the crystal (right peak). Particles found in over-barrier at the crystal entry face populates the left peak in the distribution, while region between the two peaks is populated by particles suffering dechanneling. (b) Beam profile with the crystal aligned for VR. As the crystal is oriented in VR condition, a largest fraction of the beam is steered toward the direction opposite of channeling (left peak). VR efficiency is limited by capture of particles in channeling (VC-right peak), which are deflected along the crystal bending.

Fig. 5.6 shows beam profiles under either channeling (a) or VR (b) alignments. In Fig. 5.6(a), the peak on the right corresponds to the particles deflected under channeling, while the other peak represents the overbarrier particles. Fig. 5.6(b) shows the deflection occurring as the crystal is oriented  $\sim$  in the middle of the VR region (450  $\mu\text{rad}$  far from the perfect alignment with the (111) bent planes). The peak on the left represents properly the volume-reflected particles, while the peak on the right represents the volume-captured particles.

To determine the channeling and VR mean deflection angles and efficiencies, a Gaussian fit of the channeling peak in Fig. 5.6(a) and of the VR peak in Fig. 5.6(b) were done. The deflection efficiency has been estimated as the fraction of deflected particles within  $\pm 3\sigma$ . The results are summarized in table 5.1. As expected, VR deflection angle is much

smaller than channeling one, while VR efficiency is much larger (76.7% vs. 20.1%). As for the higher energies case (see Chapter 4) the VR deflection angle is smaller than  $\theta_c$ .

Effect	Deflection angle ( $\mu\text{rad}$ )	Deflection efficiencies (%)
Channeling	$910 \pm 5$	$20.1 \pm 1.2$
Volume Reflection	$-191 \pm 10$	$76.7 \pm 1$

Table 5.1: Deflection angles and efficiencies for both channeling and VR cases.

Following the method of Refs. [46], the channeling beam profile of Fig. 5.6(a) was fitted as the sum of two gaussians around the two peaks and one exponential curve between them. The decay constant of the exponential term provides a direct experimental measurement of the dechanneling length, which resulted to be  $L_n = (19.2 \pm 1.5) \mu\text{m}$ .

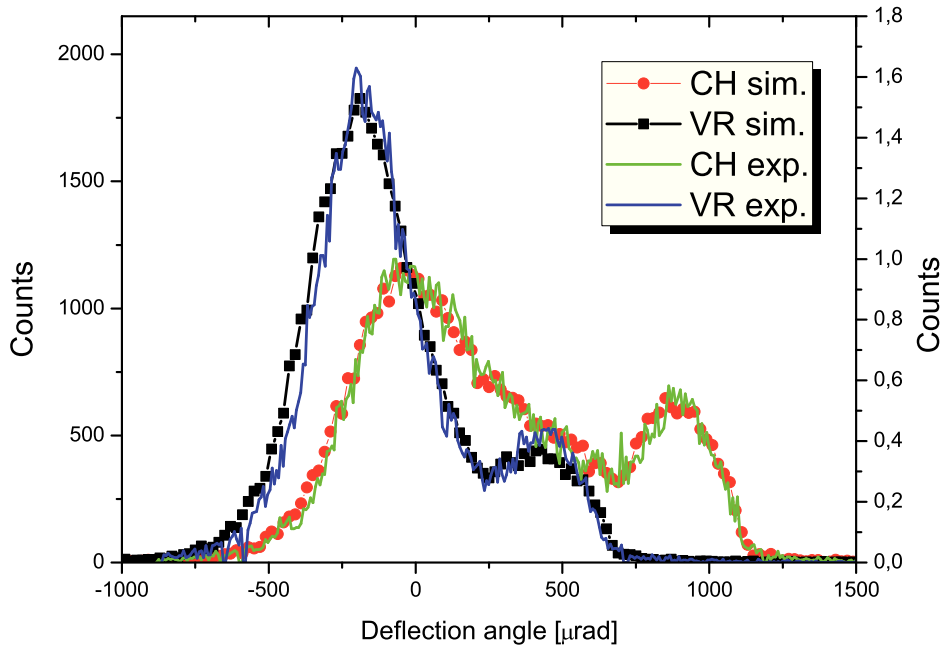


Figure 5.7: Simulated beam distribution after interaction with the  $30.5 \mu\text{m}$  bent crystal aligned parallel with the bent (111) planes at the entry face of the crystal (circles) and under VR (squares) conditions with incidence angle w.r.t. to bent planes equal to  $450 \mu\text{rad}$ . For comparison, the solid lines reproduce the experimental results presented of Fig. 5.6. Adapted from [A8].

The DYNECHARM++ code [78] has been used for prediction of the outgoing particle

distribution from the crystal. More information about the code can be found in Ref. [78] and references therein. Fig. 5.7 displays the simulated angular distribution of the 855 MeV beam after the interaction with the crystal under channeling (circles) and VR (squares) conditions, showing a good agreement with experimental results (solid lines).

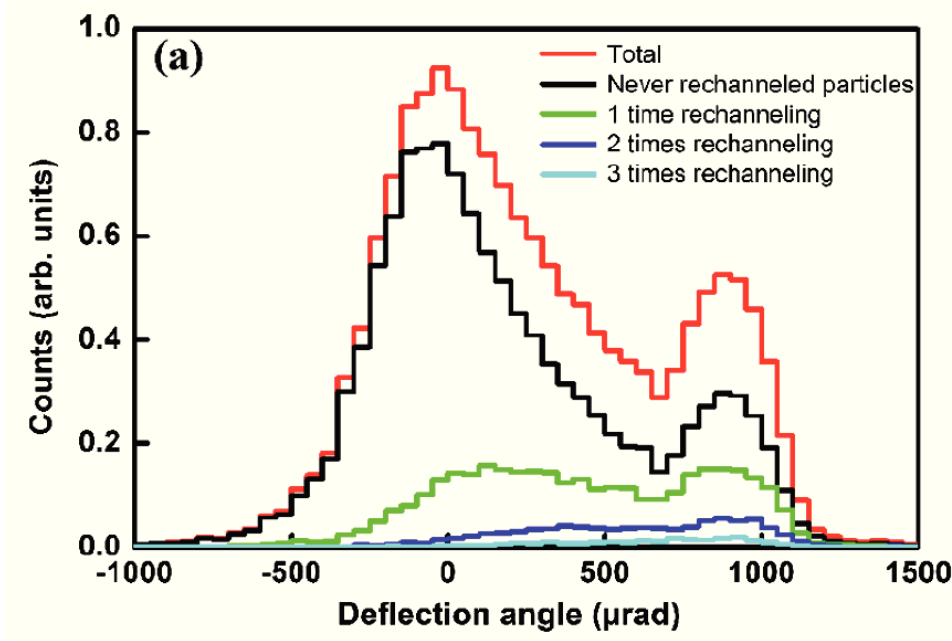


Figure 5.8: Monte-Carlo simulation of the contributions to the angular distribution originated from rechanneled particles. The red line represents the whole distribution; black line represents the particles that have never been rechanneled; green, blue and light blue lines represent the distribution of the particles rechanneled 1, 2, 3 times respectively. Adapted from [A5].

A theoretical study conducted by V. Tikhomirov through Monte Carlo simulations [116], highlights the contribution of both single and multiple rechannelings to build up the channeling peak of Fig. 5.6(a). Fig. 5.8 shows the fraction of channeled particles with and without taking into account the fraction of rechanneled electrons. About 55% of the particles recorded under the channeling peak has been rechanneled at least once. Analysis of simulations output shows that the dechanneling length causing an e-fold of the fraction of channeled particles for permanently channeled electrons (5.8 black-line) is  $L_{n,p} = 13.6 \mu\text{m}$ . It becomes  $L_n = 19.5 \mu\text{m}$  if the total fraction of channeled particles, including the rechanneled ones is considered (5.8 red line). The latter value is in good agreement with the experimentally measured one.

This strong contribution of rechanneling is expected from the reversibility rule (see Sec. 1.1.2). As there are particles that exit from the crystal channel, there have to be

particles entering the channel. Since for channeled negative particles, the possibility of suffering dechanneling is increased than for positive charges due to the strong contribution of multiple scattering with nuclei, the same has to be for rechanneling that is caused by the same phenomenon.

If the particle dynamics is strongly influenced by the incoherent scattering, the same should be for the process of radiation emission. This topic will be one of the main subjects of the next Section.

### 5.3 Radiation measurements

In this Section, we report on a study about the radiation generated by 855 MeV electrons through coherent interactions with the quasi-mosaic bent crystal presented in Sec. 5.1. This study allows one to investigate the influence of the crystalline curvature on the radiation emitted by sub-GeV electrons in a bent crystal and thereby the radiation accompanying VR within an unexplored energy range.

In order to measure the radiation spectrum, a calibration of the NaI detector was performed by using the natural radioactive isotopes  $^{40}\text{K}$  (1.461 MeV) and  $^{208}\text{Tl}/^{228}\text{Th}$  (2.6146 MeV) which are impurities in the detector itself and in the surroundings. Fig.

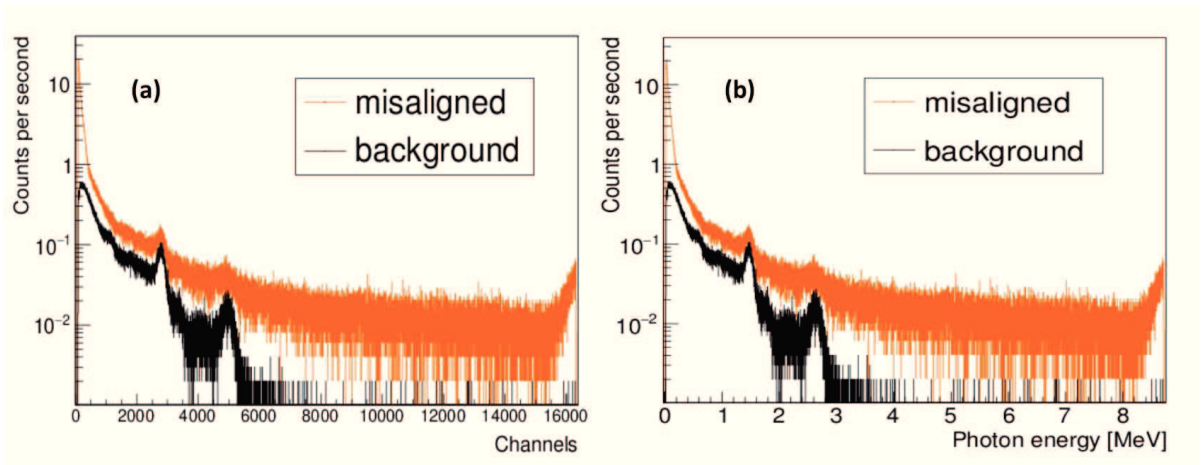


Figure 5.9: NaI row spectra for beam off (black-line) and for 855 MeV electrons (orange-line) in MCA-channels (a) and in photon energy (b).

5.9(a) black-line represents the photon spectrum in counts/sec vs. the MCA units, i.e., the channels of the NaI scintillator, in the case of beam-off. The two more pronounced peaks represent the  $^{40}\text{K}$  and the  $^{208}\text{Tl}/^{228}\text{Th}$  lines. Such peaks have been fitted with a gaussian

distribution to evaluate the mean peak position. The obtained values have been then used to convert the MCA units in energy values,  $E(\text{MeV})$ , by making a linear fit:

$$\frac{E(\text{MeV}) - E_K}{E_{Tl/Th} - E_K} = \frac{MCA - MCA_K}{MCA_{Tl/Th} - MCA_K}, \quad (5.1)$$

being  $MCA_i$  and  $E_i$  the measured and theoretical values for the  $^{40}\text{K}$  and the  $^{208}\text{Tl}/^{228}\text{Th}$  lines. Then, the calibration function is obtained as:

$$E(\text{MeV}) = -0.022401164 + 0.000535418MCA. \quad (5.2)$$

The energy scale of sensibility has been selected in the MeV region interesting for channeling radiation (CR). Fig. 5.9(b) black-line represents the photon spectrum in counts/sec vs. the Photon Energy  $E(\text{MeV})$  after the calibration. The percentage differences between the theoretical and the measured values are 0.068% and 0.057% for the  $^{40}\text{K}$  and the  $^{208}\text{Tl}/^{228}\text{Th}$  lines, respectively.

After the calibration, the electron beam was set at 855 MeV and the emitted photons after interaction with the crystal in random orientation have been collected by the scintillator detector. The resulting photon spectra in MCA (channels) and MeV units are shown in Fig. 5.9(a)-(b) orange-lines, respectively. After the subtraction of the background contribution (black-line), the pure photon spectrum of emitted radiation by electrons inside the crystal is obtained.

The crystal was then rotated around the x axis and, for each angular position (one every 0.003 degrees  $\approx 52\mu\text{rad}$ ), the photon spectrum after interaction with the crystal was recorded. The experimental radiation spectrum after interaction with the crystal as a function of the crystal-to-beam angle is shown in Fig. 5.10(b). The regions (A) and (D) correspond to the nonchanneling case, (B) is for channeling and (C) for VR. For comparison, Fig. 5.10(a) displays the outgoing angle from the crystal as a function of the beam orientation with respect to the (111) planes. A direct comparison between the 2D-distributions of Figs. 5.10 (a) and (b) shows that radiation intensity is stronger than for the misaligned case (regions A and D) within all the angular acceptance of VR (corresponding to region (C)). Nevertheless, the most intense region is represented by channeling radiation (CR) of region (B). As clearly visible by comparing the two plots in Fig. 5.10, it is not possible to separate experimentally the contribution of volume-captured particles in radiation accompanying VR (region (C) in Fig. 5.10(b)) or the contribution of dechanneling in the CR of region (B) in Fig. 5.10(b).

Fig. 5.11 (a) shows the experimental spectra for channeling ( $\alpha$ -curve), VR ( $\beta$ -curve),

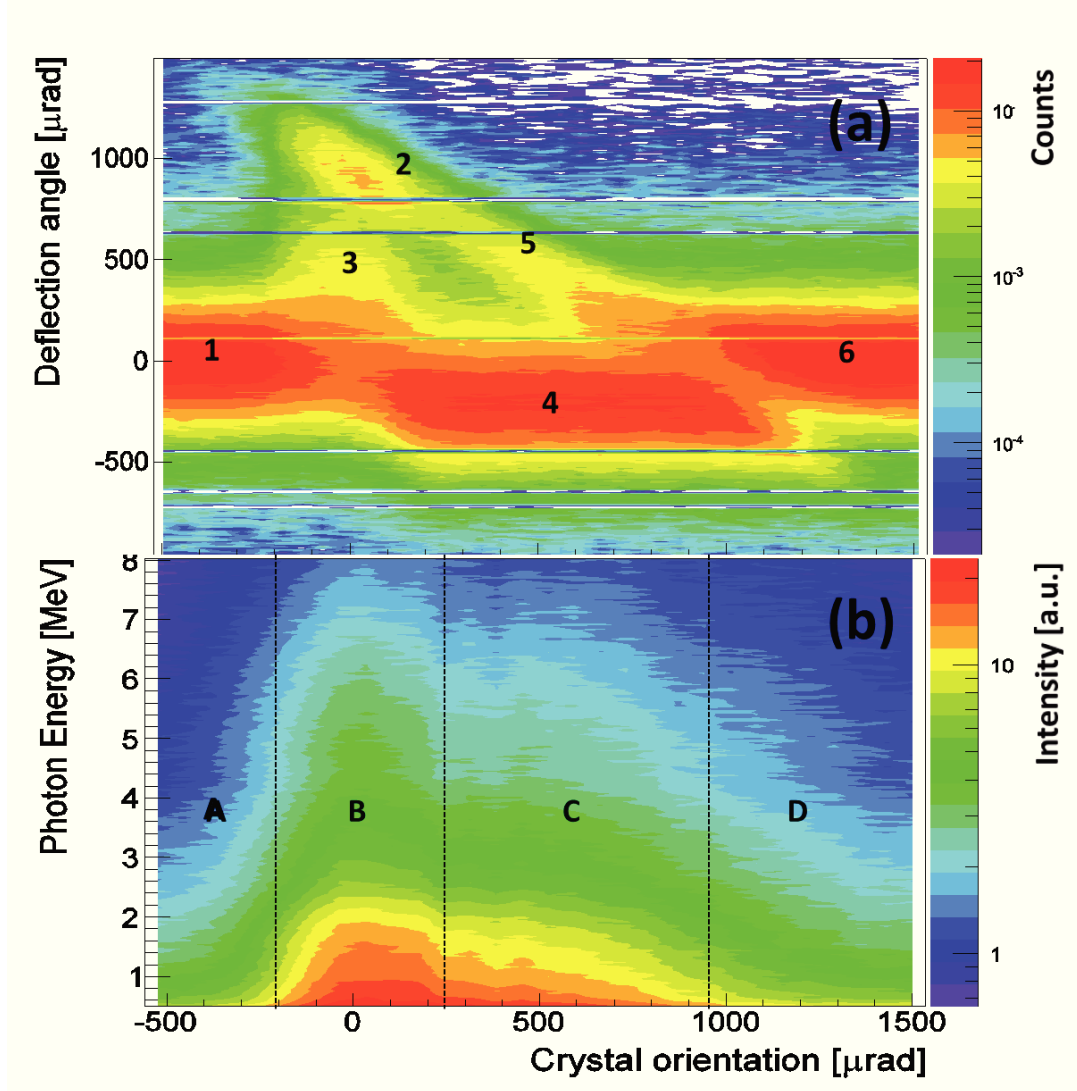


Figure 5.10: (a) Experimental deflected beam distribution vs. the incoming angle with respect to the bent (111) planes. The numbers 1-6 on the figure highlight different regions of interest: (1) and (6) crystal is misaligned, (2) channeling, (3) dechanneling, (4) VR, and (5) volume capture (VC). (b) Experimental radiation spectrum vs. the incoming angle with respect to the bent (111) planes. Regions (A) and (D) correspond to the nonchanneling case, (B) is for channeling and (C) for VR.

at an incidence angle  $\theta_{in}$  equal to 493  $\mu\text{rad}$  from the channeling condition and far from the (111) bent planes, at  $\theta_{in} = 8726 \mu\text{rad}$  ( $\gamma$ -curve). In order to eliminate the fluctuations caused by the too small binning (given by the numbers of NaI channels), a new binning (256) was chosen. The intensities for both CR ( $\alpha$ ) and radiation accompanying VR ( $\beta$ ) are stronger than for the case far from the bent (111) planes ( $\gamma$ ). The experimental spectra

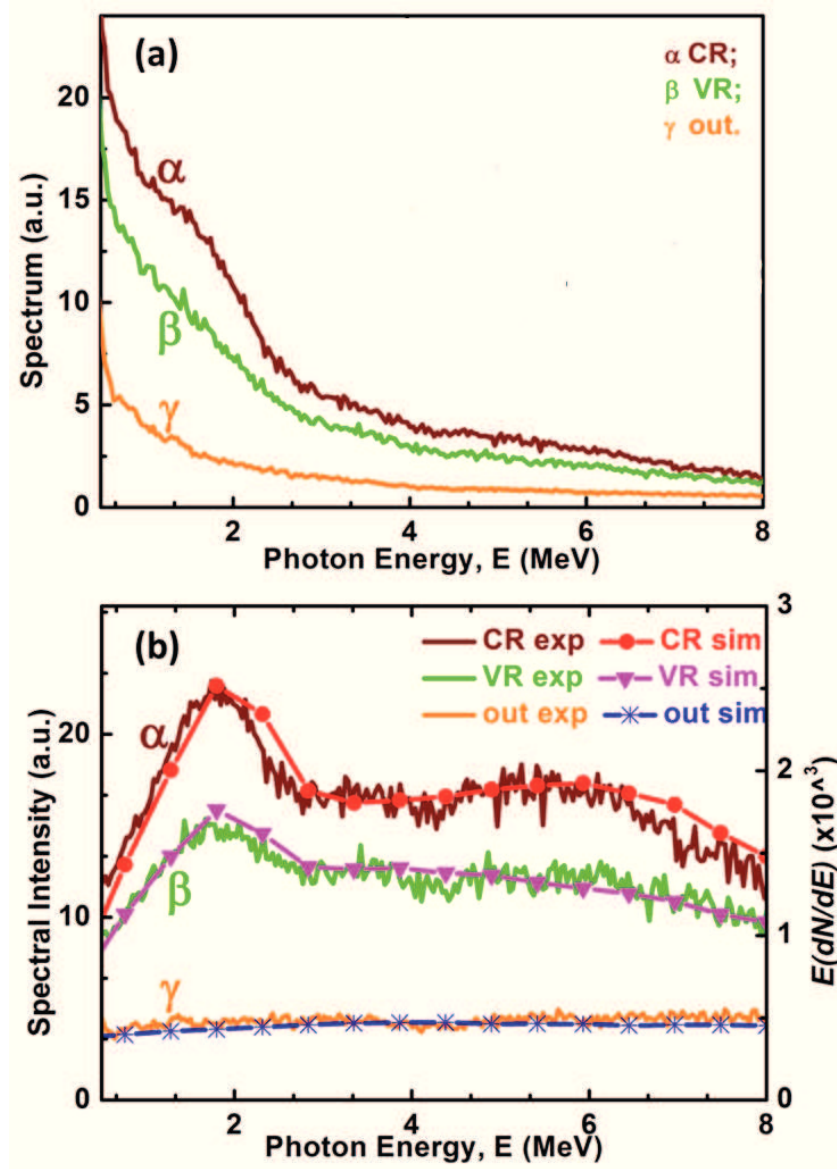


Figure 5.11: (a) The experimental radiation spectra (solid lines) for the cases of channeling ( $\theta_{in} = 0 \mu\text{rad}$ ,  $\alpha$ ), VR ( $\theta_{in} = 493 \mu\text{rad}$ ,  $\beta$ ) and far from (111) bent planes ( $\theta_{in} = 8726 \mu\text{rad}$ ,  $\gamma$ ). The spectra have been taken by subtracting the spectra collected with the beam off (background subtraction). The experimental scale has been chosen from 0.5 MeV to 8 MeV to select the region of interest for CR. (b) Experimental (left-scale) radiation spectral intensities obtained by multiplying the experimental spectra in Fig. 6.11 (a) by the photon energy,  $E$ , for the three cases. The simulated (right-scale) spectral intensity,  $E(dN/dE)$ , has been obtained averaging one thousand of trajectories. Adapted from [A9].

represent the total radiation collected by the NaI detector that is proportional to the number of photons by unit time and energy. In fact, differently from the setup available at

CERN, in which a dedicated trigger system has been constructed, the MAMI setup does not allow for the direct measure of the photons emitted by each electron (see Chapter 4). The depicted spectra are unprocessed, i.e., the deconvolution from the detector response function has not been performed. Nevertheless, the effect of the finite resolution would influence mostly the lower part of the spectra ( $< 0.5$  MeV), far from the CR region.

For the sake of comparison with the spectra normally displayed in the literature, Fig. 5.11 (b) highlights the spectral intensities obtained by multiplying the experimental spectra in Fig. 5.11 (a) by the photon energy,  $E$ . The spectral intensity of CR peaks for photon energies close to 1.8 MeV, which appears also in the case of VR, though less intense.

For the interpretation of experimentally recorded patterns, we performed Monte Carlo simulations with the extension of the DYNECHARM++ code [78] including the routine RADCHARM++ for radiation computation [A8] (see Chapter 3 for details). The simulated spectral intensities  $E(dN/dE)$  vs.  $E$ ,  $dN/dE$  being the photon emission probability, for channeling (circles), VR (down triangles) and misaligned cases (stars), are also displayed in Fig. 5.11 (b), showing a good agreement with experiments both in the shape and amplitude. The difference in the y-scale between experimental and simulated spectra is due to the fact that in the first case the whole radiation collected by the NaI detector is shown, while the latter represents the photon emission probability.

The Monte Carlo code allows one to investigate the influence of the incoherent scattering on the process of photon emission, similarly of what has been done for particle steering. Fig. 5.12 shows the simulated spectral intensity for channeling (circles and squares) and VR (down- and up-triangles) by taking (circles and down-triangles) or not taking (squares and up-triangles) into account the incoherent scattering. For comparison, the simulated incoherent bremsstrahlung (Bethe-Heitler) value is also shown (diamonds) on Fig. 5.12. One can notice that CR is suppressed by the contribution of incoherent scattering. Indeed, incoherent scattering may lead to the dechanneling of the electrons, which causes a strong reduction in the CR intensity. On the contrary, in the case of VR the emitted radiation is intensified by the incoherent scattering, especially in the region of the CR peak. This fact has to be ascribed to the contribution of the volume-captured particles, which undergo a dynamics similar to that of channeled particles after the capture into the channel, resulting in a similar radiation process.

For a quantitative estimation of the contribution of VC in the radiation accompanying VR (Fig. 5.11– $\beta$ ), we checked through the Monte Carlo the value of the particle transverse energy,  $E_T$ , as compared to the potential well depth of bent (111) planes,  $U_0$ :

- if  $E_T < U_0$  at some point during its motion inside the crystal, the particle is labeled

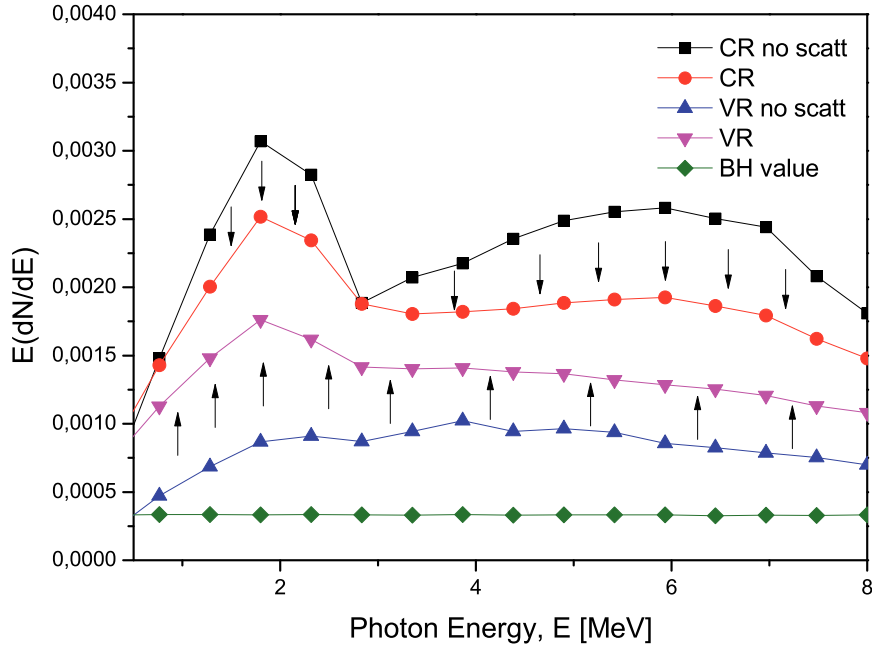


Figure 5.12: Simulated spectral intensity  $E(dN/dE)$  vs. photon energy  $E$  for channeling (circles and squares) and VR (down and up triangles) by taking (circles and down-triangles) or not taking (squares and up-triangles) into account the incoherent scattering. For comparison, the simulated Bethe Heitler value is also shown (diamonds). The arrows directed downwards underline the intensity decrease for CR caused by the incoherent scattering. The arrows directed upwards underline the intensity increase for the radiation accompanying VR due to incoherent scattering. Adapted from [A9].

as **volume-captured**;

- if  $E_T \geq U_0$ , the particle never falls into the channel during its motion inside the crystal and the particle is labeled as pure **volume-reflected**.

Through simulation we found that the first case concerns the 32% of the total number of electrons, while the rest of the beam particles (68%) was purely volume-reflected.

Fig. 5.13 displays the contribution to the radiation accompanying VR (down triangles) of the **volume-captured** (circles) and the purely **volume-reflected** (up triangles) particles. The first case, presented in Fig.5.13 by circles, shows the simulated spectral intensity calculated by averaging over the 32% of VC electrons. One can notice a much more peaked spectral intensity, which is typical for channeled particles, as compared to the case of the total radiation accompanying VR (down triangles). The second case, presented in

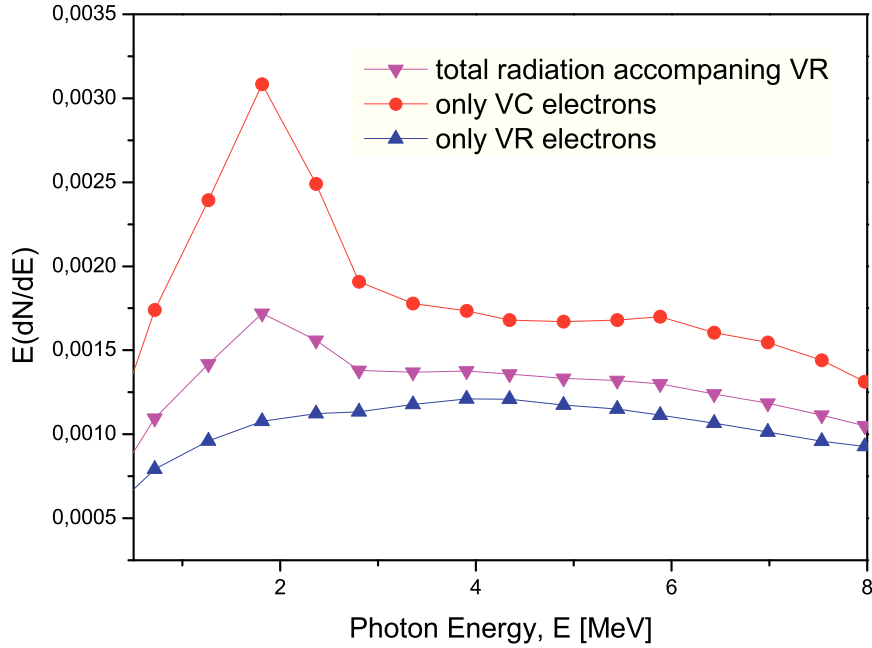


Figure 5.13: The simulated spectral intensity  $E(dN/dE)$  vs. photon energy  $E$  for the radiation accompanying VR (down triangles) and for the contribution of the 32% of VC particles (circles) and of the 68% of VR particles (up triangles). All the simulated spectral intensities are normalized to one electron trajectory. Adapted from [A9].

Fig.5.13 by up-triangles, shows a smeared spectral intensity calculated by averaging over the 68% portion of the total electrons that never fall into the planar well. The absence of sharp peaks in the spectra is ascribed to the change in the angle between particle trajectory and crystal planes, which decreases as the particle approaches the reflection point [20, 22, 66, 70] (see Sec. 2.2.1). The changes in the alignment between particle trajectory and crystal planes result in a smearing of the coherent bremsstrahlung-like (CB) radiation spectrum typical of over barrier particles [20, 22, 70]. In summary, Fig.5.13 highlights the contribution of VC particles, which maintains the electromagnetic radiation accompanying VR close in intensity to that for CR over the whole angular acceptance (see Fig. 5.10(b)). Finally, it is also important to highlight how the changing in the spectral intensities of Fig. 5.12 caused by the incoherent scattering cannot be obtained simply adding the amorphous contribution.

Since many applications in nuclear physics or medicine do require MeV nearly-monochromatic photon beams, we repeated the measurements for CR and radiation accompanying VR with

a smaller collimator aperture (4 mm instead of 40 mm) to reject the contribution of the soft radiation emitted at large angles. The experimental results shows the possibility to pass from the total un-peaked spectra of Fig. 5.11 (a) to the peaked spectra of Fig. 5.14. Both CR and VR radiation peak at  $\sim 2$  MeV, differently from the misaligned case in which the spectrum does not show any peak.

The radiation accompanying VR is comparable in intensity to the radiation in a straight crystal, i.e., it is a sort of intermediate case between CR and CB, however it exhibits a flexibility in its usage as it was shown for the higher energies (see Chapter 4). First of all, the radiation accompanying VR possesses an adjustable and broader angular acceptance, which can be used for high-intensity radiation generation with poor emittance beams. Secondly, VR is less sensitive to crystalline defects as compared to channeling [79], with consequence on the intensity of generated radiation. Such a possibility opens up the way to the usage of higher-Z materials such as W, which usually cannot be grown with the same perfection as a Si crystal, while being more suitable for intense e.m. generation [79, 117]. Finally, differently from CB and CR in a straight crystal, the process of photon generation under VR conditions is accompanied by the process of particle steering, thereby the combination of these two physical effects can be useful in some practical applications. The choice of VR instead of channeling can be preferable for some applications due to its higher efficiency and wider angular acceptance. We also demonstrated that a suitable collimation system it could be possible to increase monochromaticity of emitted radiation, making this kind of radiation interesting for a class of applications in nuclear physics and medicine, for which a nearly monochromatic MeV photon beam is required.

## 5.4 Summary

In summary, the dynamics of sub-GeV electrons in a short and bent (111) oriented Si crystal has been studied at the Mainzer Mikrotron. Planar channeling and volume reflection proved to be effective for efficient steering of the particle beam. It has been shown that rechanneling plays a crucial role in the negative particle dynamics under coherent interactions at such energies. In particular, it has been shown that 55% of the particles recorded under the channeling peak has been rechanneled at least once.

Moreover, it was demonstrated the possibility to exploit bent crystals in the sub-GeV energy range to generate hard and intense electromagnetic radiation. It has also been demonstrated that CR and the radiation accompanying VR are much more intense than for an amorphous material. In particular, it was shown how the radiation accompanying

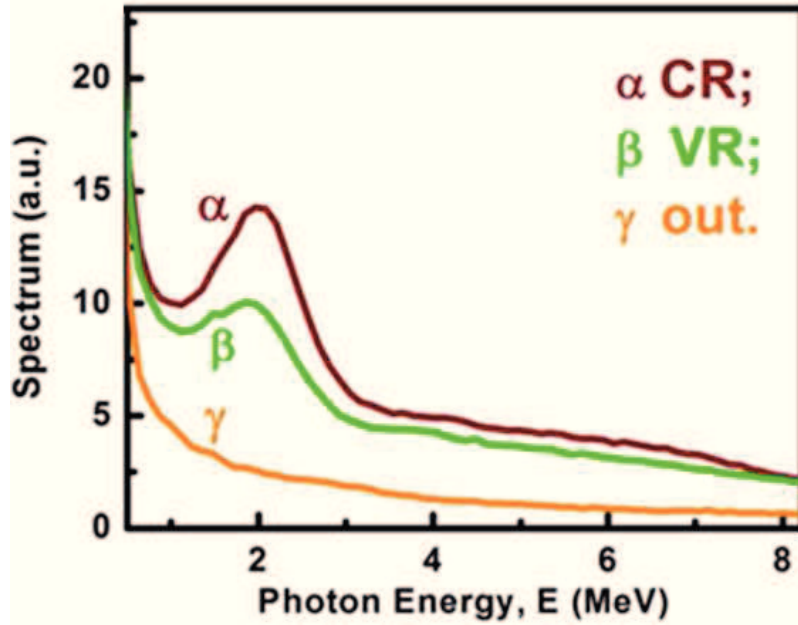


Figure 5.14: Experimental spectra for the case of a 4mm aperture.  $\alpha$ -line for channeling,  $\beta$ -line for VR ( $\theta_{in} = 493 \mu\text{rad}$ ) and  $\gamma$ -line for the misaligned case. Adapted from [A9].

VR naturally combines the radiation emitted by pure volume-reflected particles with that emitted as a result of VC. The contribution of VC radiation renders the radiation accompanying VR similar to that for CR in intensity, but its angular acceptance is wider than for channeling.

All these information together could be taken into account to simulate and design periodically bent crystals, i.e., crystalline undulators (see [23] and references therein), as innovative sources of high-intensity electromagnetic radiation. Furthermore, the combination of these features provides interesting prospects for applications of the e.m. radiation generated in bent crystals in an energy range available by many electron accelerators worldwide.



# Chapter 6

## Recent studies on coherent interactions of 400 GeV/c protons with innovative crystals

This Chapter will go beyond the study of emitted radiation by high energy electrons in bent crystals, describing some interesting results achieved with 400 GeV/c protons, available the external line H8 of CERN-SPS, interacting with two innovative crystals, i.e., a **periodically bent crystal** and a **crystal mirror**. Sec. 6.1 describes the realization of a periodically bent crystal via the superficial groovings method, to be used as a crystalline undulator. The sample was then tested vs. 400 GeV/c proton beam to demonstrate the feasibility of such a method. Sec. 6.2 describes the realization and the experimental test of ultra-thin straight crystal, to be used as a *crystal mirror* for positively charged beam steering.

### 6.1 Characterization of a crystalline undulator with 400 GeV/c protons

#### 6.1.1 Why a crystalline undulator?

High-intensity and monochromatic X- and  $\gamma$ -rays are very desirable for a great amount of applications, ranging from fundamental to applied science. Free-electron lasers (FELs) are usually adopted to generate intense and monochromatic photon beams.

FELs are based on magnetic undulators [118, 119], which force electrons to an oscillatory

motion. As a consequence, electromagnetic radiation is produced. The condition

$$K = \frac{eF\lambda_u}{2\pi mc} \sim 1 \quad (6.1)$$

lead to a high intensity and nearly monochromatic spectrum for the undulator radiation [120, 121]. In eq. 6.1,  $K$  is the undulator parameter,  $e$  and  $m$  the electron charge and mass,  $F$  the magnetic field amplitude, and  $\lambda_u$  the undulator period. The minimum achievable  $\lambda_u$  with the currently available magnetic undulators is of the order of some centimeters, allowing to generate X-ray with energy

$$\hbar\omega = \frac{4\pi\gamma^2}{\lambda_u(1+K^2)} \quad (6.2)$$

with  $\gamma$  being the Lorentz factor. At the highest synchrotron electron energies, eq.6.2 reaches a few tens of keV [122]. For a class of applications, such as photo-transmutation [123] or photo-induced nuclear fission [124], much higher photon energies are needed and thereby much shorter undulator periods are required. Indeed, since the usage of current tools adds constraint to the minimum oscillation period, it would be very difficult or even impossible to generate photon with higher energies with such technique. First efforts to decrease undulator periods down to 1mm date back to the mid 80s [125–130].

The usage of a crystalline undulator (CU) has been identified as a promising technique to overcome the limit of achievable energy by a FEL. The main idea of the CU is to impress an oscillatory motion to a bunch of particles exploiting the strong interplanar field generated by ordered atoms within an oriented crystal [1]. In other word, one could replace the magnetic undulator in a FEL with a crystal.

When an electron/positron enters an oriented crystal with a small angle with respect to the major crystallographic planes or axes, the strong electrostatic fields between crystal planes or axes confines the particle trajectories. The channeled particles are subjected to a field of 6GV/cm for (110) Si plane, that is equivalent to a 2 kT magnetic field. The motion of the channeled  $e^\pm$  is accompanied by fast transverse oscillations. Such a motion is accompanied by the hard and quite smooth channeling radiation. If the crystal planes are periodically bent with an oscillation period  $\lambda_u$ , exceeding those of channeled particles ( $\lambda_u > \lambda_c$ ), the motion of such particles will resemble the one achievable in a magnetic undulator with the same  $\lambda_u$ .

To be more general, CU radiation can be distinguished from the channeling radiation only if  $\lambda_u$  is not equal to the average channeling oscillation period  $\lambda_c$ . Traditional CU-scheme works under the condition  $\lambda_u > \lambda_c$  [67], though an alternative scheme with  $\lambda_u < \lambda_c$

was recently proposed [131]. Fig. 6.1 is a schematic representation of a CU [132]. A positron and an electron trajectories are depicted.

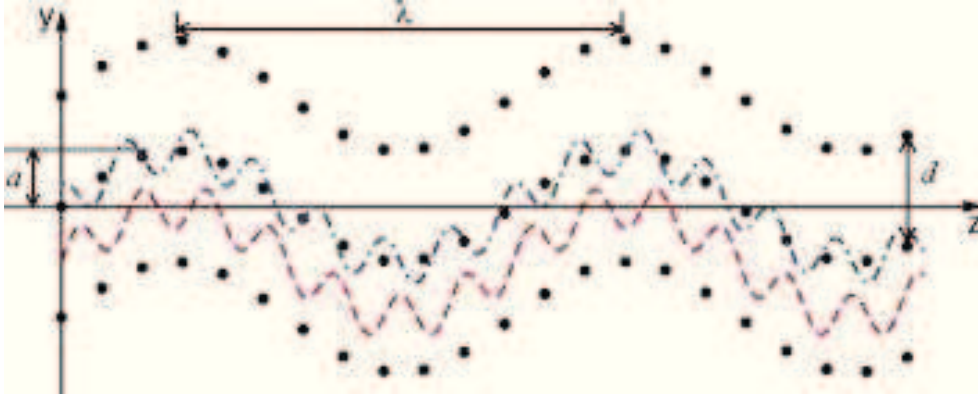


Figure 6.1: Schematic representation of a CU for the case  $\lambda_u > \lambda_c$ . A positron and an electron trajectories are depicted. Picture adapted from [132].

### 6.1.2 Fabrication and Interferometric Characterization of a periodically bent crystal

The key point for the realization of a working CU does require both an high-accuracy in the deformation of the crystallographic planes and a low-level of induced defects. Different methods have been proposed for the realization of a periodically bent crystal, such as acoustic wave transmission [133], periodically graded  $Si_{1-x}Ge_x$  structures [134], and periodic surface deformations obtainable via superficial grooves [135, 136], laser ablation [137], or film deposition [138, 139]. Up to now different experiments have been done to demonstrate the feasibility of a working CU [135, 140–145], and some theoretical work has been accomplished to foresee the energy response of a CU interacting with a positrons or electrons beam [146]. However, either the low quality of the beams or the not perfect structure of the CUs have limited or even inhibited the performances of the realized CUs. Only very recently, a first evidence of the radiation generated by sub-GeV electrons interacting with a CU having  $\lambda_u < \lambda_c$  was observed in the 7-15 MeV range, using a 600-855 MeV electron beam available at MAMI B[147].

The simplicity and reproducibility of the superficial grooving method makes it particularly suitable for the purpose of realizing a working CU. Indeed in the last years, in the framework of the LAUE project, the method of superficial grooving [135, 140] has been deeply investigated and implemented to produce bent crystals tailored for the realization

of optics for hard X-rays (e.g. Laue lens) [148, 149]. The method consists in the manufacture of a series of grooves on the major surfaces of a crystal. It was shown that series of grooves may cause a permanent and reproducible deformation of the whole sample [150]. Indeed, the plasticization that occurs in the thin superficial layer is able to transfer coactive forces to the crystal bulk, producing an elastic strain field within the crystal itself (see Fig. 6.2(a)). An alternated pattern of parallel indentations performed on both surfaces of a crystal could lead to the realization of a millimetric or even a sub-millimetric undulator as shown schematically in Fig. 6.2(b).

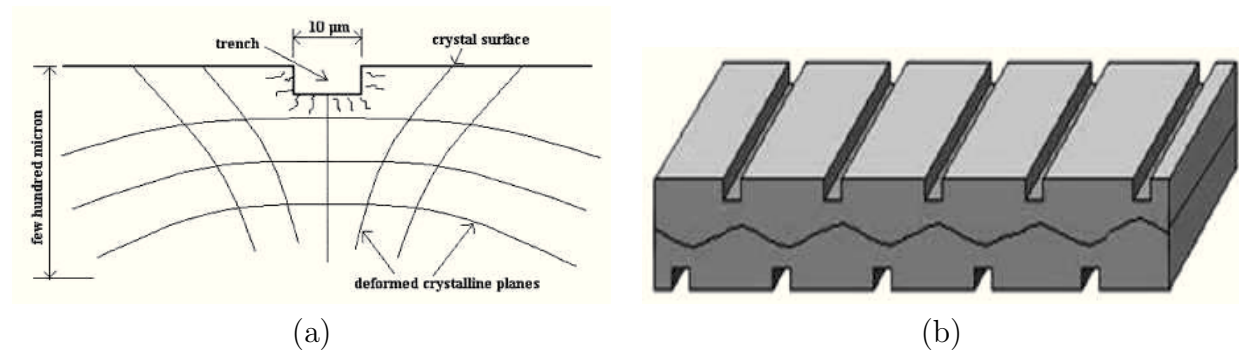


Figure 6.2: (a) Schematic representation of a superficial groove. Plasticization of the surface of the plates proved to induce a net and uniform curvature within a crystal which resulted in a wavy profile that propagates deep into the bulk. (b) Schematic representation of a crystallographic undulator obtained through the grooving method.

In the case of the superficial grooving method, it is possible to realize CU within the traditional scheme,  $\lambda_u > \lambda_c$ . A larger period means a larger bending of the particle beams, resulting in a weaker effective field ( $F$ ) for the particle motion in the periodically bent crystal as compared to the maximum planar field.

A CU was realized at the Sensor and Semiconductor Lab of Ferrara University by manufacturing a series of grooves on a  $0.2 \times 45.0 \times 5.0$  mm<sup>3</sup> silicon crystal. In particular, an alternating and periodic pattern of parallel grooves 150 μm wide was performed on the largest surfaces of the strip, with the distance between consecutive grooves being 1 mm. The grooves were manufactured by means of a diamond blade through the usage of a DISCO DAD 3220 dicing machine. The groove depth was  $(54 \pm 2)$  μm. A schematic representation of the sample is reported in Fig.6.3 and the fabrication parameters are listed in Tab. 6.1.

A morphological analysis of the sample surface was attained through a VEECO NT-1100 white-light interferometer, which allowed the reconstruction of the three-dimensional surfaces with lateral resolution of about 1 μm and vertical resolution of 1 nm. The pro-

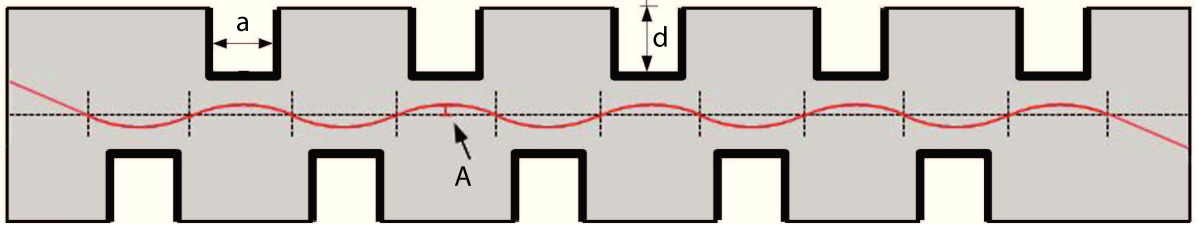


Figure 6.3: Schematic representation of the crystallographic undulator obtained through the grooving method. The red line represents the undulated planes on the center of the crystal.  $A$  is the amplitude of the undulated planes,  $a= 150 \mu\text{m}$  the groove width and  $d = 54 \mu\text{m}$  the groove depth. Adapted from [A7].

Table 6.1: Fabrication parameters

Material	Silicon
Sample size ( $\text{mm}^2$ )	$45.0 \times 5.0$
Sample thickness (mm)	0.2
Blade width ( $\mu\text{m}$ )	150
Blade rotation (rpm)	40000
Blade speed (mm/s)	1
Groove depth ( $\mu\text{m}$ )	54
Number of grooves per surface	5
Groove step (mm)	1

filometric pattern of one of the sample surface is shown in Fig. 6.4. A periodical series of curvatures are clearly visible between the grooves. These curvatures are caused by the grooves on the opposite surface of the sample. As a result, it was possible to estimate the amplitude of the crystallographic planes undulation. The averaged value of the undulating amplitude resulted to be  $4.5 \pm 1.0 \text{ nm}$ . Since the interferometric analysis gives information just on the surface shape of the sample, it does not allow collecting any information on the undulator structure inside the crystal bulk.

### 6.1.3 Experiment with high-energy protons

With the aim of investigating the undulator structure of the sample, the CU crystal was mounted on an high-resolution goniometer (see Sec. 4.1) and exposed to the 400 GeV/c proton beam of the H8 beam line at CERN-SPS. The Lindhard angle at such energy is  $\theta_c = \sqrt{\frac{2U_0}{400\text{GeV}}} \approx 11\mu\text{rad}$ , being  $U_0 \sim 25 \text{ eV}$  for (111) planes. The beam was tracked before and after interaction with the crystal by a tracking system of Si double-sided microstrip

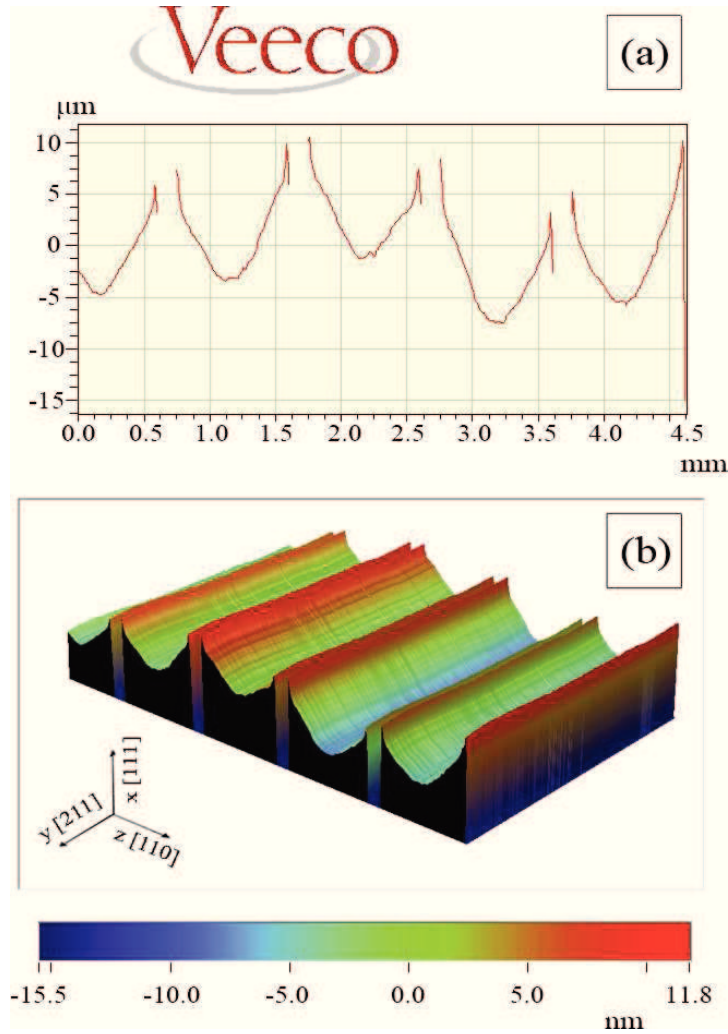


Figure 6.4: Interferometric measurement of the sample. (a) 2d view analysis as taken at the center of the sample along  $x$  axis. (b): 3d view analysis.

detectors [151]. The experimental setup on H8 is similar to the part A of the setup used before in H4 beamline (see Chapter 4). The main difference is in the arrangement of the three double sided Si microstrip detectors ( $SD_i$ ) as shown in Fig. 6.5. The angular resolution of the telescope system is  $\sim 3.5 \mu\text{rad}$ . Beam size  $(1.36 \pm 0.02) \text{ mm} \times (0.73 \pm 0.01) \text{ mm}$  and angular divergence  $(10.15 \pm 0.04) \mu\text{rad} \times (8.00 \pm 0.03) \mu\text{rad}$  were measured with the telescope system.

The vertical axis of the CU was purposely misaligned with respect to the beam direction to avoid axial channeling. The  $0.2 \times 45.0 \text{ mm}^2$  face was (110) oriented. The (111) planes were exploited as channeling planes. A geometrical cut has been implemented during

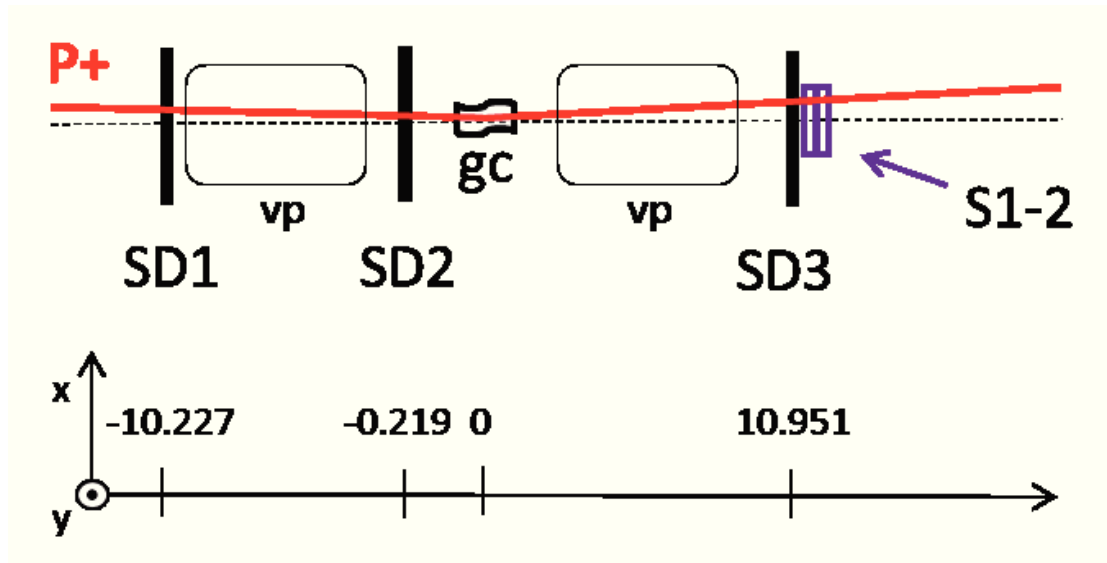


Figure 6.5: Scheme of the experimental setup on the H8 beamline at CERN SPS. It consists of a telescope system composed by 3 silicon modules (SDi) separated by vacuum pipes (vp) and the high precision goniometer on which has been installed the CU sample (gc). Two scintillator S1-2 are mounted on SD3 and are used for the trigger system. The distances are in  $m$ .

data analysis with the aim of avoiding the surface scratches. A range of  $35 \mu m$  in the horizontal coordinate at the center of the sample has been selected during the off-line analysis, leading to the study of the sample region in which the oscillatory structure of the crystal should manifest. The distribution of the particle deflection angle in the horizontal direction as a function of the horizontal incoming angle was measured by rotating the goniometer around the (111) planes (see Fig. 6.6). Since the proton beam has a non-zero divergence, the horizontal incoming angle was determined as the sum of the angle measured by the goniometer and the incoming angle of the beam particle as measured by SD1-2. The distribution represented in Fig. 6.6 exhibits a two-fold pattern. Indeed, channeled particles can dechannel at various penetration depths of the CU. As a consequence, particles acquire a positive or negative deflection angle. By comparing Fig. 6.6 with Si (111) angular scan in a bent crystal from literature (see Fig. 5.5 as an example), a noticeable difference stood. In fact, the two fold pattern cannot be observed for a uniformly bent crystal, because only one curvature is present.

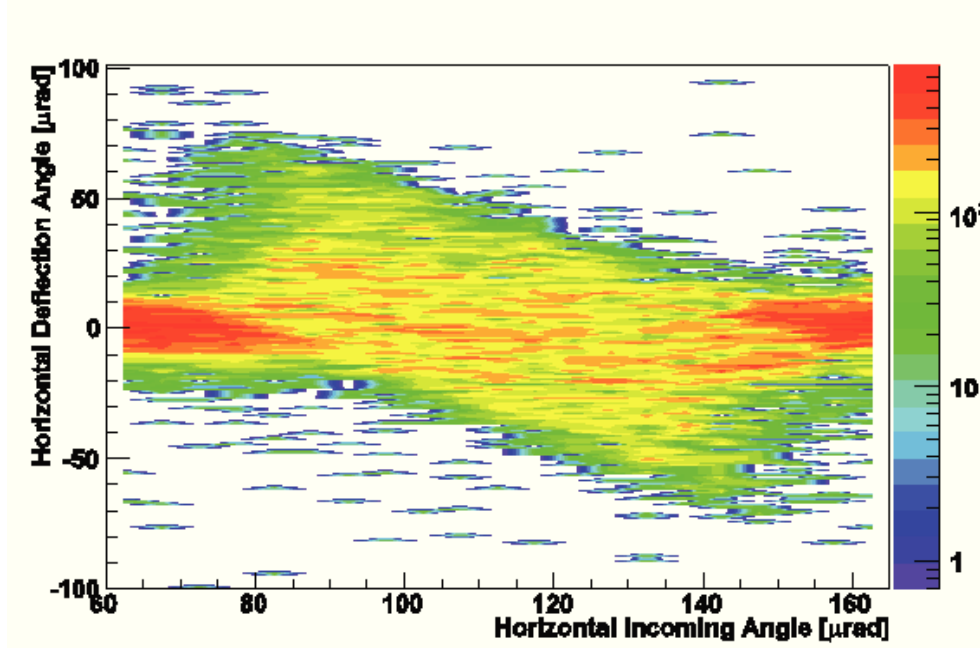
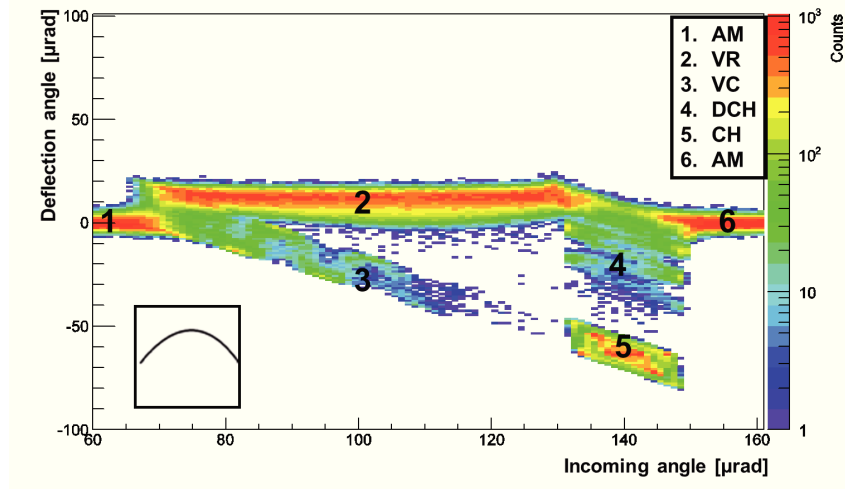


Figure 6.6: Experimental deflection angle vs. the incoming angle of particle with respect to the crystal (111) planes. The two-fold pattern is the mark of the undulating structure.

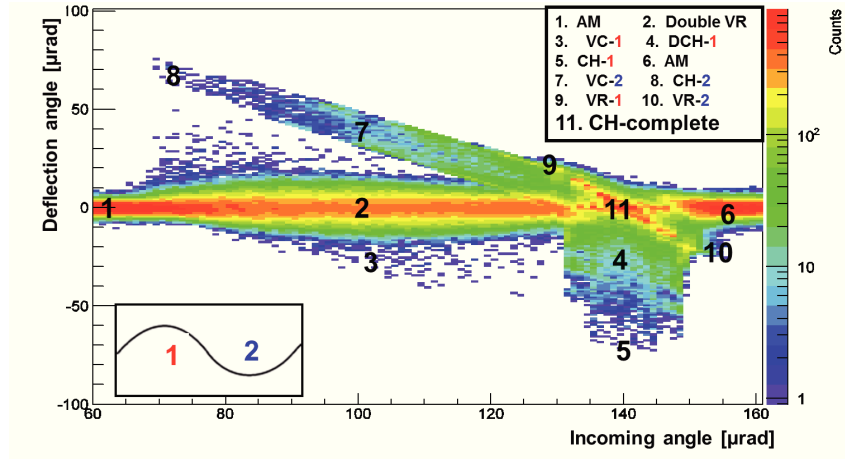
#### 6.1.4 Monte Carlo simulations

In order to get an insight into the experimental result, a Monte Carlo simulation was performed by using the DYNECHARM++ code [78]. The CU geometry was approximated through a sinusoidal function with the measured amplitude, obtained through the interferometric measurement, and oscillation period being equal to the distance between the grooves. The influence of such geometry on particle trajectory was evaluated through the application of a position-dependent centrifugal force. Intensity of scattering on nuclei and electrons was averaged over the distribution density in the channel in order to reliably estimate the dechanneling probability.

With the aim of a better understanding of the protons dynamics inside the CU sample, simulated particles were tracked along all the crystal length. Fig. 6.7(a) shows the distribution of horizontal deflection angle as a function of the horizontal incoming angle at an half of the CU oscillation period  $\lambda_u$ . The clear typical markers of a bent crystal are present, i.e., channeling spot and volume reflected particles. In fact, channeled particles are distinguishable because of they received the largest deflection kick (region 5). On the other side, particles which impact on the target tangent to the crystalline curved planes are deflected to the opposite direction, i.e., they undergo volume reflection (region 2). The regions 3 and



(a)



(b)

Figure 6.7: (a) Simulated deflection distribution vs. incoming angle after half of an oscillatory period,  $\frac{\lambda_u}{2}$ . (b) Simulated deflection distribution vs. incoming angle after one oscillatory period,  $\lambda_u$ .

4 represent the volume capture and the dechanneling zones, respectively. In regions 1 and 6, the proton beam is misaligned with respect to the (111) planes. After an entire period  $\lambda_u$  (Fig.6.7(b)) the general picture evolves towards a double fold distribution. Indeed, the particles that did not suffer dechanneling are still trapped into the crystalline potential well and acquire an overall zero deflection angle (region 11). The dechanneled particles are distributed in regions 4. Volume reflected particles bounce against the potential wall of the second half-period with inverted bending radius and either acquire a net zero deflection angle (region 2), either are captured into the channeling state (region 7).

The simulated pattern of the beam interacting with the whole CU is shown in Fig.

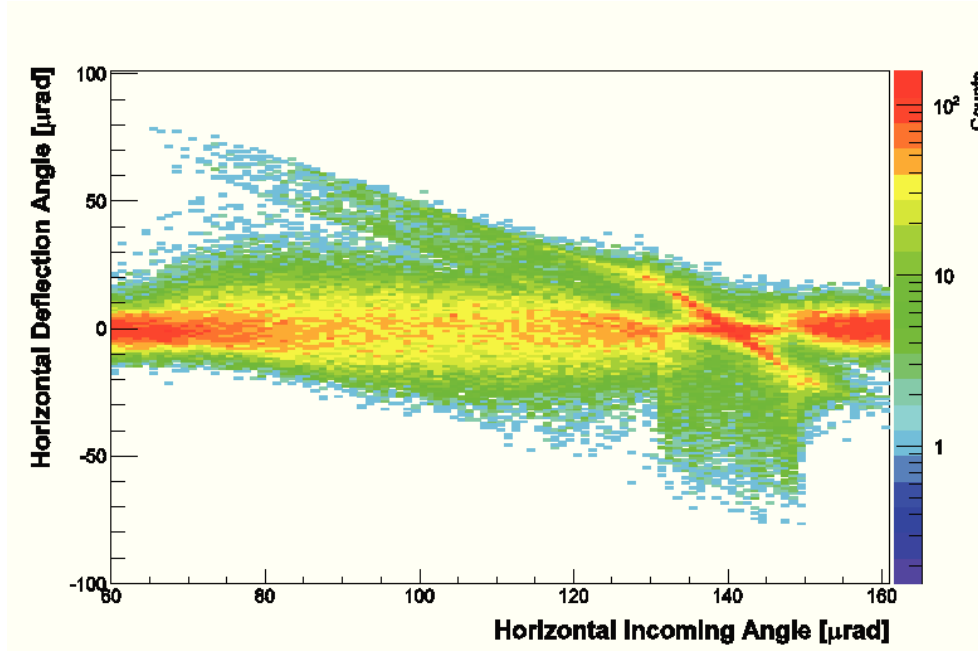


Figure 6.8: Simulated deflection distribution vs. the incoming angle of particle with respect to the crystal planes after the total CU length. The two-fold pattern is the mark of the undulating structure.

6.8. The comparison between patterns in Figs. 6.6 and 6.8 highlights an agreement in shape. Indeed, the two fold structure is identifiable in both distributions. Particles under channeling along all the crystal length exit with an overall zero deflection angle. On the contrary, the particles deflected at positive and negative angles were dechanneled because of the change of the centrifugal force direction in the crystal. The angular spread of reflected particles increases with the increase of the quantity of material traversed and the consequent more frequent incoherent scattering with nuclei and electrons during the motion. The difference between the distributions Figs. 6.6 and 6.8 could be ascribed to the poor statistics of the experimental results and to the non-perfect determination of the CU amplitude achievable through an interferometric method. After the preliminary analysis presented in this work of thesis, a campaign of measurements was conducted at the ESRF by using hard X-ray diffraction with the aim of analyzing how the oscillatory structure propagates within the CU sample. Such results and new Monte Carlo simulations based on new informations of the CU structure are published in [A7].

In the next future, a positron beam with energy in the range of 10-20 GeV will be available at FACET-SLAC, being a perfect facility for the test of the CU sample. Indeed, the choice of the CU sample parameters well fit with the condition of eq. 6.1 for an

optimal undulator in the case of FACET positrons. Indeed, the equation 6.1 represents the equality between the maximum deflection angle of the particles inside the undulator,  $\theta_u$ , and the characteristic angle of the forward radiation emitted by relativistic particles in an accelerated motion,  $1/\gamma$ . Since in our case it is  $\theta_u \approx 50\mu\text{rad}$ , the beam energy has to be  $E \sim mc^2/\theta_u \sim 10 \text{ GeV}$  to comply the condition of eq. 6.1. Moreover, in this energy range the possibility to use an electron beam for the CU test has to be excluded because the electron dechanneling length is much smaller than the CU length. Thereby, only positrons can be used for such a test, allowing for the production of photons with energy in the subMeV-MeV range.

### 6.1.5 Summarizing

A crystalline undulator was manufactured through the superficial grooving method. The morphological surfaces of the sample were analyzed through an interferometric analysis at SSL (Ferrara, It). Then, the crystal was tested at the H8 line of the CERN-SPS. Coherent interactions between of 400 GeV/c protons with the sample were observed. The experimental pattern was reproduced through Monte Carlo simulations with the DYNECHARM++ toolkit. Finally, the fabrication parameters of the CU sample are in the optimal range for a 10-20 GeV positron-based CU.

## 6.2 Mirroring of 400 GeV/c protons by a ultra-thin straight crystal

In this section, a study of the *mirror effect* for ultrarelativistic positive particles performed at external lines of CERN-SPS by using 400 GeV/c protons is presented.

### 6.2.1 A crystal *mirror*

A series of experiments done at CERN SPS demonstrated that a mm-long bent crystal can efficiently deflect 400 GeV/c protons with a strength comparable to a magnetic dipole of hundreds of Tesla with the same length [51, 152, 153]. A possible application of channeling in a bent crystal is halo-beam collimation of very-high energy beams of modern hadron colliders [17]. The UA9 experiment, which is devoted to the study and the realization of a crystal-assisted collimation system for the Super Proton Synchrotron (SPS) and the Large Hadron Collider (LHC), demonstrated that crystal collimation is a viable way to reduce the beam losses in the SPS circular accelerator [154].

In 1995, Tsyganov and Taratin suggested that also a straight crystal can be used for particle deflection for positively charge particles [24]. In fact, the transverse motion of a positive particle under the planar channeling regime is governed by a potential that can be well described by the harmonic approximation,  $\sim x^2$ , where  $x$  is the distance from the potential minimum (see Sec. 1.1.2) [42]. For this reason, planar channeled particles oscillate during their motion with a characteristic oscillation length,  $\lambda = \pi d_p / \theta_c$ ,  $d_p$  being the interplanar distance. If a crystal is as thick as  $\lambda/2$ , a positive particle incident onto the crystal with an angle in the range  $[-\theta_c, +\theta_c]$ , would reverse its transverse momentum after half of its period, resulting in "mirroring" of its trajectories [24].

Despite the effect of particle mirroring was theorized in the 90s, only recently was proven to work [155] at the non-relativistic energies. In [155] it was demonstrated the possibility to *reflect* non-relativistic protons of 2 MeV kinetic energy, while the most appealing applications concerning crystal-assisted manipulation of beam trajectories are those at ultrarelativistic energies, where an inexpensive and passive crystal would do the same job as a cumbersome superconducting magnet.

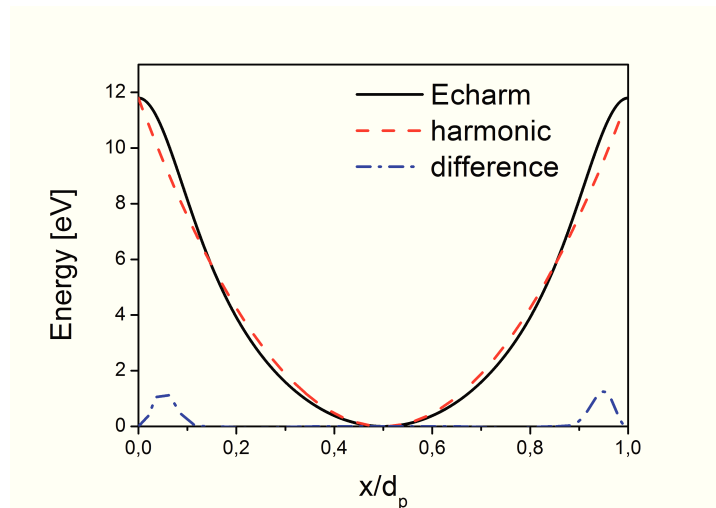


Figure 6.9: Transverse potential energy between two (100) plane as calculated by using form factors experimental data (solid line) and in harmonic approximation (dashed line). The difference between these two model is also shown (dot-dashed line), highlighting the not-validity of harmonic approximation close to atomic planes.

Before undertaking experimental work, a study aimed to design the crystal with the correct size for mirroring 400 GeV/c protons was done. The Monte Carlo code DYNECHARM++ [78] was used to study particles trajectories and transverse momentum evolution of 400 GeV/c protons interacting with (100) planes of a Si crystal. The maximum of the (100)

potential well and the Lindhard angle estimated through the ECHARM code [82] are  $\approx 11.8$  eV and  $\approx 7.6$   $\mu\text{rad}$ , respectively. Under the harmonic approximation,  $\lambda$  would be 57  $\mu\text{m}$ . In fact, the planar potential well  $U(x)$  is not perfectly harmonic, especially close to planes in the region of high nuclear density (see Fig. 6.9). Fig. 6.10(a) shows some trajectories of 400 GeV/c protons in a 100  $\mu\text{m}$  thick Si crystal aligned along the (100) planes at the entry face of the crystal. Since  $U(x)$  is not perfectly harmonic, the trajectories are not characterized by a single oscillation length  $\lambda$ , but by a set of  $\lambda$ s lying between 50  $\mu\text{m}$  and 61  $\mu\text{m}$ . The value of  $\lambda$  for each particle depends on its impact parameter with the atomic planes. From Fig. 6.10(a) one may also notice that the imperfection in the harmonic approximation of  $U(x)$  weakly affects the first half-oscillation length, while it plays significant role after few oscillations.

### 6.2.2 *Crystal mirror* fabrication and characterization at the Sensor and Semiconductor Lab of Ferrara University

A (100) oriented Si wafer was machined via anisotropic etching [88] in order to obtain a Si crystal with lateral sizes of  $4 \times 4$   $\text{mm}^2$  (see Fig. 6.11(a)). All the wafer surfaces were coated with 100 nm silicon nitride layer deposited through low-pressure chemical vapour deposition. Such layer was then patterned through photolithography techniques to remove the coated film from selected areas. With such technique, one can obtain a very thin silicon membrane surrounded by a bulky frame of 500  $\mu\text{m}$  in order to assure easy handling and to prevent deformations of the crystal when it is mounted on a goniometer. The wafer was immersed in a basic solution of KOH, resulting in thinning of the uncoated areas. A precise calibration of the silicon etching rate allowed stopping the thinning process once an ultra-thin silicon membrane with the desired thickness was left. Fig. 6.11(b) shows a picture of the manufactured Si membrane.

The thickness of the crystal was characterized with infrared interferometry (Fogale T-MAP) and was found to be  $(26.5 \pm 0.1)$   $\mu\text{m}$ . This value lies within the range of values for  $\lambda/2$  foreseen for (001) Si planes used to deflect the particles as a crystal mirror (see Fig. 6.11(c)).

With the aim of testing the capability of the 26.5  $\mu\text{m}$  Si crystal as a mirror, a simulation of interactions of 400 GeV/c protons with the crystal has been carried out. Fig. 6.10(b) shows the outcomes of the simulation, in particular some trajectories of 400 GeV/c protons in the crystal tilted by 4  $\mu\text{rad}$ ,  $\sim \theta_c/2$ , with respect to the perfect alignment of (001) planes with the beam, are displayed. The choice of  $\theta_c/2$  for the tilt angle was suggested in [24] as a trade-off between large deflection efficiency (more than 50% for small beam divergence)

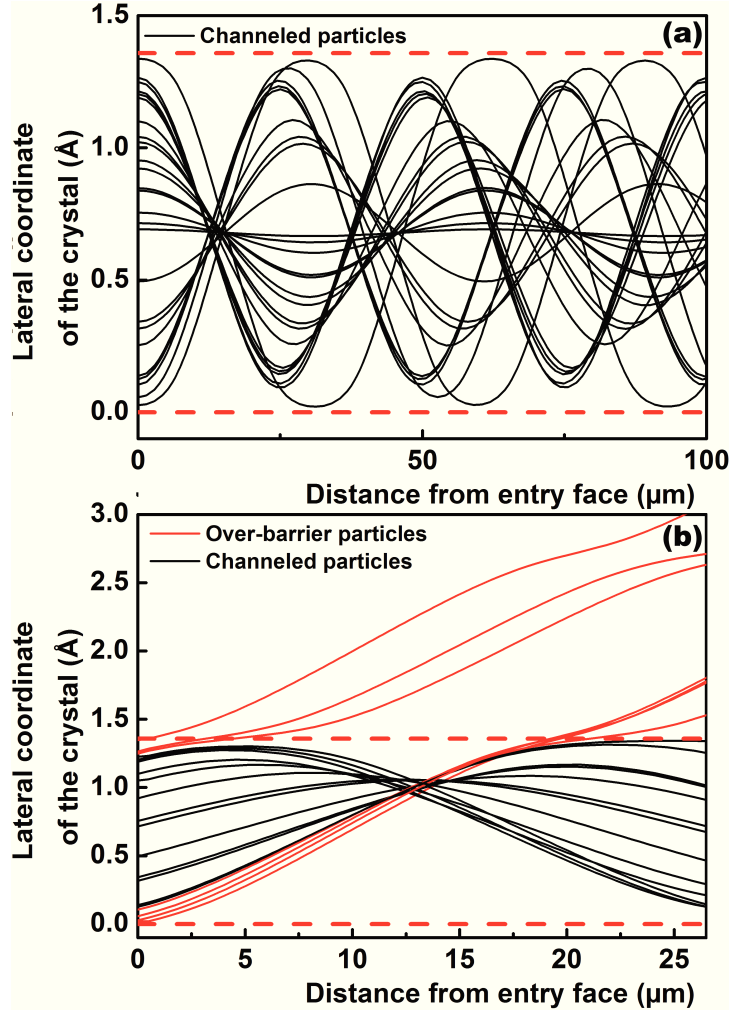


Figure 6.10: (a) A graphic representation of a few trajectories of 400 GeV/c protons in a 100  $\mu\text{m}$  Si crystal. At the entry face of the crystal the particle momenta are parallel to the (100) planes. Due to the not harmonicity of the planar potential, each trajectory is characterized by an oscillation length  $\lambda$  that depends on the impact parameter at the entry face of the crystal. (b) A few trajectories of 400 GeV/c protons in the 26.5  $\mu\text{m}$  thin crystal tilted by 4  $\mu\text{rad} \sim \theta_c/2$  with respect to the beam-to-crystal perfect alignment. Most of the particles are captured under planar channeling regime (black trajectories). Trajectories in red pertain to the particles that are in over-barrier states at their entrance in the crystal. In order to highlight the coherent part of interaction between particles and the crystals, the simulation for (a) and (b) were performed without the contribution of incoherent scattering on nuclei and electrons. Adapted from [A6].

and large deflection angle. Indeed, one may notice that most of the particles are captured under planar channeling regime (black trajectories) and then reflected by an angle twice

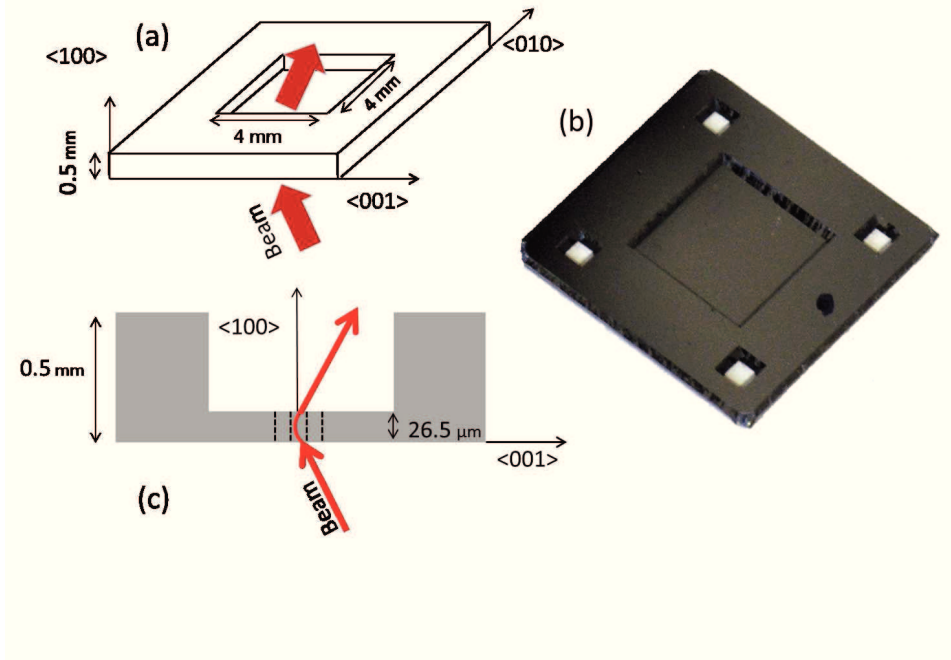


Figure 6.11: (a) Sketch of the ultra-thin Si crystal that highlights the crystallographic orientations; the arrows indicate the direction of the proton beam, which impinges on an active area  $4 \times 4 \text{ mm}^2$  large and  $26.5 \mu\text{m}$  thick, surrounded by a  $500 \mu\text{m}$  thick frame. (b) Picture of the thin Si crystal. (c) Lateral view of the crystal, with crystallographic orientation highlighted; red arrows represent the incidence and outgoing direction of particle beam mirrored by the Si (001) crystal planes. Adapted from [A6].

that of incidence. Trajectories in red pertain to the particles in over-barrier states at the entry face of the crystal. At the exit face, most of over-barrier particles acquire a non-zero component of transverse momentum and are deflected in a direction opposite to that of the channeled ones. The expected angular distribution of the beam after interaction with the crystal is shown in Fig. 6.12 solid line. One can notice two sharp peaks; the more intense peak on the right corresponds to the mirrored-channeled particles; the smaller one on the left corresponds to deflection of above-barrier particles in an opposite direction with respect to channeled ones. A two-Gaussian fit provided the positions of the peaks, resulting in about  $7.9 \mu\text{rad}$  and  $-5 \mu\text{rad}$ , respectively. The right peak is two times the incidence angle, i.e., deflection takes place according to mirror effect. The percentage of particles deflected with an angle larger than zero is about the 84%. For comparison, Fig. 6.12 displays also the deflection distribution of for incidence angles  $\theta_{in} \approx \theta_c$  (dashed line) and for  $\theta_{in} = 0$  (dot-dashed). In the first case, even if the angle of mirroring is the largest achievable, most of the particles found in over-barrier states and are not deflected. While in the case of

perfect alignment with crystal planes, the protons do not suffer a mirroring process.

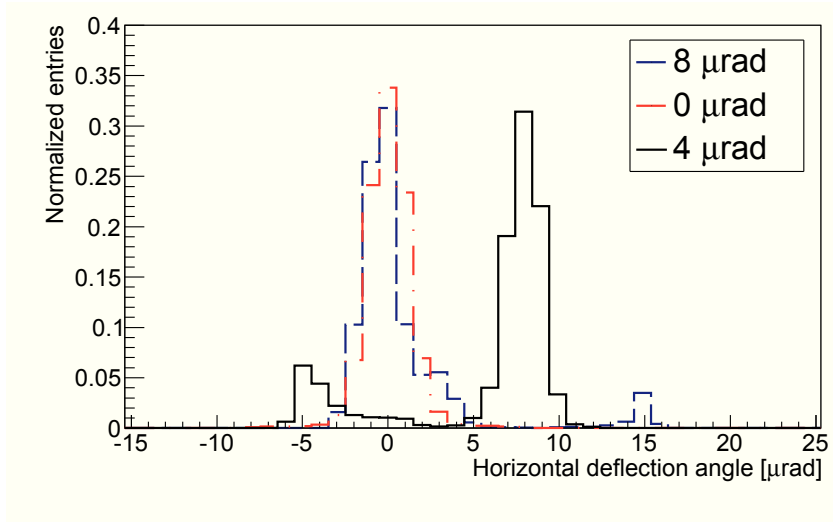


Figure 6.12: The distributions of angular deflection obtained by Monte Carlo simulation for a parallel beam of 400 GeV/c protons misaligned with the (001) planes of a 26.5  $\mu\text{m}$  thick Si crystal of a tilt angle equal to 4  $\mu\text{rad} \sim \theta_c/2$  (solid), 8  $\mu\text{rad} \sim \theta_c$  (dashed) and 0  $\mu\text{rad}$  (dot-dashed).

### 6.2.3 Experiment at CERN SPS

An experiment to test the feasibility of a crystalline mirror for 400 GeV/c protons was performed at the SPS-H8 extracted beamline in October 2012 by the UA9 collaboration. The experimental setup was based on a particle telescope developed at the Imperial College of London [156], consisting of ten planes of silicon microstrip sensors, arranged as five pairs, each measuring two orthogonal coordinates, with an active area of  $3.8 \times 3.8 \text{ cm}^2$  (see Fig. 6.13).

The telescope system had a long baseline, of approximately 10 m in each arm, and achieved an angular resolution in the incoming arm of 2.5  $\mu\text{rad}$  and a total angular resolution on the difference of the two arms of 5.2  $\mu\text{rad}$ , with performance limited by multiple scattering in the sensor layers. The upstream section of the telescope for the measurement of incoming tracks is formed by planes couple 1 and 2 while outgoing tracks are measured using planes couple 3, 4 and 5. Plane 4 is a rotated XY plane ( $\pi/4$ ), used in order to resolve ambiguities in reconstruction from multiple outgoing tracks. Events were triggered on the signal coincidence recorded by a pair of plastic scintillators placed downstream the telescope.

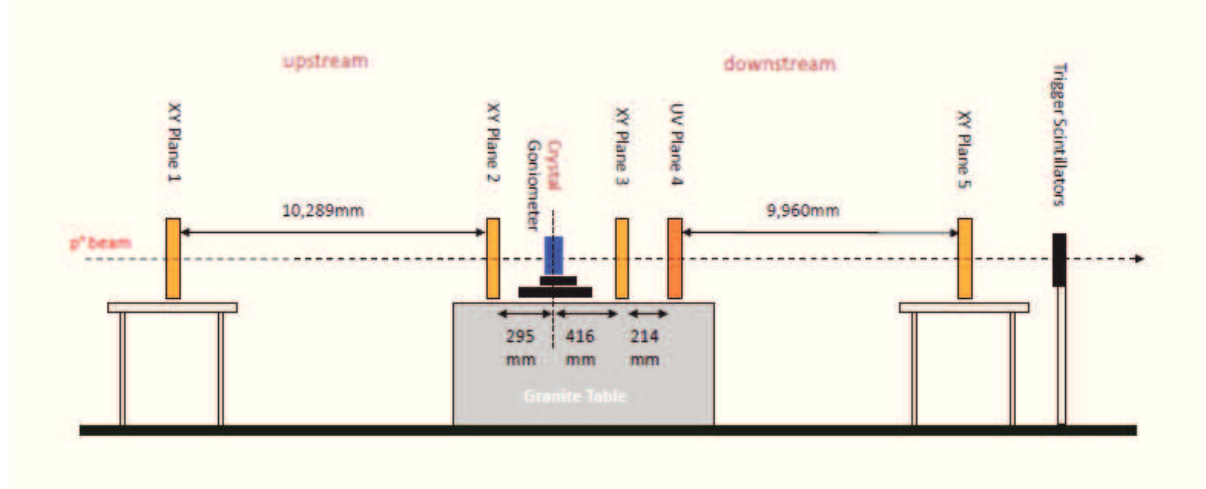


Figure 6.13: Experimental layout in the H8 beam line. The UV plane denotes the rotated ( $\pi/4$ ) XY plane. Adapted from [156].

The crystal was mounted on a high-precision goniometer with an angular resolution of about  $1 \mu\text{rad}$ . This instrument allowed three degrees of freedom, one linear and two rotational movements to align the crystal along either the horizontal or vertical directions [157]. Pre-alignment of the sample was worked out by means of a laser system parallel to the beam direction. An angular scan of crystal planes with respect to the beam orientation was then performed to find the ideal region for the mirror effect. The crystal was rotated around the horizontal axis and, for each angular position, the particle distribution after interaction with the crystal was recorded.

Fig. 6.14 displays the experimental deflection distribution of the beam in the direction orthogonal to (001) crystal planes (x) vs. crystal-beam orientation. The crystal-beam orientation was obtained adding the incidence angle of each particle as measured by the incoming arm to the nominal value of the goniometer. The 2D deflection distribution shows a two-fold structure, in which particle with a positive incidence angle ( $\theta_{in} > 0$ ) are deflected with  $\Delta\theta = \theta_{out} - \theta_{in} < 0$  and vice versa. In Fig. 6.15, the mean mirror peak position obtained through a Gaussian fit vs. the incidence angle with respect to the crystal planes is shown. One can notice that the deflection angle is not equal to double of the incidence angle as expected from theory. For a better understanding, Fig. 6.16 shows the 1D horizontal deflected beam distributions for each angular position every  $\mu\text{rad}$  in the range within  $\pm\theta_c \approx 8\mu\text{rad}$ . From the left to the right, from the top to the bottom, the seventeen profiles from  $-8 \mu\text{rad}$  to  $+8 \mu\text{rad}$  (incrementation equal to  $1 \mu\text{rad}$ ) are shown. It is easy to see that no one of this profiles resembles those obtained through simulations of

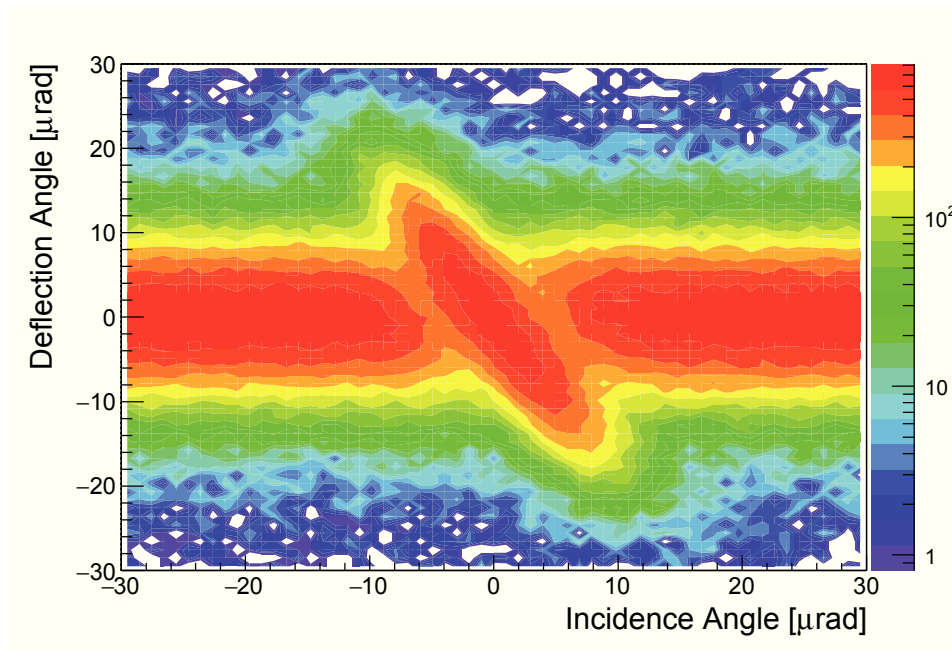


Figure 6.14: Deflected beam distribution in the direction orthogonal to (001) crystal planes (x) vs. crystal planes-to-beam orientation.

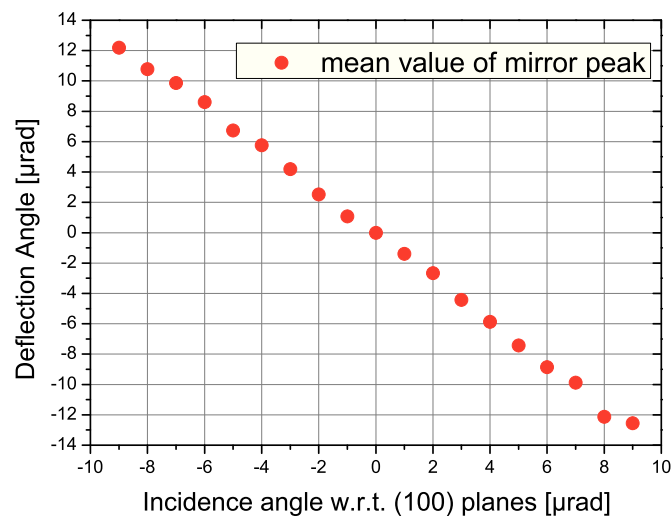


Figure 6.15: The mean mirror peak position vs. the incidence angle with respect to the crystal planes.

Fig. 6.12. This can be ascribed to the finite experimental resolution, which is not capable to completely resolve a such fine effect.

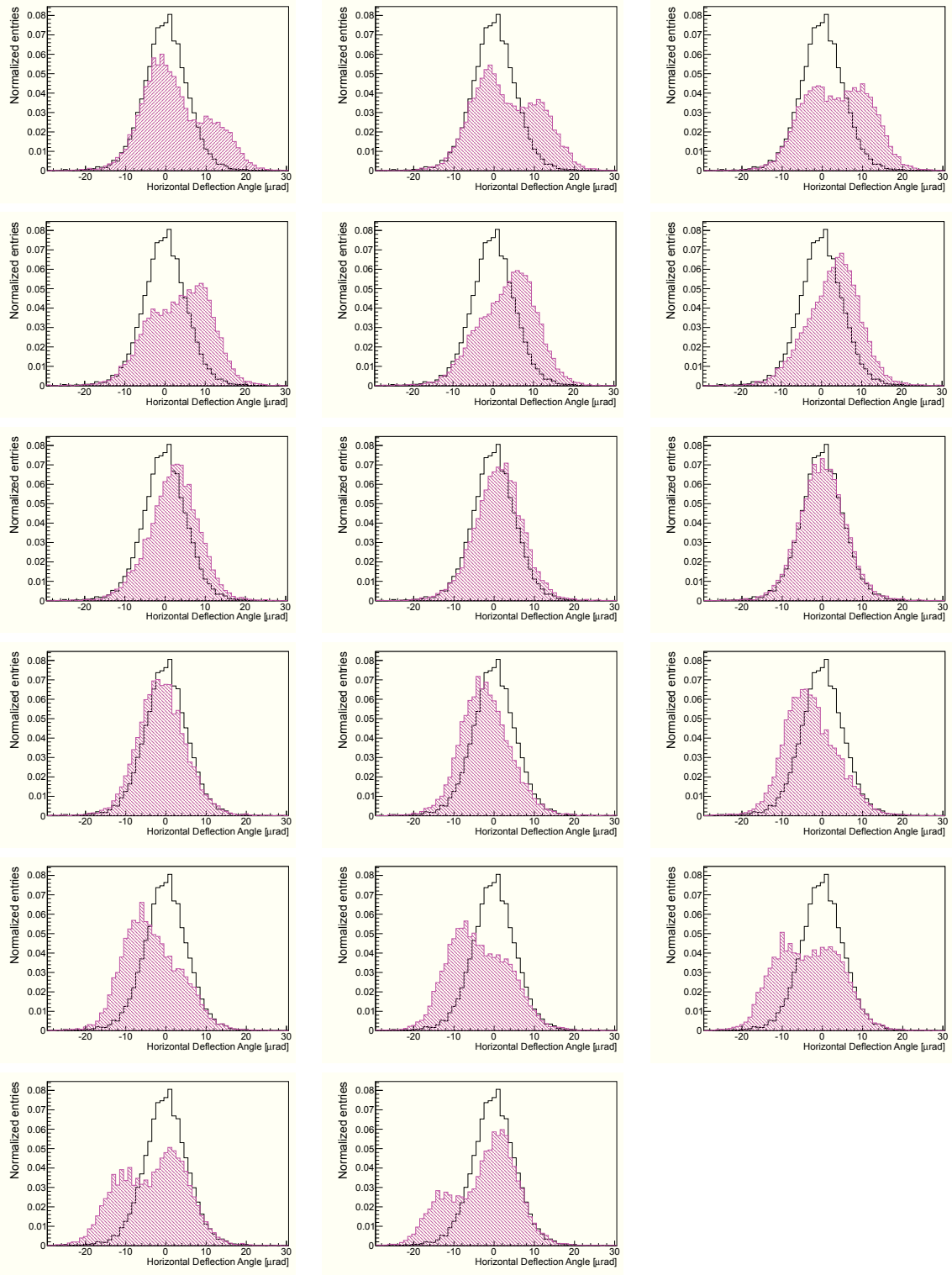


Figure 6.16: Horizontal deflection distribution vs. incidence angle with respect to (001) planes (pink distributions). The  $\theta_{in}$  values are from  $-8 \mu\text{rad}$  to  $+8 \mu\text{rad}$  with a step of  $1 \mu\text{rad}$  (Read from left to right and from top to bottom). The misaligned case is also shown for comparison.

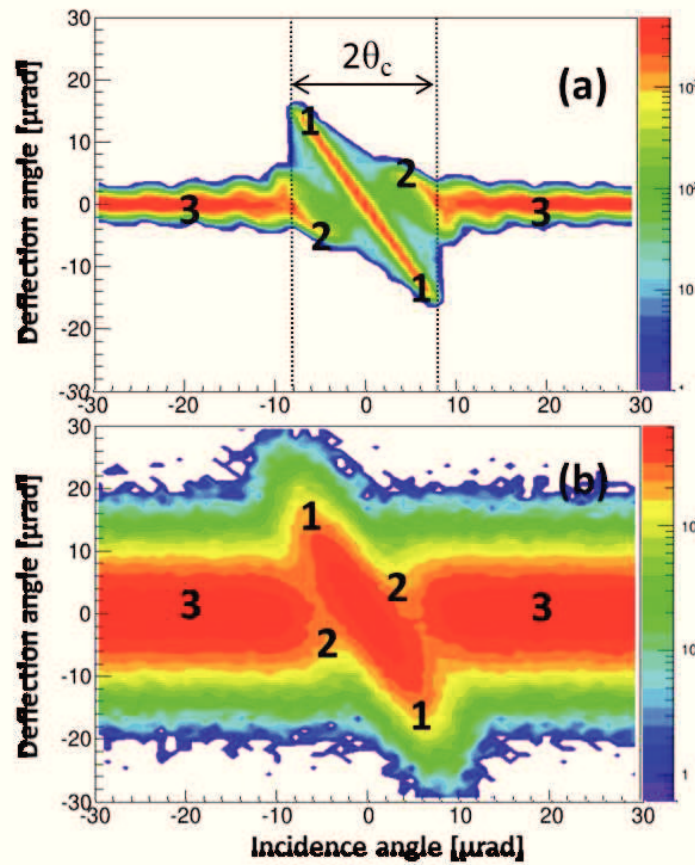


Figure 6.17: Deflected beam distribution in the direction orthogonal to (001) crystal planes (x) vs. crystal planes-to-beam orientation. (a) Simulation for a parallel beam of 400 GeV/c interacting with the crystal; (b) the same after the convolution with the finite resolution of the experimental apparatus. Adapted from [A6].

Indeed, a theoretical prediction of the outcomes of the scan is shown in Fig. 6.17(a), where the simulated beam distribution after interaction with the crystal as a function of the incidence angle is displayed. The effect of mirroring is observed within the whole angular range for channeling, that is  $2\theta_c$  wide, and the crystal shows a perfect spatial symmetry upon reversal of the incident angle. Four regions can be identified. In region (1) beam deflection occurs via particle mirroring through interaction with the (001) crystal planes. The region (2) corresponds to the deflection experienced by over-barrier particles within the angular acceptance for channeling. In regions (3) all the particles move in over-barrier conditions and are scattered almost incoherently as it would be for an amorphous material. Indeed, the presence of the oscillations in the pattern of regions (3) suggests that the crystal planes are still capable of deflecting over-barrier particles to some extent. In any case such

deflection is very small and quickly decreases with the incidence angle.

For a direct comparison with the experiment, a convolution between the simulated profile and the experimental resolutions for incidence and deflection angles has been computed (see Fig. 6.17(b)). The effect of the finite resolution is to spread out the beam distribution and to eliminate the clear distinction between region (1) and (2) of under- and above-barrier particles within the  $2\theta_c$  angular acceptance for mirror. There is a very good agreement between the patterns in Figs. 6.17(b) and 6.14, as a proof of the observation of the mirror effect for 400 GeV/c protons.

Fig. 6.18 is a more quantitative comparison between simulation and experiment for three significant crystal-to-beam misalignments. The experimental (solid) and the convoluted (dashed) angular distribution of the deflected beam are shown in Fig. 6.18(a)-(b)-(c) for tilt angle equal to 0  $\mu\text{rad}$  (perfect alignment with (001) planes), 4  $\mu\text{rad} \approx \theta_c/2$  and 8  $\mu\text{rad} \approx \theta_c$ , respectively. Good agreement between experimental results and simulation outcomes can be inferred in all three cases. As in Ref. [24], the tilt angle equal to  $\theta_c/2$  (see Fig. 6.18(b)) results as the most efficient case for mirroring. The finite angular resolution of the telescope does not allow estimating the deflection efficiency of the crystal mirror as we have done through simulations. We remind here that, for a parallel beam, the percentage of particles deflected with an angle larger than zero is about the 84% for the ideal case of  $\theta_{in} = 4 \mu\text{rad}$ .

## 6.2.4 Summarizing

In summary, it has been experimentally proven that a properly sized ultra-thin crystal can be used for mirroring of ultrarelativistic positively charged-particles. It was shown that the deflecting angle achievable through the mirror effect is of the order of  $\theta_c$  as for volume reflection, while the angular acceptance is the same as for channeling. The main advantage of mirroring is to involve a minimal amount of material for interaction of the particles with the crystal. For comparison, in channeling or volume-reflection experiments with ultra-high energy protons, 1-2 mm long bent crystals are used [40, 158]. Therefore, the usage of a crystal of a few tens of microns thickness would decrease the unwanted nuclear interactions by two orders of magnitude. A crystal-based collimator for a particle accelerator equipped with a crystal mirror not only would reduce the rate of nuclear interactions but also would avoid any problem related to the non-zero angle of the crystalline planes with the geometrical surface of the crystal (the so-called miscut) [14], thus decreasing further the particle losses during the first encounters with the crystal collimator. Another advantage of a crystal mirror is the non-necessity for an external mechanical device for crystal

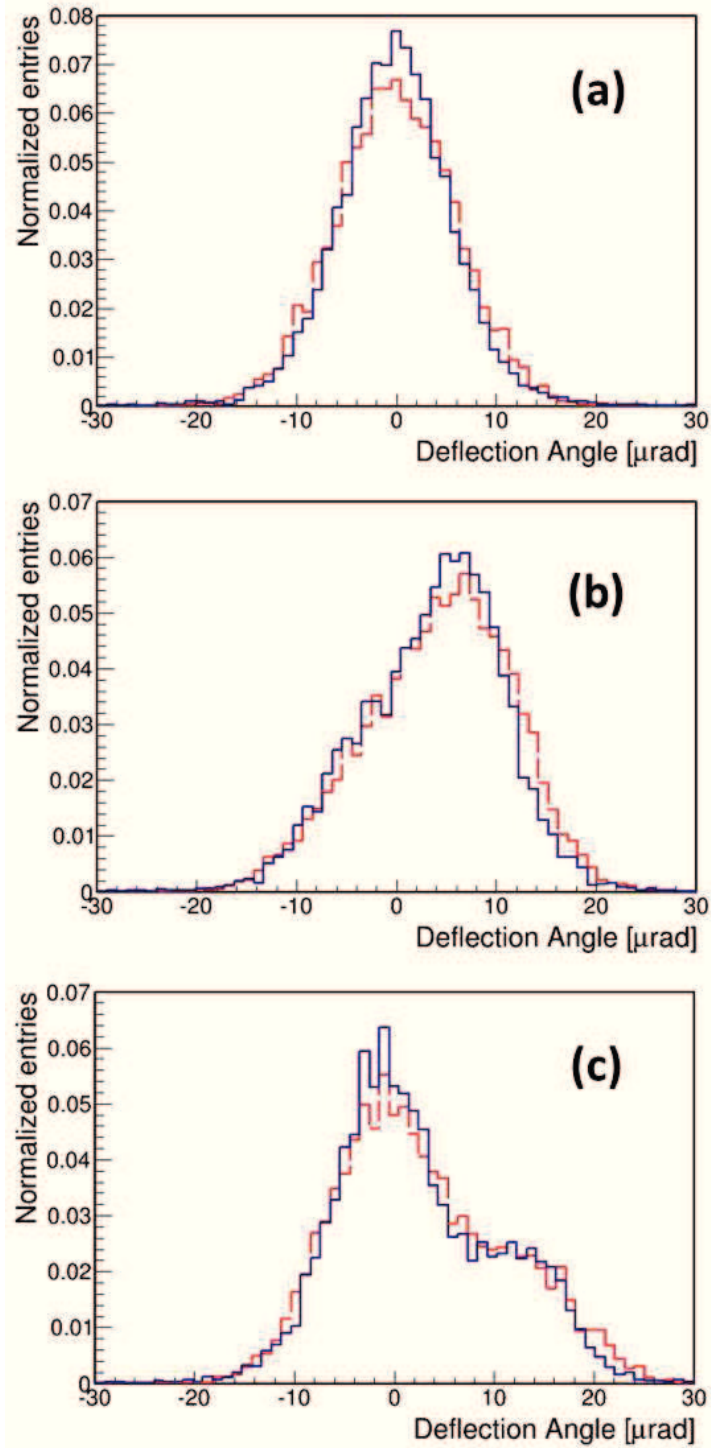


Figure 6.18: The distributions of angular deflection of 400 GeV/c protons in a (001) Si crystal 26.5  $\mu\text{m}$  observed in experiments (solid) and obtained by Monte Carlo simulation with accounting the angular resolution for outgoing particles (dashed) for three different crystal-to-beam orientations. Tilt angles are 0  $\mu\text{rad}$  (a), 4  $\mu\text{rad} \approx \theta_c/2$  (b) and 8  $\mu\text{rad} \approx \theta_c$  (c). Adapted from [A6].

bending [159], thereby circumventing the problem of crystal torsion and its compensation [89]. Moreover, if a deflection of the order of  $\theta_c$  would not be sufficient for an effective beam steerer, multiple mirroring can be envisaged through the usage of an array of properly oriented crystal mirrors, in analogy to the case of multiple volume reflection [160]. However, the smaller angular acceptance for mirror compared with volume reflection does require a high precision alignment system such as that in Ref. [39].



# Conclusions

The work presented in this thesis has been devoted to investigate new possibilities for beam steering and high-intense e.m. radiation generation through coherent interactions of charged particle beams with crystals. The results of different experiments were analyzed and critically compared with simulations.

An experiment performed at the external line H4 of CERN Super Proton Synchrotron with 120 GeV/c electrons demonstrated the possibility to exploit bent crystals under single (VR) and multiple (MVROC) volume reflection conditions to generate wide-spectrum and very-intense electromagnetic radiation. The most peculiar characteristics of VR-MVROC radiation are the higher intensity than for an amorphous material, the wide angular acceptance and the weak dependence on the particle charge and trajectory. The combination of these features makes these types of radiation suitable for the conversion of high-emittance electron beams into hard gamma quanta in high-Z crystals (like tungsten). By combining the high deflecting capability with the high radiative power, VR and MVROC can be envisaged as good candidates for crystal-assisted collimation in future electron-positron colliders.

With the aim of extending the knowledge on coherent interactions between electrons and bent crystals to an unexplored energy range, an experiment was conducted at the Minzer Microtron (Germany), demonstrating the possibility to steer sub-GeV electron beams via channeling and VR in a short bent crystal. It was also demonstrated the possibility to exploit bent crystals in the sub-GeV energy range to generate hard and intense electromagnetic radiation. Channeling radiation and the radiation accompanying VR resulted to be much more intense than for an amorphous material. The expansion of the code DYNECHARM++ with the newly developed RADCHARM++ routine for computation of e.m. radiation production in crystals has been used to investigate the contribution of incoherent scattering in the radiation formation. In particular, it was shown how the radiation accompanying VR is enhanced by the contribution of incoherent scattering in its whole wide angular acceptance. As for the higher energies case, the radiation accompanying VR

provides interesting prospects for applications as sources of high-intensity electromagnetic radiation, in an energy range interesting for many electron accelerators worldwide available. All these information together could be taken into account to design periodically bent crystals, i.e., crystalline undulators, as innovative compact sources of X- and  $\gamma$ -radiation.

Apart the studies conducted with the usage of ultrarelativistic electrons, a campaign of measurements for the investigation of new possibility for charged beam steering and manipulation was carried out the external line H8 of CERN-SPS with 400 GeV/c protons. First of all, a characterization of a periodically bent crystal realized via supetrificial grooving method was done, showing the feasibility of such a method. On the strength of such characterization, the possibility to test the crystal as a positron-based crystalline undulator in the 10-20 GeV energy range has been proposed. Finally, it has been experimentally proven that a properly sized ultra-thin straight crystal, i.e., a *crystal mirror*, can be used for the steering of ultrarelativistic protons. It was shown that the deflecting angle achievable through the mirror effect is of the order of the Lindhard critical angle as for volume reflection, while the angular acceptance is the same as for channeling. Nevertheless, a crystal mirror has the advantage to involve a minimal amount of material for interaction of the particles with the crystal, thus being interesting for a crystal-assisted collimation. For comparison, in channeling or volume-reflection based collimation, 1-2 mm long bent crystals are used. Therefore, the usage of a crystal of a few tens of microns thickness would decrease the unwanted nuclear interactions by two orders of magnitude.

Summarizing, all the experimental studies presented in this thesis lead us to consider crystals, either bent or unbent, as reliable tools in particle accelerator physics for different applications within a wide energy range.

# Bibliography

- [1] J. Lindhard, Danske Vid. Selsk. Mat. Fys. Medd. **34**, 14 (1965).
- [2] M. T. Robinson and O. S. Oen, Phys. Rev. **132**, 2385 (1963).
- [3] L. Feldman, J. Mayer, and S. Picraux, *Materials analysis by ion channeling* (Academic Press, 1982).
- [4] V. Baier, V. Katkov, and V. Strakhovenko, *Electromagnetic Processes at High Energies in Oriented Single Crystals* (World Scientific, Singapore, 1998).
- [5] D. Scott, J. Clarke, D. Baynham, V. Bayliss, T. Bradshaw, G. Burton, A. Brummitt, S. Carr, A. Lintern, J. Rochford, *et al.*, Physical review letters **107**, 174803 (2011).
- [6] H. Bethe, W. Heitler, Proc. Roy. Soc. **146**, 83 (1934).
- [7] D. Lohmann, J. Peise, J. Ahrens, I. Anthony, H.-J. Arends, R. Beck, R. Crawford, A. Hüniger, K. Kaiser, J. Kellie, *et al.*, Nuclear Instruments and Methods in Physics Research Section A: Accelerators, Spectrometers, Detectors and Associated Equipment **343**, 494 (1994).
- [8] B. Ferretti, Nuovo Cim. **7**, 118 (1950).
- [9] M. L. Ter-Mikaelian, *High-energy Electromagnetic Processes in Condensed Media* (Wiley, New York, 1972).
- [10] H. Uberall, Phys. Rev. **103**, 1055 (1956).
- [11] M. Kumakhov, Physics Letters A **57**, 17 (1976).
- [12] E. Tsyganov, *Some aspects of the mechanism of a charge particle penetration through a monocrystal*, Tech. Rep. (Fermilab, 1976) preprint TM-682.
- [13] H. Akbari *et al.*, Physics Letters B **313**, 491 (1993).
- [14] W. Scandale *et al.*, Phys. Lett. B **714**, 231 (2012).
- [15] W. Scandale *et al.*, Phys. Lett. B **703**, 547 (2011).

- [16] A. Taratin and S. Vorobiev, Phys. Lett. A **119**, 425 (1987).
- [17] V. M. Biryukov et al., Nucl. Instrum. Methods Phys. Res. Sect. B **234**, 23 (2005).
- [18] E. Uggerhoj and U. Uggerhoj, Nucl. Instrum. Methods Phys. Res. Sect. B **234**, 31 (2005).
- [19] A. Seryi, Nucl. Instrum. Methods Phys. Res., Sect. A **623**, 23 (2010).
- [20] W. Scandale, et al., Phys. Rev. A **79**, 012903 (2009).
- [21] D. Lietti et al., Nucl. Instrum. Methods Phys. Res., Sect. B **283**, 84 (2012).
- [22] Yu. A. Chesnokov et al., Journal of Instrumentation **3**, P02005 (2008).
- [23] A. V. Korol, A. V. Solov'yov, and W. Greiner, *Channeling and Radiation in Periodically Bent Crystals* (Springer Berlin Heidelberg, 2013).
- [24] E. Tsyganov and A. Taratin, Nucl. Instrum. Methods Phys. Res., Sect. A **363**, 511 (1995).
- [25] J. Stark, Phys. Zs. **13**, 973 (1912).
- [26] G. D. Palazzi, Rev. Mod. Phys. **40**, 611 (1968).
- [27] M. T. Robinson and O. S. Oen, Applied Physics Letters **2**, 30 (1963).
- [28] G. R. Piercy et al., Phys. Rev. Lett. **10**, 399 (1963).
- [29] A. Taratin, Physics of Particles and Nuclei **29**, 437 (1998).
- [30] A. Vodopyanov, V. Golovatyuk, A. Elishev, *et al.*, JETP Lett **30**, 442 (1979).
- [31] V.A. Andreev *et al.*, Pis'ma v Zh. Eksp. Teor. Fiz. **36**, 340 (1982).
- [32] V. Tikhomirov, Physics Letters B **655**, 217 (2007).
- [33] Yu. M. Ivanov *et al.*, Phys. Rev. Lett. **97**, 144801 (2006).
- [34] W. Scandale et al., Phys. Rev. Lett. **98**, 154801 (2007).
- [35] W. Scandale *et al.*, Phys. Lett. B **681**, 233 (2009).
- [36] W. Scandale et al., Physics Letters B **682**, 274 (2009).
- [37] W. Scandale *et al.*, Phys. Lett. B **693**, 545 (2010).
- [38] W. Scandale *et al.*, EPL (Europhysics Letters) **93**, 56002 (2011).
- [39] W. Scandale *et al.*, Phys. Rev. Lett. **102**, 084801 (2009).

- [40] W. Scandale et al., Phys. Rev. Lett. **101**, 164801 (2008).
- [41] N. Shul'ga and A. Greenenko, Physics Letters B **353**, 373 (1995).
- [42] V. M. Biryukov, Y. A. Chesnekov, and V. I. Kotov, *Crystal Channeling and Its Applications at High-Energy Accelerators* (Springer, 1996).
- [43] S. Hasan, *Bent silicon crystals for the LHC collimation: studies with an ultrarelativistic proton beam*, Master's thesis, University of Insubria (2007).
- [44] P. t. Doyle and P. Turner, Acta Crystallographica Section A: Crystal Physics, Diffraction, Theoretical and General Crystallography **24**, 390 (1968).
- [45] G. Molière, Z. Naturforsch. A **2**, 133 (1947).
- [46] W. Scandale et al., Physics Letters B **719**, 70 (2013).
- [47] W. R. Leo, *Techniques for nuclear and particle physics experiments: a how-to approach* (Springer, 1994).
- [48] J. Beringer et al. (Particle Data Group), Phys. Rev. D **86**, 010001 (2012).
- [49] W. T. Scott, Rev. Mod. Phys. **35**, 231 (1963).
- [50] V. V. Beloshitsky, M. A. Kumakhov, and V. A. Muralev, Radiation Effects **13**, 9 (1972).
- [51] W. Scandale et al., Phys. Lett. B **680**, 129 (2009).
- [52] R. J. Carrigan and J. Ellison, *Relativistic Channeling* (Plenum Press, 1987).
- [53] H. Backe, P. Kunz, W. Lauth, and A. Rueda, Nuclear Instruments and Methods in Physics Research Section B: Beam Interactions with Materials and Atoms **266**, 3835 (2008).
- [54] E. H. and G. J.A., Nucl. Phys. A **298**, 382 (1978).
- [55] H. Esbensen, O. Fich, J. Golovchenko, S. Madsen, H. Nielsen, H. Schiøtt, E. Uggerhøj, C. Vraast-Thomsen, G. Charpak, S. Majewski, et al., Physical Review B **18**, 1039 (1978).
- [56] K. Olive et al. (Particle Data Group), Chin.Phys. **C38**, 090001 (2014).
- [57] W. Scandale et al., Phys. Rev. Lett. **101**, 234801 (2008).
- [58] Y. Chesnokov, N. Galyaev, V. Kotov, S. Tsarik, and V. Zapolsky, Nuclear Instruments and Methods in Physics Research Section B: Beam Interactions with Materials and Atoms **69**, 247 (1992).

- [59] V. Guidi, A. Mazzolari, and V. Tikhomirov, *Journal of Applied Physics* **107**, 114908 (2010).
- [60] V. Guidi, A. Mazzolari, and V. Tikhomirov, *Il nuovo cimento, COLLOQUIA: Channeling 2010.* (2011).
- [61] J. D. Jackson, *Classical Electrodynamics* (Wiley & Sons, 1975).
- [62] L. Landau and E. Lifshitz, *The Classical Theory of Fields. Vol. 2 (4th ed.)*. (Butterworth-Heinemann, 1975).
- [63] A. Akhiezer and N. Shulga, *High-energy electrodynamics in matter* (Gordon & Breach, New York, 1996).
- [64] L. D. Landau and I. Pomeranchuk, in *Dokl. Akad. Nauk SSSR*, Vol. 92 (1953) p. 535.
- [65] U.I. Uggerhoj *et al.*, *Physics Letters B* **619**, 240 (2005).
- [66] D. Lietti *et al.*, *Nuclear Instruments and Methods in Physics Research Section B: Beam Interactions with Materials and Atoms* **283**, 84 (2012).
- [67] W. G. Andrey V. Korol, Andrey V. Solov'yov, *Channeling and Radiation in Periodically Bent Crystals* (Springer, New York City, 2013).
- [68] L. Bandiera *et al.*, *Nuclear Instruments and Methods in Physics Research Section B: Beam Interactions with Materials and Atoms* **309**, 135 (2013).
- [69] L. Bandiera *et al.*, *Phys. Rev. Lett.* **111**, 255502 (2013).
- [70] V. Guidi, L. Bandiera and V. Tikhomirov, *Phys. Rev. A* **86**, 042903 (2012).
- [71] V. M. Strakhovenko, *Phys. Rev. A* **68**, 042901 (2003).
- [72] U. Uggerhøj, *Ultrarelativistic particles in matter*, Ph.D. thesis, Doctoral Dissertation. Department of Physics and Astronomy, University of Aarhus, Denmark, [http://www.phys.au.dk/~ulrik/Doct\\_dis\\_UIU.pdf](http://www.phys.au.dk/~ulrik/Doct_dis_UIU.pdf) (2011).
- [73] V. Baier and V. Katkov, *Physics Letters A* **25**, 492 (1967).
- [74] V. Baier and V. Katkov, *Sov. Phys. JETP* **26**, 854 (1968).
- [75] V. P. Lapko, N. F. Shul'ga, A. S. Esaulov, *Ukrayins'kij Fyizichnij Zhurnal* **52**, 571 (2007).
- [76] V. Tikhomirov, *Nuclear Instruments and Methods in Physics Research Section B: Beam Interactions with Materials and Atoms* **36**, 282 (1989).
- [77] X. Artru, *Nuclear Instruments and Methods in Physics Research Section B: Beam Interactions with Materials and Atoms* **48**, 278 (1990).

- [78] E. Bagli and V. Guidi, Nuclear Instruments and Methods in Physics Research Section B: Beam Interactions with Materials and Atoms **309**, 124 (2013).
- [79] E. Bagli et al., Phys. Rev. Lett. **110**, 175502 (2013).
- [80] E. Bagli et al., The European Physical Journal C **74**, 1 (2014).
- [81] E. Bagli et al., Eur. Phys. J. C **74**, 3114 (2014).
- [82] E. Bagli, V. Guidi, V. A. Maisheev, Proc. of 1st International Particle Accelerator Conference: IPAC'10 , TUPEA070 (2010).
- [83] E. Bagli, V. Guidi, V. A. Maisheev, Phys. Rev. E **81**, 026708 (2010).
- [84] A. Jankowiak, Eur. Phys. J. A **28**, 149 (2006).
- [85] E. Bagli et al., Physical review letters **110**, 175502 (2013).
- [86] S. Hasan, *Experimental Techniques for deflection and radiation studies with bent crystals*, Ph.D. thesis, University of Insubria (2011).
- [87] D. Lietti and A. Berra and M. Prest and E. Vallazza, Nuclear Instruments and Methods in Physics Research Section A: Accelerators, Spectrometers, Detectors and Associated Equipment **729**, 527 (2013).
- [88] S. Baricordi *et al.*, J. Phys. D **41**, 245501 (2008).
- [89] E. Bagli, P. Dalpiaz, V. Guidi, A. Mazzolari, D. Vincenzi, A. Carnera, D. De Salvador, G. Della Mea, and A. Taratin, in *The 1st International Particle Accelerator Conference (IPAC10) IPAC*, Vol. 10 (2010) pp. 4243–4245.
- [90] V. Guidi, L. Lanzoni, and A. Mazzolari, Journal of Applied Physics **107**, 113534 (2010).
- [91] M. Prest, G. Barbiellini, G. Bordignon, G. Fedel, F. Liello, F. Longo, C. Pontoni, and E. Vallazza, Nuclear Instruments and Methods in Physics Research Section A: Accelerators, Spectrometers, Detectors and Associated Equipment **501**, 280 (2003).
- [92] A. Berra, *Silicon Photomultipliers in high energy and space applications*, Ph.D. thesis, University of Insubria (2012).
- [93] V. Maisheev, Il nuovo Cimento C (2011).
- [94] V. Arutyunov, N. Kudryashov, V. Samconov, and M. Strikhanov, Nuclear Physics B **363**, 283 (1991).
- [95] V. Tikhomirov, Nuclear Instruments and Methods in Physics Research Section B: Beam Interactions with Materials and Atoms **82**, 409 (1993).

- [96] S. Bellucci and V. Maisheev, *Physical Review A* **86**, 042902 (2012).
- [97] V. Baryshevskii and V. Tikhomirov, *Sov. Phys. Usp.* **32**, 1013 (1989).
- [98] D. De Salvador *et al.*, *Journal of Applied Physics* **114**, 154902 (2013).
- [99] N. S. Lockyer, in *The Logic Of Nature, Complexity and New Physics. From Quark-Gluon Plasma to Superstrings, Quantum Gravity and Beyond*, Vol. 1 (2008) pp. 399–418.
- [100] F. Zimmermann, *Beam Dynamics Challenges for Future Circular Colliders*, Tech. Rep. (CERN, 2004).
- [101] G. Ellwood and J. Greenhalgh, in *Particle Accelerator Conference, 2007. PAC. IEEE* (IEEE, 2007) pp. 2859–2861.
- [102] A. Toader, R. Barlow, F. Jackson, and D. Angal-Kalinin, *EUROTeV-Report-2008-024* (2008).
- [103] V. Guidi, A. Mazzolari, D. De Salvador, and L. Bacci, *Phys. Rev. Lett.* **108**, 014801 (2012).
- [104] Y. M. Ivanov, Y. A. Gavrikov, A. Denisov, A. Zhelamkov, V. Ivochkin, S. Kosyanko, L. Lapina, A. Petrunin, V. Skorobogatov, V. Suvorov, *et al.*, *JETP letters* **84**, 372 (2006).
- [105] W. Scandale *et al.*, *Phys. Lett. B* **692**, 78 (2010).
- [106] R. A. Carrigan *et al.*, *Phys. Rev. ST Accel. Beams* **5**, 043501 (2002).
- [107] E. Uggerhoj and U. Uggerhoj, *Nuclear Instruments and Methods in Physics Research Section B: Beam Interactions with Materials and Atoms* **234**, 31 (2005).
- [108] Y. N. Adishchev, P. Ananyin, A. Didenko, B. Kalinin, V. Kaplin, E. Rozum, A. Potylitsyn, S. Vorobiev, and V. Zabaev, *Physics Letters A* **77**, 263 (1980).
- [109] A. Baurichter, K. Kirsebom, R. Medenwaldt, S. Møller, T. Worm, E. Uggerhøj, C. Biino, M. Clément, N. Doble, K. Elsener, *et al.*, *Nuclear Instruments and Methods in Physics Research Section B: Beam Interactions with Materials and Atoms* **119**, 172 (1996).
- [110] W. Scandale *et al.*, *Phys. Lett. B* **680**, 301 (2009).
- [111] D. Lietti *et al.*, submitted to *Rev. Sci. Instr.* (2015).
- [112] D. Lietti, A. Berra, M. Prest, and E. Vallazza, *Nuclear Instruments and Methods in Physics Research Section A: Accelerators, Spectrometers, Detectors and Associated Equipment* **729**, 527 (2013).

- [113] V. Guidi *et al.*, J. Phys. D **42**, 182005 (2009).
- [114] G. Germogli *et al.*, submitted to Nucl. Instrum. and Meth. in Phys. Res. B. (2014).
- [115] Y. Ivanov, A. Petrunin, and V. Skorobogatov, Journal of Experimental and Theoretical Phys. Lett. **81**, 99 (2005).
- [116] V. Baryshevsky and V. Tikhomirov, Nuclear Instruments and Methods in Physics Research Section B: Beam Interactions with Materials and Atoms **309**, 30 (2013).
- [117] C. Gary, R. Pantell, M. Özcan, M. Piestrup, and D. Boyers, Journal of applied physics **70**, 2995 (1991).
- [118] V. L. Ginzburg, Izv. Akad. Nauk SSSR Ser. Fiz. **11**, 165 (1947).
- [119] H. Motz, J. Appl. Phys. **22**, 527 (1951).
- [120] P. Elleaume, Beam Line **14**, 32 (2002).
- [121] X. A. R. Rullhusen and P. Dhez., *Novel radiation sources using relativistic electrons. From infrared to x-rays.* (World Scientific Publishing Co. Pte. Ltd., 1998).
- [122] H. Schneider-Muntau, J. Toth, and H. Weijers, Applied Superconductivity, IEEE Transactions on **14**, 1245 (2004).
- [123] D. Li, K. Imasaki, and M. Aoki, Journal of nuclear science and technology **39**, 1247 (2002).
- [124] R. Haxby, W. Shoupp, W. Stephens, and W. Wells, Physical Review **59**, 57 (1941).
- [125] V. Granatstein, W. Destler, and I. Mayergoyz, Appl. Phys. Lett. **47**, 643 (1985).
- [126] G. Ramian, L. Elias, and I. Kimel, Nucl. Instrum. Methods Phys. Res., Sect. A **250**, 125 (1986).
- [127] K. Paulson, Nucl. Instrum. Methods Phys. Res., Sect. A **296**, 624 (1990).
- [128] R. Tatchyn and P. Csonka, Appl. Phys. Lett. **50**, 377 (1987).
- [129] R. Tatchyn, A. Toor, J. Hunter, R. Hornady, D. Whelan, G. Westenskow, P. Csonka, T. Cremer, and E. Kallne, J. X-Ray Sci. Technol. **1**, 79 (1989).
- [130] R. Tatchyn, P. Csonka, and A. Toor, Rev. Sci. Instrum. **60**, 1796 (1989).
- [131] A. Kostyuk, Phys. Rev. Lett. **110**, 115503 (2013).
- [132] Mehdi Tabrizi *et al.*, Phys. Rev. Lett. **98**, 164801 (2007).
- [133] V. Baryshevsky, I. Dubovskaya, and A. Grubich, Phys. Lett. A **77**, 61 (1980).

- [134] M. Breese, Nuclear Instruments and Methods in Physics Research Section B: Beam Interactions with Materials and Atoms **132**, 540 (1997).
- [135] A. G. Afonin *et al.*, Nuclear Instruments and Methods in Physics Research Section B: Beam Interactions with Materials and Atoms **234**, 122 (2005).
- [136] S. Bellucci *et al.*, Phys. Rev. ST Accel. Beams **7**, 023501 (2004).
- [137] P. Balling, J. Esberg, K. Kirsebom, D. Le, U. Uggerhj, S. Connell, J. Hrtwig, F. Masiello, and A. Rommeveaux, Nuclear Instruments and Methods in Physics Research Section B: Beam Interactions with Materials and Atoms **267**, 2952 (2009).
- [138] V. Guidi, A. Antonini, S. Baricordi, F. Logallo, C. Malag, E. Milan, A. Ronzoni, M. Stefancich, G. Martinelli, and A. Vomiero, Nuclear Instruments and Methods in Physics Research Section B: Beam Interactions with Materials and Atoms **234**, 40 (2005).
- [139] V. Guidi, L. Lanzoni, A. Mazzolari, G. Martinelli, and A. Tralli, Applied Physics Letters **90**, 114107 (2007).
- [140] S. Bellucci *et al.*, Phys. Rev. Lett. **90**, 034801 (2003).
- [141] Biryukov *et al.*, in *Advanced Radiation Sources and Applications*, NATO Science Series II: Mathematics, Physics and Chemistry, Vol. 199, edited by H. Wiedemann (Springer Netherlands, 2006) pp. 191–200.
- [142] V. Baranov, S. Bellucci, V. Biryukov, G. Britvich, V. Chepegin, Y. Chesnokov, C. Balasubramanian, G. Giannini, V. Guidi, V. Kotov, A. Kushnirenko, V. Maisheev, E. Milan, G. Martinelli, V. Pikalov, V. Terekhov, U. Uggerhj, and V. Zapolsky, Nuclear Instruments and Methods in Physics Research Section B: Beam Interactions with Materials and Atoms **252**, 32 (2006), relativistic Channeling and Coherent Phenomena in Strong Fields.
- [143] V. Baranov, S. Bellucci, V. Biryukov, G. Britvich, C. Balasubramanian, V. Guidi, G. Giannini, V. Zapolsky, V. Kotov, A. Kushnirenko, V. Maisheev, G. Martinelli, E. Milan, V. Pikalov, V. Terekhov, U. Uggerhoj, V. Chepegin, and Y. Chesnokov, Journal of Experimental and Theoretical Physics Letters **82**, 562 (2005).
- [144] H. Backe and D. Krambrich and W. Lauth and K.K. Andersen and J. Lundsgaard Hansen and Ulrik I. Uggerhoj, Nuclear Instruments and Methods in Physics Research Section B: Beam Interactions with Materials and Atoms **309**, 37 (2013).
- [145] H. Backe, D. Krambrich, W. Lauth, K. K. Andersen, J. L. Hansen, and U. I. Uggerhj, Journal of Physics: Conference Series **438**, 012017 (2013).
- [146] A. V. Korol, A. Solov'yov, and W. Greiner, International Journal of Modern Physics E **13**, 867 (2004).

- [147] T. N. Wistisen et al., Phys. Rev. Lett. **112**, 254801 (2014).
- [148] R. Camattari, V. Guidi, V. Bellucci, I. Neri, and M. Jentschel, Rev. Sci. Instrum. **84**, 053110 (2013).
- [149] R. Camattari, A. Battelli, V. Bellucci, and V. Guidi, Exp Astron **37**, 1 (2013).
- [150] V. Bellucci, R. Camattari, V. Guidi, and A. Mazzolari, Thin Solid Films **520**, 1069 (2011).
- [151] L. Celano et al., Nucl. Instrum. Methods Phys. Res. Sect. A **381**, 49 (1996).
- [152] S. Moller, E. Uggerhoj, H. Atherton, M. Clment, N. Doble, K. Elsener, L. Gatignon, P. Grafstrm, M. Hage-Ali, and P. Siffert, Physics Letters B **256**, 91 (1991).
- [153] A. G. Afonin *et al.*, Phys. Rev. Lett. **87**, 094802 (2001).
- [154] W. Scandale, G. Arduini, R. Assmann, C. Bracco, S. Gilardoni, V. Ippolito, E. Laface, R. Losito, A. Masi, E. Metral, *et al.*, Physics Letters B **692**, 78 (2010).
- [155] V. Guidi, A. Mazzolari, D. De Salvador, and L. Bacci, Physical review letters **108**, 014801 (2012).
- [156] M. Pesaresi, W. Ferguson, J. Fulcher, G. Hall, M. Raymond, M. Ryan, and O. Zorba, Journal of Instrumentation **6**, P04006 (2011).
- [157] W. Scandale, I. Efthymiopoulos, D. A. Still, A. Carnera, G. Della Mea, D. De Salvador, R. Milan, A. Vomiero, S. Baricordi, S. Chiozzi, *et al.*, Review of Scientific Instruments **79**, 023303 (2008).
- [158] W. Scandale, G. Arduini, M. Butcher, F. Cerutti, S. Gilardoni, L. Lari, A. Lechner, R. Losito, A. Masi, A. Mereghetti, *et al.*, Physics Letters B **726**, 182 (2013).
- [159] V. Carassiti, P. Dalpiaz, V. Guidi, A. Mazzolari, M. Melchiorri, Review of Scientific Instruments **81**, 066106 (2010).
- [160] W. Scandale *et al.*, Phys. Lett. B **688**, 284 (2010).